University of Southampton

Faculty of Physical Sciences and Engineering

Optoelectronics Research Centre

WAVELENGTH SELECTION AND TRANSVERSE MODE CONTROL IN HIGH POWER FIBRE LASERS

By

JAE M O DANIEL

Thesis for the degree of Doctor of Philosophy

December 2013

ABSTRACT

FACULTY OF PHYSICAL SCIENCES AND ENGINEERING

OPTOELECTRONICS RESEARCH CENTRE

DOCTOR OF PHILOSOPHY

WAVELENGTH SELECTION AND TRANSVERSE MODE CONTROL IN HIGH POWER FIBRE LASERS

By Jae M O Daniel

In this thesis we explore the wide parameter space of thulium doped silica fibre lasers, looking at various techniques for the control of operating wavelength and bandwidth as well as transverse beam profile. We demonstrate the extremely broad tunability of thulium fibre sources. Through various device architectures we show wavelength coverage over a 450nm wavelength range from 1660nm to 2115nm. With a simple external cavity containing an electronically controllable acousto-optic tunable filter we construct a wavelength agile tunable fibre source. This source demonstrates rapid wavelength selection and coverage within the thulium gain band including multiple simultaneous wavelength selection. Under fixed wavelength operation we show the generation of high power and efficiency 1726nm light in a monolithic thulium fibre source with output powers of up to 12.6W and internal laser slope efficiencies of 69%.

Exploiting the fast cavity dynamics of pulsed fibre sources we demonstrate the generation of a bandwidth and wavelength flexible ASE source. Under pulsed operation we generate peak powers of greater than 2kW with tunable bandwidth from 24nm to 0.28nm corresponding to a change in coherence length from ~5mm down to ~60µm. Applying this source to nonlinear frequency conversion, we show the ASE seeded supercontinuum generation at output powers of up to 1.5W, covering a wavelength range of more than one octave from 1000nm to greater than 2400nm. Looking further ahead with this ASE source, we investigate the effects of propagation and amplification within a multimode waveguide, highlighting the potentially detrimental effects of modal interference and through spectral bandwidth tailoring, successfully supresses these effects. Showing stable high peak power amplification within a multimode thulium fibre amplifier.

Finally, we introduce a novel mode selection technique utilising multimode fibre Bragg gratings. Allowing the selection of individual modes within a multimode fibre oscillator. We experimentally demonstrate this technique within a multimode thulium fibre source

showing the electronically controllable selection and arbitrary switching between the fundamental and next higher order mode at switching speeds of up to 20kHz and output powers of greater than 5W. Extending this technique, we show the generation of near arbitrary superpositions of the first two guided modes with electronically tunable beam ‘flatness’ and other parameters. The prospects for further core area scaling are also discussed.

Table of Contents

List of Figures

Declaration of Authorship

I, Jae M O Daniel, declare that the thesis entitled "Wavelength selection and transverse mode control in high power fibre lasers" and the work presented in the thesis are both my own, and have been generated by me as the result of my own original research.

I confirm that:

- this work was done wholly or mainly while in candidature for a research degree at this University;
- where any part of this thesis has previously been submitted for a degree or any other qualification at this University or any other institution, this has been clearly stated;
- where I have consulted the published work of others, this is always clearly stated;
- where I have quoted from the work of others, the source is always given. With the exception of such quotations, this thesis is entirely my own work;
- I have acknowledged all main sources of help;
- where the thesis is based on work done by myself jointly with others, I have made clear exactly what was done by others and what I have contributed myself;
- parts of this work have been published as: [see Appendix]

Signed: ……..

Date: **July 2014**

Acknowledgements

Over the past four years at the ORC I have been lucky enough to have had the chance to work with very talented people on a day to day basis and I am grateful for the help, advice and friendship they have provided. Without this support this thesis would not have been possible. Thank you to all those I have mentioned below as well as the countless others I have not.

I would like to thank my supervisor, Professor Andy Clarkson. For his always insightful advice and for giving me the freedom to guidance to be able to work on a wide range of interesting and challenging projects.

To the senior faculty members for their advice and assistance, Dr. Ji Won Kim, Dr Christophe Codemard, Dr. Jacob Mackenzie, Dr. Shaif-ul Alam, Dr. Jonathan Price, Dr Morten Ibsen and Prof. Jayanta Sahu.

To the people with whom I have had close collaboration on several different projects, Dr. Masaki Tokurakawa, Dr. Jaclyn Chan, Mr. Nikita Simakov, Mr. Zhihong Li, Mr. Di Lin.

To the past and present members of the ASSS whose labs I have looted and whose help I have valued, in particular Dr Rafal Cieslak, Dr. Peter Shardlow, Mr. Jakub Szela and Mr. Matthew Eckold (particularly for his valiant proof reading efforts).

To Dr's Mehta, Feinäugle, and Payne for their non-professional help as well as all the past and present occupants of 4017.

I would also like to thank and proudly acknowledge the support of my parents, my two sisters and my wonderful girlfriend Lina. All of whom have helped me get through what has been a long and eventful four years.

To my brother Tahl

Notation

AO	Acousto-optic
AOM	Acousto-optic modulator
AOTF	Acousto-optic tunable filter
ASE	Amplified spontaneous emission
CW	Continuous wave
DMD	Digital micromirror device
FBG	Fibre Bragg grating
FP	Fabry–Pérot (interferometer)
FRIP	Fibre refractive index profile
FWHM	Full width at half maximum
HNLF	Highly nonlinear fibre
HOM	Higher order mode
HR	High reflector
MCVD	Modified chemical vapour deposition
MFD	Mode field diameter
MM	Multimode
MM-FBG	Multimode fibre Bragg grating
MPE	Maximum permissible exposure
NA	Numerical aperture
OC	Output coupler
OCT	Optical coherence tomography

PER	Polarisation extinction ratio
PTR	Photo thermal refractive (glass)
RF	Radio Frequency
SBS	Stimulated Brillouin scattering
SC	Supercontinuum
SLM	Spatial light modulator
SM	Single mode
SMF	Single mode fibre
SRS	Stimulated Raman Scattering
TDF	Thulium doped fibre
TDFA	Thulium-doped fibre amplifier
TFB	Tapered fibre bundle
VBG	Volume Bragg grating
WDM	Wavelength division multiplexor
wt%	Weight percent

Chapter 1.

Introduction

1.1 Overview

The introduction of high power lasers into new markets tends to have a disruptive effect, displacing existing technologies and enabling processes that were otherwise impractical. This has resulted in the current market situation where it is almost impossible to purchase modern consumer goods that have not benefited from the use lasers at some point in their manufacture; such as the ubiquitous use of laser marking of plastics and metals. Within the semiconductor industry, lasers are used from the initial photolithography steps through to the final packaging of the end product. In the medical field lasers have also seen wide adoption, from application of the highly precise work conducted in laser ophthalmology through to the ablation of kidney stones. In the automotive and manufacturing industries high power lasers allow rapid processing and welding of materials and are quickly displacing existing technologies. This is most obvious in the additive manufacturing sector, where the laser sintering of metals allows parts to be constructed with complexities and composites not achievable with any other technique. In the defence sector interest in directed energy applications has also driven the development of very high power laser sources as well as countless other applications.

Optical fibre lasers offer a convenient route to power scaling in a robust architecture and can service many of the above applications. Through total internal reflection, pump and signal can both be waveguided in a fibre laser configuration, this allows long interaction lengths, tight mode confinement and high overlap with active ions. The result of this long and distributed gain medium is high small-signal-gain or low lasing threshold and high laser slope efficiencies. Typically fibre cladding diameters are kept to below ~500μm with device lengths in few to tens of meters, fibre core dimensions are also generally kept to below 20-40μm. From a power scaling perspective this long and thin device format

results in large surface area to doped volume ratio, leading to low thermal load per unit length. The ability to define the transverse lasing mode through waveguiding allows the generation of near perfect beam profiles that show low sensitivity to changes in thermal load. High power fibre lasers generally operate in a 'double-clad' arrangement (Figure 1.1), here the inner core is doped with active ions and intended to guide the lasing mode and a secondary outer-cladding is used to guide pump light. This allows lower brightness diode sources to be launched into the larger area cladding whilst still maintaining single mode operation of the signal.

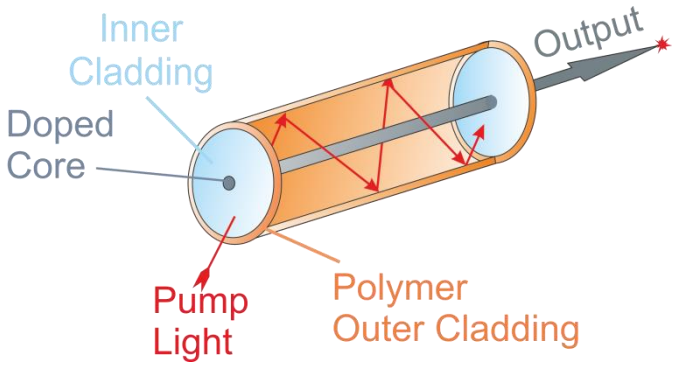

Figure 1.1 A typical double clad optical fibre, showing pump guidance (red) within the cladding (blue region) and signal propagation within the core (grey).

The power scaling of this approach is unrivalled. Over the course of ten years, from the initial demonstration of a near diffraction-limited 1.36kW fibre source in 2004 [1] powers have steadily increased. In 2009, a 10kW single mode source was demonstrated [2], and more recently through the spatial combination of 91 individual kW fibre lasers, 103kW of output power was reported this year (2013) with combined output from a multimode beam delivery showing a beam quality factor of M^2~50 [3]. Perhaps the most impressive achievement of this power scaling is the high level of laser slope efficiency achieved at kW levels, with commercially available sources showing slope efficiencies of 90% under diode pumped operation and output powers of 1.1kW and wavelengths within the ytterbium gain band [4].

Whether operating at the Watt level or kW level the basic fibre laser architecture remains essentially unchanged. In the manufacture of fibre lasers and the individual components that comprise these sources, a high level of automation is used. Techniques and equipment initially developed in the telecoms sector have been repurposed for high power laser development, such as the use of modified chemical vapour deposition (MCVD) for

active fibre manufacture and optical fibre fusion splicers for fibre joining. This use of automated equipment such as the fusion splicer, where the core and cladding of two fibres are aligned and permanently fussed together with sub-micron positional accuracies, greatly simplifies the construction of such high power sources. This allows the rapid production of fibre lasers. Once the initial design has been perfected technicians in production line environments can assemble a well-designed fibre source relatively quickly and repeatedly.

The choice of a fibre laser over other laser architecture is largely dependent on the operating regime. The area in which fibre lasers excel is in high beam quality, high average output power applications. Whilst moderate pulse energies are possible, in comparison to bulk laser arrangements there is no competition. The same advantages that allow efficient CW operation of fibre lasers also put limits on output pulse energy. The tight mode confinement and long interaction length seen in fibre lasers can lead to detrimental nonlinear effects that become particularly pronounced under high peak power operation. On top of this due to high levels of small signal gain, only limited energy storage can be achieved within an active fibre before amplified spontaneous emission (ASE) begins to extract inversion, effectively clamping energy storage. Pulse energies of up to 10's of mJ [5,6] have been demonstrated within fibre sources at nanosecond pulse widths, achieved through the use of exotic cavity arrangements or at the cost of beam quality. However pushing significantly beyond these levels would require a dramatic change in device architecture. This is in comparison to bulk laser cavities where 10's of mJ are regularly achieved and scaling to significantly higher pulse energies is possible by increasing resonator mode size [7].

Whilst fibre lasers will never compete with other laser architecture in terms of pulse energy generation or peak power operation, they do have some unique advantages that have allowed them to quickly gain traction within the industrial sector. Whilst bulk lasers generally show high sensitivity to thermal effects, as we have discussed above, fibre lasers are relatively immune from these same issues and, due to their waveguiding nature, very high beam qualities are possible. The monolithic nature of high power fibre sources is also a strong advantage, alignment free operation is an attractive prospect within an industrial environment where vibration and movement can lead to issues within bulk sources. Long device lifetimes without the need for regular maintenance also add to the attraction of these sources.

In this thesis, we focus on wavelength and mode control within the two-micron wavelength range operating with a thulium-silica fibre gain medium. In a silica host, fluorescence emission from thulium ions can be seen from 1600-2200 nm (Figure 1.2). With wavelength tunability from 1700-2100nm in standard configurations. The operating wavelength range from thulium sources represents an interesting spectral region for a number of reasons. Thulium emission sits within the 'eye-safe[1]' wavelength range from ~1400-2500nm and because of this it is an attractive source for free space applications where laser safety is a concern, such as LIDAR [8] and free space communications [9]. The wavelength range covering the thulium emission band is also a rich region of spectroscopic markers for identification of various chemical species, this is also seen in Figure 1.2 where prominent atmospheric water absorption features are seen from 1800-1950nm. These water absorption features also transfer across to liquid-state water absorption, where a peak in absorption is seen at 1940nm and is an attractive target for medical applications. Other material absorption features also sit within the thulium emission band and can allow the enhanced laser processing and welding of polymers and plastics [10]. Sitting between ytterbium/neodymium (~1μm) and CO_2(~10μm) laser sources, thulium represents an unexplored wavelength range that has yet to be commercially exploited for high power processing applications, and can represent an interesting source for speculative use. From a power scaling perspective in the fibre laser architecture, doubling of propagation wavelength from the 1μm to 2μm allows larger core areas to be achieved for single mode operation. This has the beneficial result of increasing energy storage and thresholds for detrimental nonlinear effects. The lower emission and absorption cross-sections of Tm:silica in comparison to Yb:silica may also represent a route to greater pulse energies within a fibre source.

[1]Eye-safe in this context relates to an increase in maximum permissible exposure (MPE) limits rather than an implication of complete eye safety. Direct exposure of watt level laser sources is still an issue of significant concern regardless of wavelength. The increase of MPE levels within this wavelength range relates to an increase of absorption of these wavelengths within the eye in comparison to short wavelength near IR sources, but also reasonable absorption depths in comparison to longer wavelength sources where cornea damage is likely to occur due to short penetration depths.

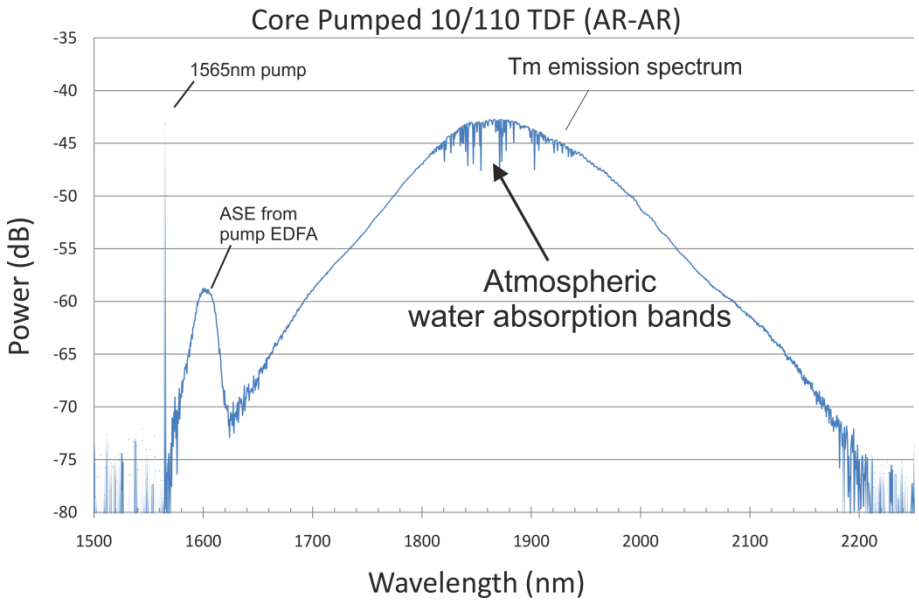

Figure 1.2 Fluorescence emission spectrum from a thulium aluminium co-doped silica optical fibre (The active fibre was core pumped with a single mode 1565nm source and spectral measurements were taken at a 2nm resolution).

1.2 Outline of thesis

In this thesis we explore the wide parameter space fibre lasers can offer, exploiting broad gain bandwidths and novel fibre waveguide behaviours to create sources that show agility in mode of operation of wavelength, bandwidth and beam profile. Throughout this work we highlight promising applications of these sources. The experimental demonstrations reported in this thesis are all achieved in thulium doped silica fibre, but in many instances the concepts presented transfer directly to other active ions and wavelength ranges within the fibre laser architecture.

In Chapter 2 we introduce the relevant background theory for fibre laser operation and power scaling. First we look at the range of rare earth dopants and wavelength coverage available within a silica host, detailing pumping options and operating wavelengths. We then look in more depth at thulium spectroscopy, discussing the various pumping levels and dynamics such as two-for-one cross relaxation. Highlighting, through reference to published literature, the achievable laser slope efficiencies at different pump wavelengths and dopant concentrations. In the final section of this chapter we look at the relevant nonlinear loss processes encountered when power scaling optical fibre lasers and review

core area scaling techniques with an aim to increase the thresholds for detrimental nonlinear effects as well as increasing laser energy storage.

In Chapter 3 we introduce the application of narrow linewidth sources within the 1700-2100nm wavelength range, detailing the use of widely tunable sources for spectroscopic characterisation and components testing as well as highlighting several promising applications within the short wavelength range of the thulium emission band. These include the targeting of C-H absorption features within the 172xnm wavelength range. The targeting of such resonances allows the preferential heating and processing of materials for medical and industrial applications. In the experimental section of this chapter we detail several tunable sources offering a combined wavelength span of >450nm, from 1660nm to 2115nm. Through the use of an electronically tunable wavelength filter we construct core and cladding pumped thulium fibre sources operating from 1700-2115nm, both sources utilising an external cavity arrangement containing an acousto-optic tunable filter (AOTF) and HR mirror. The result is highly reconfigurable wavelength control. This simple arrangement allows high average output powers and broad spectral coverage. Due to the electronically-controllable nature of the AOTF, rapid selection and switching between operating wavelengths is also possible, allowing operation in a non-sequential manner as well as simultaneous selection of multiple wavelengths within the thulium gain band. We extend the short wavelength operation of the core pumped thulium source through the use of a compression-tuned fibre Bragg grating (FBG), allowing high efficiency wavelength dependent feedback and enabling wavelength tuning down to 1660nm. Finally within a fixed wavelength configuration using two static FBG's, we show the high efficiency generation of 1950nm and 1726nm light with single mode beam qualities and output power levels of 14W and 12.6W respectively, operating with laser slope efficiencies of 69% and 63%.

In Chapter 4 we focus on the generation of broad bandwidth, temporally incoherent, amplified spontaneous emission. By exploiting the high small signal gain, and corresponding short pulse-build-up time in a pulsed fibre source, we generate broad bandwidth pulsed ASE light with peak powers of up to 2.2kW. Through the use of a wavelength selective external cavity we extend this source to one of tunable spectral bandwidth and central wavelength. This novel coherence-length-tunable source shows spectral bandwidth control from 24nm FWHM down to 0.3nm, resulting in a change in coherence length from 5mm down to 60μm. As a promising approach for pulse energy

scaling, we apply this source to the suppression of modal interference within a large core multimode fibre amplifier. Here we utilise the broad spectral bandwidth of the ASE seed to suppress the detrimental effects of modal interference. This is demonstrated through the comparison of narrowband and broadband seed amplification. For the narrowband case unstable beam profiles and poor pointing stability is seen. By moving to a broadband seed these detrimental effects are almost completely suppressed, with an increase in beam stability of nearly an order or magnitude. In this multimode amplifier, pulse energies of up to 1.1mJ are generated with peak powers of >20kW. Finally, through the use of highly nonlinear fibre, we utilise the high peak powers of this pulsed ASE source to generate a supercontinuum white light source, covering over an octave in wavelength from 1000nm to 2400nm at output powers of 1.5W.

In Chapter 5 we describe our work towards the selection and operation of individual modes within a multimode fibre laser. Through the combination of a multimode fibre Bragg grating and a free space wavelength selective element, we successfully demonstrate selection of the fundamental mode and next higher order mode in a multimode laser. By making use of AOTF for free space wavelength selection, we are able to rapidly select and switch between guided modes of the multimode fibre, with switching speeds of up to 20kHz and output powers of 5W. This mode agile laser is further extended through the use of modal superposition, by incoherently combining the fundamental Gaussian mode and a donut shaped LP_{11} mode within the laser cavity, we demonstrate the generation of flat-toped beam profiles with electronically selectable 'flatness' as well as other novel shapes.

In Chapter 6 we conclude the work presented throughout this thesis, summarising key results obtained and reiterating the concepts discussed, we pay particular attention towards future routes for laser power scaling whilst still maintaining the broad degree of flexibility as demonstrated in this thesis.

References

1. Y. Jeong, J. K. Sahu, D. N. Payne, and J. Nilsson, "Ytterbium-doped large-core fiber laser with 1.36 kW continuous-wave output power," Opt. Express **12**, 6088 (2004).

2. E. Stiles, "New developments in IPG fiber laser technology," in *5th International Workshop on Fiber Lasers* (2009).

3. E. A. Shcherbakov, V. V Fomin, A. A. Abramov, A. A. Ferin, D. V Mochalov, and V. P. Gapontsev, "Industrial grade 100 kW power CW fiber laser," Adv. Solid-State Lasers Congr. **5**, 5–7 (2013).

4. "Nufern Inc.," http://www.nufern.com/.

5. F. Stutzki, F. Jansen, A. Liem, C. Jauregui, J. Limpert, and A. Tünnermann, "26 mJ, 130 W Q-switched fiber-laser system with near-diffraction-limited beam quality.," Opt. Lett. **37**, 1073–5 (2012).

6. M.-Y. Cheng, Y.-C. Chang, A. Galvanauskas, P. Mamidipudi, R. Changkakoti, and P. Gatchell, "High-energy and high-peak-power nanosecond pulse generation with beam quality control in 200-microm core highly multimode Yb-doped fiber amplifiers.," Opt. Lett. **30**, 358–60 (2005).

7. S. Banerjee, K. Ertel, P. D. Mason, P. J. Phillips, M. Siebold, M. Loeser, C. Hernandez-Gomez, and J. L. Collier, "High-efficiency 10 J diode pumped cryogenic gas cooled Yb:YAG multislab amplifier.," Opt. Lett. **37**, 2175–7 (2012).

8. N. Sugimoto, N. Sims, K. Chan, and D. Killinger, "Eye-safe 2.1-μm Ho lidar for measuring atmospheric density profiles," Opt. Lett. **15**, 302–304 (1990).

9. D. A. Rockwell and G. S. Mecherle, "Wavelength selection for optical wireless communications systems," in *International Symposium on the Convergence of IT and Communications* (2001), pp. 27–35.

10. I. Mingareev, F. Weirauch, A. Olowinsky, L. Shah, P. Kadwani, and M. Richardson, "Welding of polymers using a 2μm thulium fiber laser," Opt. Laser Technol. **44**, 2095–2099 (2012).

Chapter 2.

Background

2.1 Introduction

An optical fibre laser, where both waveguiding and signal amplification occur within the same doped core region, can allow for significant power scaling within a rugged device architecture.

The benefits of light guidance within the doped region include long interaction lengths with tight mode confinement and a high overlap between the active ions and resonator mode. These properties result in high small-signal-gain, low lasing thresholds and excellent power extraction. The long and thin device format results in large surface areas, allowing for efficient heat removal and simplified power scaling. Due to the waveguiding nature it is also possible to ensure single mode operation even at considerable power levels, resulting in near ideal Gaussian beam profiles that are resistant to thermal load and lensing effects.

In this chapter we will investigate the various options for laser dopant and wavelength coverage [1], paying particular attention to thulium spectroscopy and the relevant transitions for power scaling within the two-micron wavelength range. We will briefly discuss the concepts of Gaussian beam propagation in free space and mode guidance within optical fibre [2,3]. Finally, we will discuss the relevant parameters for output power scaling within a fibre laser architecture, highlighting the detrimental effects of relevant nonlinear processes [4] and present the techniques commonly used to mitigate them.

2.2 Rare earth dopants within Silica optical fibre

Power scaling in an optical fibre architecture is almost exclusively achieved within a silica host. This is partially because the pre-existing technology was borrowed from the telecoms sector, where large amounts of money have been spent developing componentry and low loss fibre, but also due its high chemical stability and robustness. In comparison to other glass hosts such as fluoride or germanate glass, silica shows increased damage thresholds and more than double the glass transition temperature (Tg=~1150°C [5]). On top of this leveraging off telecoms technologies, such as the modified chemical vapour deposition (MCVD) process, allow hundreds to thousands of meters of active fibre to be fabricated within a single batch and thus enables relatively low cost production. Transparency of silica is from approximately 400nm to 2400nm with a maximum phonon energy of ~1100cm^{-1}. Within this section we will focus on dopants and transitions relevant to power scaling in this wavelength range and within a silica host (Figure 2.1).

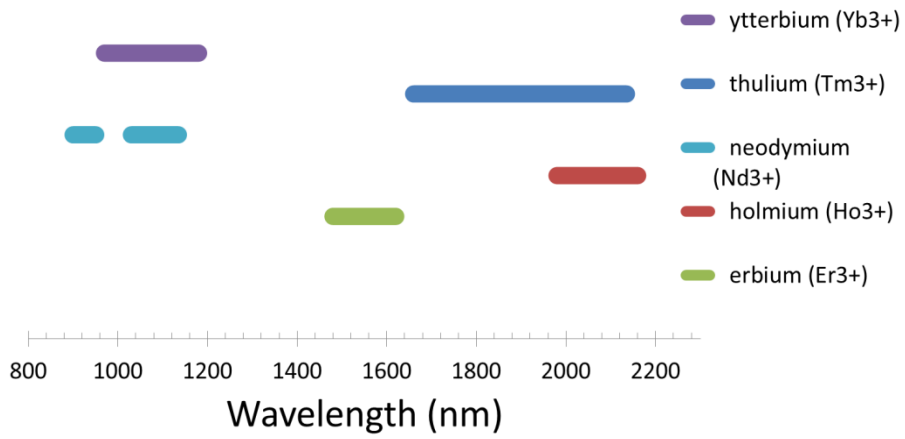

Figure 2.1 Wavelength coverage within silica of several common glass dopants

2.2.1 Ytterbium (1000-1200nm)

Ytterbium doped fibre sources are the most mature in terms of industrial use and power scaling. Ytterbium fibre lasers are generally pumped with diode sources operating at wavelengths of 910nm-940nm and 976nm, with laser operation possible from ~976 - 1180nm [6–8]. For high power operation the lasing wavelength tends to be in the 1060-1080nm range. The low quantum defect between pump and lasing wavelength and the availability of high power laser diodes has ensured wide industry adoption. Commercial systems have demonstrated laser slope efficiencies of nearly 90% at power levels above a

kW [9]. The current power records for single and multimode operation of Yb:fibre sources sit at 10kW[2] [10] and 100kW [11] respectively and represent the highest values reported for any fibre laser operation.

2.2.2 Erbium (1500-1600nm)

Erbium and erbium-ytterbium co-doped fibres operate within the so called 'eye safe' wavelength range, with laser operation demonstrated from 1480-1620nm [12,13], and high power operation generally occurring at wavelengths longer than 1550nm. For Er:silica, optical pumping can be achieved at 975nm and 1470nm. Due to clustering effects limiting doping levels and narrow absorption peaks, Er:fibre is often co-doped with ytterbium in high power situations. This allows the increased solubility and increased absorption cross section of ytterbium to be used for laser pumping, with a non-radiative energy transfer between excited state Yb and ground state Er. Yb sensitization also allows broader pump wavelength operation in the 9xx nm range [14]. The current power record for erbium operation was demonstrated in a cladding pumped Er:Yb co-doped fibre with a maximum power level of 297W at a slope efficiency of 40% at low power, decreasing to 19% at maximum output power [15]. More recently, higher efficiency has been obtained with in-band pumping configurations with laser slope efficiencies of 75% and 80% demonstrated, at output powers of 103W [16] and 18.4W [17] respectively. Both demonstrations were pumped at 1535nm with the former result achieved with multimode diodes and the latter with a single mode fibre source.

2.2.3 Thulium (1700-2100nm)

Thulium fibre sources, pumped at either 79xnm or >~1550nm show laser emission from ~1700-2100nm with maximum output generally achieved at wavelengths of 2000-2040nm. Due to a fortuitous cross relaxation process, when pumping at 79xnm, it is possible to achieve laser slope efficiencies greater than the quantum defect limit (~40%). In this process one pump photon is able to produce two signal photons and allows a significant increase in laser slope efficiency [18]. Power scaling in thulium fibre sources has pushed output powers to 608W within narrow linewidth (<5MHz) operation at a laser slope efficiency of 54% [19]. For broader wavelength operation, a maximum output

[2] At Photonics West 2013 IPG reported 20kW operation with a beam quality of M^2=1.4, few details were given on this source or its design and it is not entirely clear that this is a solely fibre based solution

power of 1.05kW has been reported, operating at a wavelength of 2045nm in a dual-stage amplifier configuration. In this demonstration the single stage amplifier slope efficiency was ~62% (500W output), however the total efficiency reduced to 53% in the dual amplifier configuration [20]. Thulium fibre sources are an attractive alternative to high power erbium fibre sources for operation in the 'eye safe' wavelength range. This is due to a greater ease in power scaling as is evident in demonstrated output powers. The broad wavelength coverage (>400nm) of thulium sources also make it attractive for targeted spectroscopic applications, where sources can be tailored to specific absorption features.

2.2.4 Holmium (2000-2200nm)

Holmium doped fibre lasers operate in the in the 1990-2180nm wavelength range [21,22] with options to pump at ~1150nm or 1900-2000nm [23]. In-band pumping with high-brightness thulium sources is seen as a promising route to power scaling of holmium sources. Single mode operation of a 400W oscillator has recently been demonstrated at an operating wavelength of 2120nm. This source was a double clad holmium doped fibre, cladding pumped by an array of single mode thulium sources in a high core to clad area ratio configuration, and operated with a slope efficiency of ~40% [24]. Previous demonstrations using a similar approach have yielded slope efficiencies of up to 66% [25,26].

2.2.5 Other dopants

Other dopant options for extended wavelength coverage using silica as the host include neodymium for operation in the 900 - 940nm – 1060 - 1140nm wavelength ranges [27–30], as well as Bi doped silica for operation in ~1200-1500nm [31,32]. Finally, exploiting nonlinear processes, stimulated Raman Scattering (SRS) can provide power scaling at wavelengths not accessible to other sources. With the recent demonstration of 301W of single mode output power operating at a wavelength of 1480nm, pumped with ~470W of 1117nm and corresponding to a conversion efficiency of 64% [33].

In this thesis we will mainly focus on thulium as the laser gain material, however many of the concepts presented are independent of dopant and can be equally applied to other dopants and laser wavelengths.

2.3 Thulium spectroscopy

In a silica host, florescence emission of the $^3F_4$-$^3H_6$ transition of thulium can be seen from 1600-2200nm (Figure 2.2) with a large proportion of this emission band covered by fixed wavelength and tunable thulium sources. In-band pumping directly to the upper laser level ($^3F_4$) is possible using sources operating at wavelengths around the ~1650nm absorption peak. Here due to the low quantum defect (<20%) high efficiency lasing is possible and is attractive from a thermal loading perspective. In practice this is commonly achieved with high brightness Er:Yb fibre laser sources at wavelengths >1560nm, with 412W demonstrated using this approach at a slope efficiency of ~60% [34]. Tandem pumping schemes (thulium pumped thulium) are also an interesting approach for power scaling within a thulium source. Very recent results investigating low quantum defect in-band pumping have produced impressive results. With laser slope efficiencies of 90% demonstrated for 1908nm pumping and 2005nm lasing at power levels of 1.5W [35].

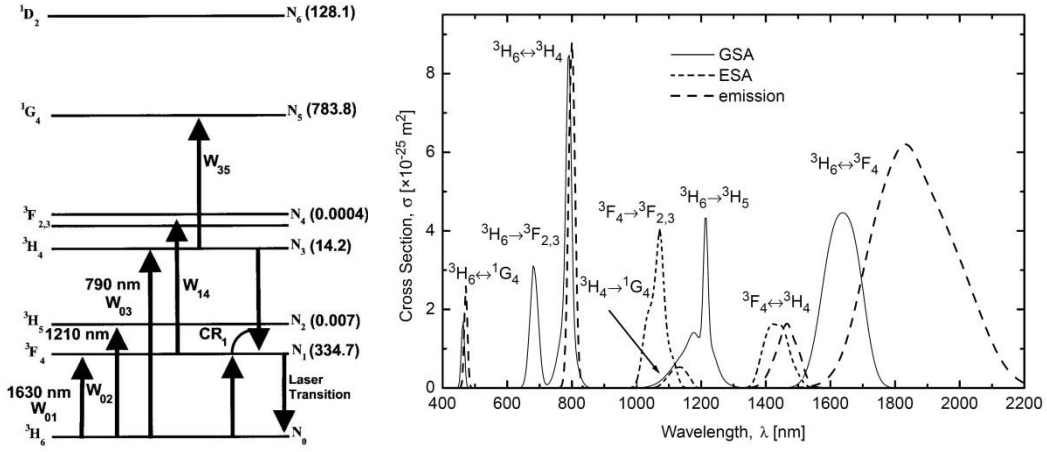

(a) (b)

Figure 2.2 (a) Energy level diagram [36] and (b) absorption and emission cross-sections [36,37] for Tm-doped silica.

79xnm diode sources can be used to excite the $^3H_4$ manifold. From here several routes can be taken to populate the $^3F_4$ level, multi-phonon decay can lead to non-radiative relaxation into the upper laser level, spontaneous emission of 1470nm light can also allow the depopulation of this level, however it is of lower probability. It is also possible for a cross relaxation process to occur between neighbouring Tm ions. Here decay from the $^3H_4$ level is achieved via resonant energy transfer with a neighbouring unexcited Tm ion, with the decay of the primary Tm ion from $^3H_4$ to $^3F_4$ resulting in an excitation of the second Tm

ion from the ground state ($^3H_6$) to the upper laser level. This process is a very attractive one as it allows for one pump photon to excite two signal photons, thus doubling the pumping quantum efficiency. The probability of this cross relaxation process occurring is dependent on the mean distance between neighbouring Tm ions, with higher thulium concentration enhancing the cross relaxation process [38]. However as thulium concentration is increased detrimental processes begin to become significant such as energy transfer upconversion and excited state absorption. In a silica host an optimum thulium concentration of 3.5-4wt% thulium has been experimentally shown and has resulted in laser slope efficiencies of upward of 70% under 795nm pumping [39], corresponding to a pumping quantum efficiency of 1.8 times the quantum limit.

2.4 Optical fibre waveguides and beam propagation

2.4.1 Optical fibre waveguides

Optical fibre waveguides, generally consisting of a cylindrical core region surrounded by a glass cladding layer that is then buffered by a polymer layer, provide an attractive approach for laser signal propagation. The core region of the optical fibre is doped such that the refractive index is greater than the surrounding cladding and allows waveguiding via total internal reflection. The cladding region provides mechanical rigidity to the core region and the polymer buffer layer serves to prevent contamination and contact with the bare glass. Depending on fibre design, the cladding region can be guiding or anti-guiding for single or double clad operation (Figure 2.5) and generally this is achieved with either a low index or high index polymer buffer layer.

The acceptance angle of an optical fibre is defined by the magnitude of the refractive index step between the core and cladding and is related to the optical fibre's numerical aperture (*NA*) as $NA=n_0 sin\theta$, where n_0 is the refractive index of the transitioning medium (generally air) and θ is the acceptance angle of the fibre. For a core refractive index (n_{core}) and cladding refractive index (n_{clad}) the numerical aperture of a step index fibre is given by [3]:

$$\mathrm{NA} = \sqrt{n_{core}^2 - n_{clad}^2} \tag{1}$$

In the ray picture of optical fibre propagation, for a given core size, the number of ray paths guided increases for increasing NA. These ray paths combine to form allowed

electromagnetic field distributions or modes within the fibre. The number of guided modes within a fibre is determined by the V parameter or normalised frequency parameter. The V parameter of a circular step index waveguide is given by [40]:

$$V = \frac{2\pi}{\lambda} rNA \tag{2}$$

where r is the waveguide radius and λ is the propagating wavelength. For V<2.405 the fibre can guide only the fundamental mode, whose profile closely matches that of a Gaussian intensity distribution, with the number of guided modes increasing for V>2.405.

To gain insight into the modal dispersion behaviour in increasingly multimode fibre we first define a normalised propagation constant:

$$b = \frac{(\beta/k)^2 - n_{clad}^2}{n_{core}^2 - n_{clad}^2} = \frac{n_{eff}^2 - n_{clad}^2}{n_{core}^2 - n_{clad}^2} \tag{3}$$

where β is the mode propagation constant, $k= 2\pi/\lambda$ and n_{eff} is the effective index of the guided mode. In Figure 2.3 we can see both the increasing number of guided modes and decreasing effective index spacing of the guided modes for an increasing V-number. As can be seen , above the single mode cut-off (V>2.405) the LP_{11} mode can begin to guide and as V number is further increased the fibre becomes progressively more multimode. Above the single mode cut-off steps must be taken to suppress higher order modes if Gaussian beam propagation is desired.

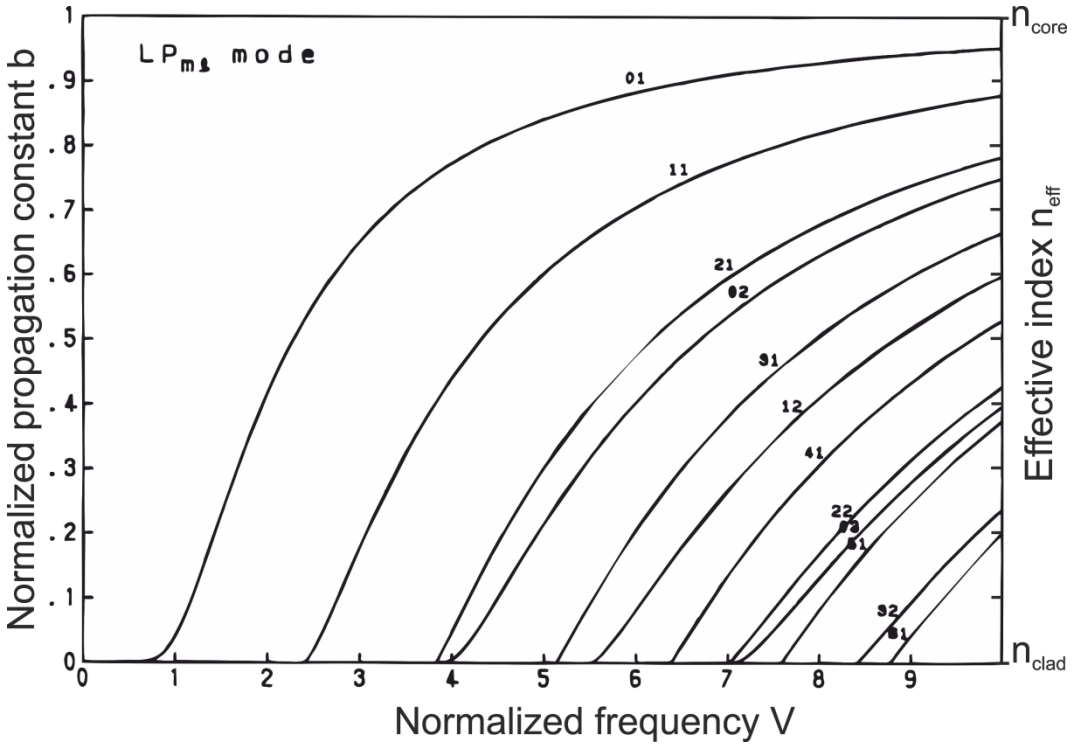

Figure 2.3 Propagation constant and number of guided modes for increasing V-number of a step index fibre [3].

As the V-number of an optical fibre is increased the strength of mode confinement of the fundamental mode also increases. The mode field diameter (MFD) of the fundamental mode within a step index fibre (at the $1/e^2$ point) can be related to the fibre core diameter and V-number by the approximation [41]:

$$\omega_0 = r\left(0.65 + \frac{1.619}{V^{3/2}} + \frac{2.879}{V^6}\right) \tag{4}$$

In Figure 2.4 we plot this approximation alongside the calculated (Optifibre) values of mode field diameter within a step index fibre, here we can see a close agreement between approximation and calculated values. From Figure 2.4 we can see that mode confinement, although initially weak, asymptotes to a value of ~70% of the fibre core diameter within an unbent fibre.

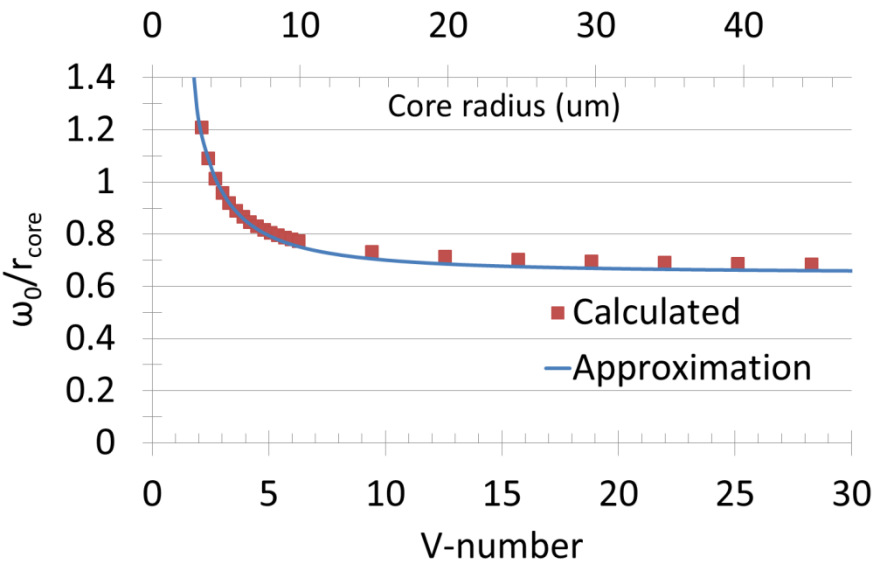

Figure 2.4 Normalised fundamental mode confinement for increasing V-number and core diameter (for λ=2μm & NA=0.2).

2.4.2 Gaussian beam propagation and beam quality

For a Gaussian beam propagating in free space, the beam waist radius (at the 1/e2 point) after a distance z is given by [2]:

$$w(z) = w_0 \left[1 + \left(\frac{\lambda z}{\pi w_0^2}\right)^2\right]^{\frac{1}{2}} \tag{5}$$

where, w_0 is the minimum beam waist radius and λ is the propagating wavelength. From the waist position we define the Rayleigh range (z_0) as the distance at which the beam waist has expanded to $\sqrt{2}$ times its initial value, i.e. the point at which $w(z_0) = \sqrt{2}w_0$. From (5) we can see:

$$z_0 = \left(\frac{\pi w_0^2}{\lambda}\right) \tag{6}$$

For non-diffraction-limited Gaussian beams, a beam propagation factor or M^2 can be used to describe the divergence and propagation behaviour relative to a diffraction-limited fundamental mode beam. M^2 is defined as the ratio of beam parameter product ($BPP=\theta.w_0$ where θ is the far field divergence) to the BPP of a diffraction limited fundamental mode beam ($=\lambda/\pi$). Rearranging this into (5) we get:

$$w(z) = w_0 \left[1 + \left(\frac{M^2 \lambda z}{\pi w_0}\right)^2\right]^{\frac{1}{2}} \tag{7}$$

Here we can see, beams with non-diffraction-limited behaviour essentially behave as diffraction-limited beams of increased wavelength. The brightness of a propagating beam is defined as the ratio of beam power over the beam area and solid angle far field divergence, as given by [42]:

$$B = \frac{P}{A_e \Omega_e} = \frac{P}{\pi w_o^2 \pi \theta^2} = \frac{P}{M_x^2 M_y^2 \lambda^2} \tag{8}$$

For multimode waveguides, we can approximate the beam quality factor of a fully filled waveguide as:

$$M^2 = \frac{\pi w_0 \theta}{\lambda} \approx \frac{\pi r}{\lambda} \sin^{-1}\left(\sqrt{n_{core}^2 - n_{clad}^2}\right) \approx \frac{\pi r}{\lambda} NA \tag{9}$$

2.4.3 Double clad fibre lasers

The first demonstrations of modern optical fibre lasers relied on core pumping technologies, where high brightness pumps (generally diode based) were guided within the same doped core as the lasing mode. This approach has limited power scalability due to the high brightness required from the pump source. A solution to this limitation was found in using a cladding pumping architecture [43]. Here the active fibre has two nested waveguides. The first waveguide, the inner core, is designed to be single mode and doped with active ions. The second waveguide, the cladding, is designed to be multimode with a diameter roughly an order of magnitude greater than the core. This allows lower brightness pump sources to be coupled into the cladding of the active fibre and absorbed by the doped core whilst traversing the length of the fibre. This reduces the cost of pump sources and greatly increases the laser power scalability through the use of low brightness, high power diode bars and stacks. In this way the double clad fibre becomes a brightness converter, taking the low brightness pump sources and converting them into high brightness signal light.

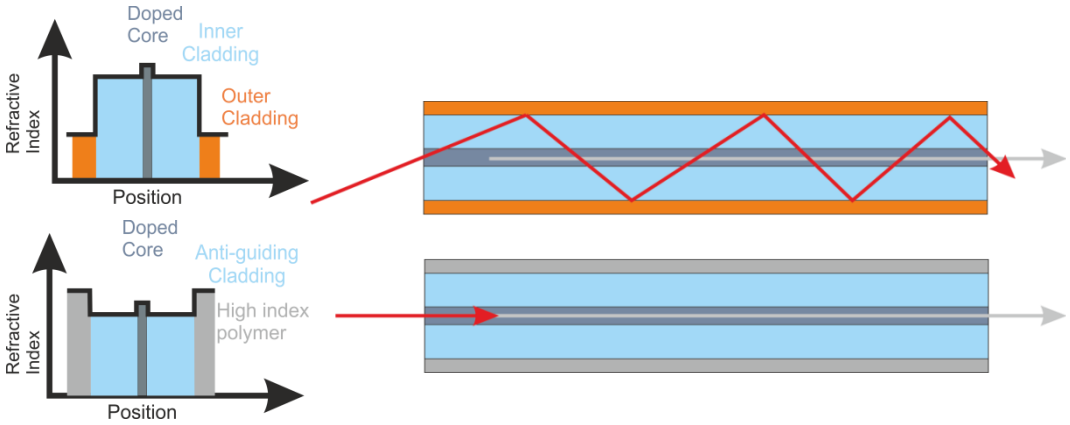

Figure 2.5 Refractive index profile and conceptual cross sections of double clad fibre (top) and single clad fibre (bottom).

To ensure efficient absorption in the core for pump light coupled into the multimode cladding, some modifications to the cladding geometry must be made. Double clad fibres, with circular outer cladding and central doped core have lower pump absorption than would initially be expected given the area ratios of the core and cladding. This is due to excitation of modes within the cladding that have a small spatial overlap with the doped core. These modes can be thought to take on a helical path about the core area and therefore do not interact with the doped active fibre sufficiently to be absorbed (Figure 2.6(b)). This results in some fraction of unabsorbed pump power even for increased fibre length. To combat this effect it is possible to fabricate the fibre with the active core offset from the centre of the cladding. To be effective the core has to be placed significantly off centre, and in practice this leads to difficulties in fibre fabrication and splicing. An alternative to this is to produce a non-symmetric cladding. The idea of this approach is to break the symmetry needed for helical ray propagation. A ‘D-shaped’ outer cladding is a simple and effective solution to enhance pump absorption within the double clad fibre (Figure 2.6(c)). To facilitate fibre fusion splicing other, more symmetric shapes such as octagonal geometries can be used (Figure 2.6(a)). For this approach, a compromise is made between fibre splicing and pump absorption. In addition to shaped claddings it is possible to introduce doped glass sections within the cross section of the fibre cladding (Figure 2.6(d)). A common dual-purpose approach is found in polarisation maintaining fibres, where low index stress rods are inserted into the fibre preform prior to drawing. This serves to both increase pump absorption due to breaking up of the fibre symmetry and also induces birefringence into the core of the waveguide due to a thermal expansion

mismatch between the ‘stress rods’ and the cladding glass leading to a stress optic effect within the core.

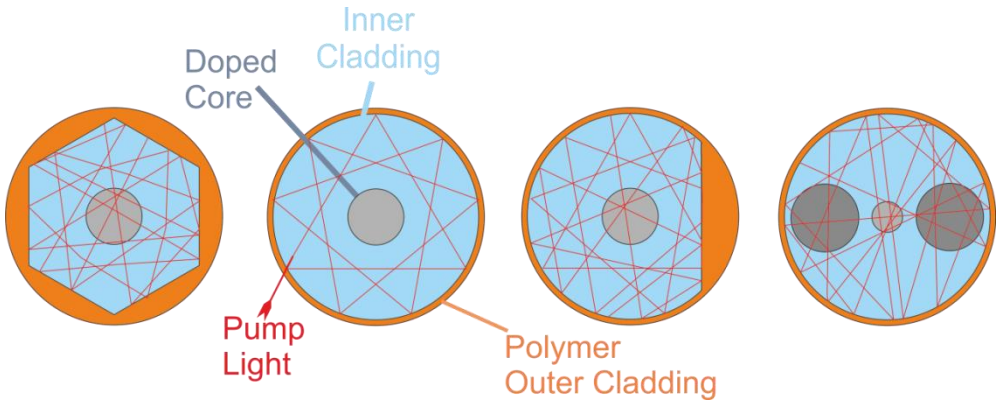

Figure 2.6 Several common double clad fibre cross sections, (a) octagonal, (b) standed step index, (c) D-shaped double clad fibre and (d) polarisation maintaining ‘PANDA’ type.

2.5 Considerations for power scaling in optical waveguides

When power scaling with a fibre architecture issues arise that would not normally be seen in free space bulk laser configurations. The high small signal gain commonly seen within waveguided gain media leads to problems associated with parasitic amplified spontaneous emission (ASE), particularly under low repetition rate pulsed operation, where energy storage is effectively clamped by the onset of ASE. Even with the energy storage limitations associated with ASE, intensities of the guided mode within a fibre laser source can approach levels in the GW/cm^{-2}. This is due to tight mode confinement of the waveguide and is compounded by the long interaction lengths that are typical of active fibres. Because of this, nonlinear interactions that would not normally be seen at equivalent power levels within a bulk laser medium can become significant and can eventually lead to catastrophic damage through dielectric breakdown of the glass itself. In this section we will discuss these effects, highlighting the major concerns and referring to the common approaches for alleviating them.

2.5.1 Pulsed laser operation

The tight mode confinement and high spatial overlap between dopant and propagating laser mode within a fibre laser leads to a high small signal gain and low lasing threshold. Whilst this is advantageous under CW operation, where low thresholds and high conversion efficiencies are seen, from an energy storage perspective this is problematic. In pulsed operation, where feedback is suppressed and inversion is allowed to build-up, small signal gain can become very high. So much so that even the small levels of spontaneous emission from the excited ions become significantly amplified. Eventually this amplified spontaneous emission will clamp the inversion for low repetition rate operation and put an upper limit on energy storage within the fibre. This is in comparison to a bulk laser, where the onset of ASE clamped behaviour is at much higher levels, allowing significantly higher energy storage before ASE becomes an issue.

As a rough rule of thumb, fibre lasers can operate up to approximately 10 times the saturation energy before the onset of ASE clamped behaviour [44]. With the saturation energy given by:

$$E_{sat} = \frac{A_{co} h\nu_L}{\eta_S\left(\sigma_e(\lambda_l) + \sigma_a(\lambda_l)\right)} \tag{10}$$

where A_{co} is the area of the doped core, $h\nu_L$ is the photon energy at the lasing wavelength, η_S is the overlap between the dopant and the guided mode and $\sigma_e(\lambda_l)$ & $\sigma_a(\lambda_l)$ are the emission and absorption cross-sections of the dopant at the lasing wavelength. From eq.(10) we can see that we have several options for increasing saturation energy and hence extractable energy storage within the fibre. First, provided sufficient pump power is available, it is advantageous to operate on a wavelength or dopant where effective cross section ($\sigma_e(\lambda_L)+\sigma_a(\lambda_L)$) is low. It is also possible to reduce signal overlap (and increase E_{sat}) through novel doping profiles, such as ring doping away from the mode centre [45]. Core area scaling also has the effect of increasing E_{sat} and is perhaps the easiest of the approaches to implement, although not without its own issue such as increasing modal content etc. as will be discussed within the following sections.

2.5.2 Nonlinear effects

Interaction of propagating light through inelastic scattering of the glass host leads to phonon excitation within the glass lattice. As the intensity of propagating light increases these phonon driven processes can become significant and lead to strong nonlinear interaction between the glass and propagating mode. In this section we will look at several prominent nonlinear processes (or limitations) for high power propagation within an optical waveguide.

Stimulated Brillouin scattering

Stimulated Brillouin scattering (SBS) is a nonlinear process that involves the excitation of an acoustic wave through sufficiently intense incident light, leading to the generation of a Stokes-shifted, backward-propagating wave that can contain a large proportion of the incident power. SBS can be very problematic for single frequency and pulsed fibre operation, often leading to catastrophic damage of components or the fibre itself.

Through electrostriction, propagating light can excite an acoustic wave within the optical fibre. In turn this acoustic wave leads to refractive index modulations of the glass and the formation of a traveling-wave Bragg grating. The incident (pump) light is then scattered from this grating with a Doppler shift dependent on the acoustic wave propagation velocity ($v_a \approx 6000 m/s$ in silica [4]) and the excitation wavelength. The frequency of the excited acoustic wave (and hence Doppler frequency shift) in a medium of refractive index n is given by:

$$\nu_B = \frac{2n\nu_a}{\lambda} \tag{11}$$

With typical values of $\nu_B \approx 18GHz$ ($\lambda = 1\mu m$) and $\nu_B \approx 9GHz$ ($\lambda = 2\mu m$). The Brillouin gain bandwidth and gain coefficient in fused silica are approximately $\Delta\nu_b \approx 50\text{-}100MHz$ and $g_B \approx 0.5 \times 10^{-11}\ m/W$ [4] with actual values dependent on fibre geometry and dopants. For spectral bandwidths greater than $\Delta\nu_b$ the effective Brillouin gain is given by:

$$g_{Beff} = \frac{\Delta\nu_b}{\Delta\nu_b + \Delta\nu_{laser}} g_B \tag{12}$$

As the laser spectral bandwidth increases g_{Beff} quickly decreases in value. The threshold for SBS can be approximated by [4]:

$$P_{th}^{SBS} = \frac{21A_{eff}}{g_{Beff}l_{eff}} \tag{13}$$

where l_{eff} is the effective interaction length of the propagating mode, as given by $l_{eff} = \frac{1-e^{-\propto L}}{\propto}$ where L is the fibre length and α is the loss (or gain) coefficient of the fibre at the SBS pump wavelength. A_{eff} is the effective area of the propagating mode calculated from eq.(4) for the fundamental mode.

Due to the high spatial overlap between the acoustic wave and guided mode as well as a long interaction length, it is possible for the back reflected Stokes wave to contain a large fraction of the incident (pump) power. Within fibre amplifier systems such as the MOPA, this effect can be disastrous, with strong amplification of the backward propagating wave (particularly in co-pumped configurations) often leading to catastrophic damage of pump diodes and other in-line components.

The timescales and bandwidths associated with SBS are related to the acoustic wave build-up time and are of the order of ~10ns. For pulse widths below this, thresholds for SBS can increase dramatically and other nonlinear effects such as stimulated Raman scattering become more prominent.

As we can see from above, SBS can be a major issue for single frequency propagation and amplification within fibre lasers. If significant power scaling is to be achieved, or long fibre propagation lengths are desired, steps must be taken to avoid the detrimental effects of SBS. Such approaches include the use of width fluctuations [46] or thermal gradients [47] along the length of the fibre, which have the effect of broadening the SBS gain bandwidth. It is also possible to reduce the overlap between acoustic and optical modes through acoustic index tailoring of the waveguide [48].

Eq.(13) allows a very rough approximation of SBS threshold and can be used as a ball-park figure, however the individual parameters will change considerably due to material properties and fluctuations. In practice, the back reflected Stokes wave is often monitored in laser or amplifier systems and power scaling halted if rapid increases in back reflected power is seen.

Stimulated Raman scattering

Stimulated Raman scattering (SRS) is an optical phonon driven process where incident light of sufficient intensity leads to an excitation of molecular bond resonances (in silica optical fibre Si-O bonds). This process is similar to SBS but the energy of the excited phonons is much higher and is referred to as optical phonon excitation rather than acoustic photon excitation. In this process photon energy is lost to lattice phonons and thus the transmitted light is Stokes-shifted to longer wavelengths.

Under low intensity propagation this process is relatively weak, however as intensity and interaction length increase energy conversion from this process can become very significant.

Again, as was the case for Brillouin gain bandwidth and coefficient, the values for Raman gain bandwidth and gain coefficient are material dependent but we can get an idea of the behaviour by taking the values for bulk fused silica. In this host the Raman gain spectrum spans from $\Delta\nu_R \approx 0\text{-}18THz$ with a peak at $\Delta\nu_r \approx 13.2THz$ and peak gain of $g_R \approx 1x10^{-13}$ m/W (at λ=1064nm and assuming linear polarisation [49]). The Stokes frequency shift associated with Raman scattering is ~44nm for λ=1μm and ~176nm for λ=2μm. The threshold for SRS is approximately given by [50]:

$$P_{th}^{SRS} = \frac{16A_{eff}}{g_R l_{eff}} \tag{14}$$

SRS is a cascading process, with 1st order Stokes shifted light able to generate a 2nd order, 3rd order etc. Stokes shifted signal as the power increases. In some situations, the effects of SRS can be exploited, allowing distributed amplification or access to otherwise difficult to reach spectral areas [33,51].

When propagating light within an active fibre SRS has two detrimental aspects. Firstly, by virtue of the frequency shift, the propagating light can be shifted in wavelength outside the gain band of the dopant, leading to an effective gain lower than would be seen otherwise. Secondly, the energy difference between the pump and Stokes signal is lost as heating within the lattice. This is in addition to the potential of running into increased material or component absorption at longer wavelengths.

Comparison of SBS and SRS effects

Here we can see that SRS can essentially be thought of as a loss process, with heat generation from the Stokes frequency shift as well as any light loss due to increased material absorption. Whilst SBS is a much more detrimental process within fibre lasers, the back reflected signal light can be further amplified within the gain medium and be incident on pump diodes that are generally very susceptible to facet damage from excess light. Furthermore, as SBS can be a cascaded process with multiple reflections backward and forward amplification can be multi-pass, greatly increasing peak power and potentially leading to catastrophic damage within the fibre.

2.5.3 Optical damage

Another prominent issue within fibre lasers (particularly pulsed sources) is the dielectric breakdown of the waveguide material. Here, for sufficiently intense light, ionisation and plasma formation can occur in the glass leading to a thermal runaway and catastrophic damage of the glass fibre. Although values within literature show some variability both on damage threshold and pulse width scaling factor [52]. For uncoated bulk silica illuminated with ps-ns pulse widths at a wavelength of 1064nm we can estimate the bulk damage threshold of silica as [53]:

$$P_{max} = I_{th}A_{eff} \approx \frac{X * A_{eff}}{\sqrt{\tau}} \tag{15}$$

where P_{max} defines the upper limit of propagating power, $X = 1.5kW \cdot ns^{0.5}/\mu m^2$ and τ is the pulse width expressed in ns . In general the most susceptible point of an optical fibre is the transition from optical fibre waveguiding to free space. Here small defects at the glass surface are suspected to lower the glass damage threshold in comparison to the bulk material. To mitigate this effect is it possible to effectively increase this damage threshold by first expanding the beam whilst still within the glass. In this situation a section of fused silica can be bonded directly to the fibre end-face, generally this takes on the form of a coreless optical fibre, commonly referred to as an ‘end-cap’. Assuming a diffraction-limited fundamental mode beam, the increase in the mode field radius as a function of end-cap length is approximately given by:

$$w(z) \approx \frac{L * NA}{n_{clad}} + r_{core} \tag{16}$$

With *w(z)* limited to ~2/3 of the end-cap radius to prevent significant diffraction losses from the end-cap boundary.

2.5.4 Other nonlinear considerations

As both SBS and SRS are proportional to area/length, increasing the core size can be an effective means of suppressing these detrimental effects, however an upper limit on peak power within a waveguide is set by the self-focusing limit. Here, due to the Kerr nonlinearity, focusing of the propagating mode starts to occur. As this further increases beam intensity this process becomes a runaway effect and will eventually lead to optical damage of the waveguide, with critical power given by [54]:

$$P_{crit} = \frac{0.146\lambda^2}{nn_2} \tag{17}$$

where n_2 the nonlinear refractive index (~2.7 x 10^{-20} m^2/W in silica [55]) with the self-focusing limit ~4MW for λ=1μm and ~16MW for λ=2μm.

2.6 Mode area scaling

As we have seen in the previous sections, to increase laser output powers within an optical fibre laser, mode area must be scaled. This allows the reduction in the detrimental effects of nonlinear processes and within pulsed systems allows the increase of pulse energy storage and extraction. By increasing the effective area of the propagating mode the thresholds for both SBS and SRS are increased, as well as the threshold for glass damage.

From Figure 2.3 and eq.(2) we can see for increasing core area eventually the conditions for higher order mode propagation are met and the waveguide is no longer strictly single mode. When the core area is scaled several approaches can be taken to suppress the onset of higher order mode guidance. Low NA fibres, where core numerical aperture is decreased as core size is increased, allow scaling of core area in the strictly single mode regime. It is also possible to operate with V-numbers slightly higher than single mode

cut-off by taking advantage of differences in bend loss between the fundamental and higher order modes under coiled fibre operation. Other approaches that can be taken include; the use of specialised launch arrangements to excite only a single mode (fundamental or higher order) or introducing resonant (or anti-resonant) structures to the waveguide that preferentially couple to and cause loss to higher order modes. Within this section we will briefly discuss several of these approaches.

2.6.1 Low NA fibres

Step index

From eq.(2) it follows that to maintain a fixed V-number for increasing core size then core numerical aperture must be reduced. Fabrication tolerances during doped fibre manufacture put a practical lower limit of ~0.06NA for solution doping techniques. This lower limit of NA results in core diameters of 12.8 & 25.5μm at wavelengths of 1μm & 2μm if true single mode guidance is required. In practice it is possible to scale core beyond this point and still maintain single mode beam quality. By exploiting the increased bend loss for higher order modes within few mode fibres, it is possible to coil the active fibre to a diameter that results in significant bend-loss for higher order modes whilst still allowing relatively low loss fundamental mode propagation [56,57]. Using this approach, commercially available [9] step index fibres with core diameters of 25μm or more have demonstrated near perfect beam quality (at operating wavelengths of ~1μm and corresponding to an equivalent of ~50μm diameter for 2μm propagation). As core size is further scaled with this approach the difference in bend loss between the fundamental mode and higher order modes becomes less prominent, putting an upper limit on distributed bend loss mode filtering [58].

Microstructured fibres

The lower limit of core NA is due to the fabrication tolerances achievable with MCVD fibre manufacture. Microstructured fibre, where rather than having a defined core, a series of high index or low index rods (or air holes) are used as sub wavelength features to define an effective refractive index profile. This is a much more versatile approach to fibre refractive index design and allows much lower core NA's to be fabricated. Using this approach core NA's as low as 0.02 [59] are commercially available. More sophisticated designs such as confined doping (to match the MFD of guided mode rather

than core diameter, Figure 2.4(b)) are also commonly used. Commercially available microstructured fibres demonstrate core diameters up to 100μm whilst still maintaining single mode guidance. Reduction of fibre core NA to such extreme levels however comes at a cost to the strength of mode confinement. As these fibres are very weakly guiding, mode skew and bend loss effects become significant [58] issues and such extreme core diameters must be kept straight. Often, these fibres are fabricated with cladding diameters of >1mm, resulting in inflexible rod type fibres and limiting their ability to integrate into commercial systems.

The high dopant concentrations and large core areas often seen in microstructured fibre designs as well as the resulting short device lengths (~1m), lead to higher energy storage and lower nonlinear effects. Due to these properties microstructured fibres excel in short pulse operation, with the current pulse energy records (26mJ for single mode output) obtained with large mode area rod type fibres in MOPA configurations [60].

More recently, detrimental effects associated with the weakly guiding nature of these fibres have started to emerge, such as thermally induced mode coupling and instability [61] leading to a threshold like onset of beam quality degradation and higher order mode excitation.

2.6.2 Single mode propagation within a multimode fibre

Provided mode coupling is sufficiently weak within a low scattering optical fibre, it is possible to use different launch techniques to couple into a single mode of a multimode fibre and propagate some distance along the fibre without significant beam quality degradation.

First demonstrated by Fermann [62] through the use of free space launch and mode matching into the fundamental mode, propagation of a fundamental mode within a multimode waveguide was demonstrated. In practice this is a difficult technique to achieve and imperfect launching results in some excitation of higher order modes, in a passive fibre this is not a significant issue. However in active fibre amplifiers, where unsaturated gain within the wings can be significant, this leads to degradation of laser beam quality. By using high precision fibre fusion splicing techniques it is possible to negate the need for free space launching and move from a single mode fibre to a multimode fibre in an all glass format. This can be achieved through the use of a fibre

taper. Here the larger core fibre is tapered down in diameter so that the mode field diameters of the two fibres match. At this point the tapered fibre is cleaved and spliced to the smaller core fibre. This approach is commonly used in combination with distributed bend loss within solid core fibres to allow near single mode propagation of otherwise multimode fibre.

2.6.3 Resonance structures for mode filtering

Other novel designs have been implemented such as secondary resonance elements that match propagation of higher order modes, causing an increased loss for all but the fundamental [63] or through the use of leakage channel that again provide loss for higher order modes [64]. However these approaches are less common, and to date published work has been limited.

References

1. M. J. F. Digonnet, *Rare-Earth-Doped Fiber Lasers and Amplifiers* (CRC Press, 2001), p. 777.

2. B. E. A. Saleh and M. C. Teich, *Fundamentals of Photonics* (John Wiley & Sons, 1991), Vol. 5.

3. K. Okamoto, *Fundamentals of Optical Waveguides* (Academic Press, 2005), p. 561.

4. G. Agrawal, *Nonlinear Fiber Optics* (Academic Press, 2001), p. 467.

5. A. Méndez and T. Morse, *Specialty Optical Fibers Handbook* (2011).

6. A. Shirakawa, H. Maruyama, K. Ueda, C. B. Olausson, J. K. Lyngsø, and J. Broeng, "High-power Yb-doped photonic bandgap fiber amplifier at 1150-1200 nm.," Opt. Express **17**, 447–54 (2009).

7. D. C. Hanna, R. M. Percival, I. R. Perry, R. G. Smart, P. J. Suni, and A. C. Tropper, "An Ytterbium-doped Monomode Fibre Laser: Broadly Tunable Operation from 1.010 μm to 1.162 μm and Three-level Operation at 974 nm," J. Mod. Opt. **37**, 517–525 (1990).

8. R. Royon, J. Lhermite, L. Sarger, and E. Cormier, "High power, continuous-wave ytterbium-doped fiber laser tunable from 976 to 1120 nm," Opt. Express **21**, 13818–13823 (2013).

9. "Nufern Inc.," http://www.nufern.com/.

10. IPG, "IPG photonics," http://www.ipgphotonics.com/.

11. E. A. Shcherbakov, V. V Fomin, A. A. Abramov, A. A. Ferin, D. V Mochalov, and V. P. Gapontsev, "Industrial grade 100 kW power CW fiber laser," in *Advanced Solid-State Lasers Congress* (OSA, 2013), p. ATh4A.2.

12. A. Bellemare, M. Karbsek, C. Riviere, F. Babin, V. Roy, and G. W. Schinn, "A broadly tunable erbium-doped fiber ring laser: experimentation and modeling," IEEE J. Quantum Electron. **7**, 22–29 (2001).

13. Q. Wang and Q. Yu, "Continuously tunable S and C+ L bands ultra wideband erbium-doped fiber ring laser," Laser Phys. Lett. **610**, 607–610 (2009).

14. M. Laroche, S. Girard, J. K. Sahu, W. A. Clarkson, and J. Nilsson, "Accurate efficiency evaluation of energy-transfer processes in phosphosilicate Er3+-Yb3+-codoped fibers," J. Opt. Soc. Am. B **23**, 195 (2006).

15. Y. Jeong, S. Yoo, C. A. Codemard, J. Nilsson, J. K. Sahu, D. N. Payne, R. Horley, P. W. Turner, L. Hickey, A. Harker, M. Lovelady, and A. Piper, "Erbium:Ytterbium Codoped Large-Core Fiber Laser With 297-W Continuous-Wave Output Power," IEEE J. Quantum Electron. **13**, 573–579 (2007).

16. M. A. Jebali, J.-N. Maran, S. LaRochelle, S. Chatigny, M.-A. Lapointe, and E. Gagnon, "A 103W High Efficiency In-Band Cladding-Pumped 1593 nm All-Fiber Erbium-Doped Fiber Laser," Conf. Lasers Electro-Optics JTh1I.3 (2012).

17. E.-L. Lim, S. Alam, and D. J. Richardson, "Optimizing the pumping configuration for the power scaling of in-band pumped erbium doped fiber amplifiers.," Opt. Express **20**, 13886–95 (2012).

18. S. D. Jackson, "Cross relaxation and energy transfer upconversion processes relevant to the functioning of 2 μm Tm3+-doped silica fibre lasers," Opt. Commun. **230**, 197–203 (2004).

19. G. D. Goodno, L. D. Book, and J. E. Rothenberg, "Low-phase-noise, single-frequency, single-mode 608 W thulium fiber amplifier," Opt. Lett. **34**, 1204–1206 (2009).

20. T. Ehrenreich, R. Leveille, I. Majid, G. Rines, P. F. Moulton, Q-Peak, and Nufern, "1-kW All-Glass Tm:fiber Laser," in *SPIE Photonics West* (2010).

21. N. Simakov, A. Hemming, W. A. Clarkson, J. Haub, and A. Carter, "A cladding-pumped, tunable holmium doped fiber laser," Opt. Express **21**, 28415 (2013).

22. Y. Li, Y. Zhao, B. Ashton, S. D. Jackson, and S. Fleming, "Highly efficient and wavelength-tunable Holmium-doped silica fibre lasers," Opt. Commun. 2005. ECOC 2005. **3**, 679–680 (2005).

23. A. S. Kurkov, V. V. Dvoyrin, and A. V. Marakulin, "All-fiber 10 W holmium lasers pumped at λ=1.15 μm," Opt. Lett. **35**, 490 (2010).

24. A. Hemming, N. Simakov, A. Davidson, S. Bennetts, M. Hughes, N. Carmody, P. Davies, L. Corena, D. Stepanov, J. Haub, R. Swain, and A. Carter, "A monolithic cladding pumped holmium-doped fibre laser," Conf. Lasers Electro-Optics CW1M.1 (2013).

25. A. Hemming, S. Bennetts, N. Simakov, A. Davidson, J. Haub, and A. Carter, "Resonantly Pumped 2 μm Holmium Fibre Lasers," in *Specialty Optical Fibers* (OSA, 2011), p. SOMB1.

26. J. W. Kim, A. Boyland, J. Sahu, and W. Clarkson, "Ho-doped silica fibre laser in-band pumped by a Tm-doped fibre laser," in *European Conference on Lasers and Electro-Optics* (2009), Vol. 6084, p. 6873.

27. D. B. S. Soh, J. Nilsson, J. K. Sahu, C. Codemard, P. Dupriez, and V. Philippov, "Neodymium-doped cladding-pumped aluminosilicate fiber laser tunable in the 0.9um wavelength range," IEEE J. Quantum Electron. **40**, 1275–1282 (2004).

28. M. Laroche, B. Cadier, H. Gilles, S. Girard, L. Lablonde, and T. Robin, "20 W continuous-wave cladding-pumped Nd-doped fiber laser at 910 nm.," Opt. Lett. **38**, 3065–7 (2013).

29. I. P. Alcock, A. I. Ferguson, D. C. Hanna, and A. C. Tropper, "Tunable, continuous-wave neodymium-doped monomode-fiber laser operating at 0.900–0.945 and 1.070-1.135 μm," Opt. Lett. **11**, 709 (1986).

30. K. Ueda, H. Sekiguchi, and H. Kan, "1kW CW output from fiber-embedded disk lasers," in *Conference on Lasers and Electro-Optics* (Opt. Soc. America, 2002), pp. CPDC4–1–CPDC4–2.

31. E. M. Dianov, A. V. Shubin, M. a. Melkumov, O. I. Medvedkov, and I. a. Bufetov, "High-power cw bismuth-fiber lasers," J. Opt. Soc. Am. B **24**, 1749 (2007).

32. S. V. Firstov, I. A. Bufetov, V. F. Khopin, A. V. Shubin, A. M. Smirnov, L. D. Iskhakova, N. N. Vechkanov, A. N. Guryanov, and E. M. Dianov, "2 W bismuth doped fiber lasers in the wavelength range 1300-1500 nm and variation of Bi-doped fiber parameters with core composition," Laser Phys. Lett. **6**, 665–670 (2009).

33. V. Supradeepa and J. Nicholson, "Power scaling of high-efficiency 1.5 μm cascaded Raman fiber lasers," Opt. Lett. **38**, 2538–2541 (2013).

34. M. Meleshkevich, N. Platonov, D. Gapontsev, A. Drozhzhin, V. Sergeev, and V. Gapontsev, "415W Single-Mode CW Thulium Fiber Laser in all-fiber format," in *European Conference on Lasers and Electro-Optics* (2007).

35. D. Creeden, B. Johnson, S. Setzler, and E. Chicklis, "Resonantly-pumped Tm-doped fiber laser with> 90% slope efficiency," Opt. Lett. **preprint**, (2013).

36. S. D. Jackson and T. a. King, "Theoretical modeling of Tm-doped silica fiber lasers," J. Light. Technol. **17**, 948–956 (1999).

37. P. Peterka, B. Faure, W. Blanc, M. Karásek, and B. Dussardier, "Theoretical modelling of S-band thulium-doped silica fibre amplifiers," Opt. Quantum Electron. **36**, 201–212 (2004).

38. S. D. Jackson and S. Mossman, "Efficiency dependence on the Tm3+ and Al3+ concentrations for Tm3+-doped silica double-clad fiber lasers.," Appl. Opt. **42**, 2702–7 (2003).

39. P. F. Moulton, G. Rines, E. V. Slobodtchikov, K. F. Wall, G. Frith, B. Sampson, and A. Carter, "Tm-Doped Fiber Lasers: Fundamentals and Power Scaling," IEEE J. Quantum Electron. **15**, 85–92 (2009).

40. D. Gloge, "Weakly guiding fibers," Appl. Opt. **10**, 2252–8 (1971).

41. D. Marcuse, "Loss analysis of single-mode fiber splices," Bell Syst. Tech. J **56**, 703–718 (1977).

42. W. Koechner, *Solid-State Laser Engineering (Springer Series in Optical Sciences)* (Springer, 2006), p. 750.

43. E. Snitzer, H. Po, F. Hakimi, R. Tumminelli, and B. C. McCollum, "Double-clad, offset-core Nd fiber laser," in *Optical Fiber Sensors* (1988), Vol. 2, p. PD5.

44. C. Ranaud, H. L. Offerhaus, J. A. Alvarez-Chavez, C. J. Nilsson, W. A. Clarkson, P. W. Turner, D. J. Richardson, and A. B. Grudinin, "Characteristics of Q-switched cladding-pumped ytterbium-doped fiber lasers with different high-energy fiber designs," IEEE J. Quantum Electron. **37**, 199–206 (2001).

45. J. Nilsson, J. D. Minelly, R. Paschotta, A. C. Tropper, and D. C. Hanna, "Ring-doped cladding-pumped single-mode three-level fiber laser," Opt. Lett. **23**, 355 (1998).

46. J. Kerttula, V. Filippov, Y. Chamorovskii, V. Ustimchik, K. Golant, and O. G. Okhotnikov, "Tapered fiber amplifier with high gain and output power," Laser Phys. Lett. **22**, 1734–1738 (2012).

47. J. Hansryd, F. Dross, M. Westlund, P. A. Andrekson, and S. N. Knudsen, "Increase of the SBS threshold in a short highly nonlinear fiber by applying a temperature distribution," J. Light. Technol. **19**, 1691–1697 (2001).

48. M.-J. Li, X. Chen, J. Wang, S. Gray, A. Liu, J. a Demeritt, a B. Ruffin, A. M. Crowley, D. T. Walton, and L. a Zenteno, "Al/Ge co-doped large mode area fiber with high SBS threshold.," Opt. Express **15**, 8290–9 (2007).

49. R. Stolen, E. Ippen, and A. Tynes, "Raman oscillation in glass optical waveguide," Appl. Phys. Lett. **62**, 18–21 (1972).

50. R. Smith, "Optical power handling capacity of low loss optical fibers as determined by stimulated Raman and Brillouin scattering," Appl. Opt. **11**, 2489–2494 (1972).

51. J. Bromage, "Raman Amplification for Fiber Communications Systems," J. Light. Technol. **22**, 79–93 (2004).

52. A. V Smith and B. T. Do, "Bulk and surface laser damage of silica by picosecond and nanosecond pulses at 1064 nm.," Appl. Opt. **47**, 4812–32 (2008).

53. D. J. Richardson, J. Nilsson, and W. A. Clarkson, "High power fiber lasers: current status and future perspectives [Invited]," J. Opt. Soc. Am. B **27**, B63 (2010).

54. G. Fibich and a L. Gaeta, "Critical power for self-focusing in bulk media and in hollow waveguides.," Opt. Lett. **25**, 335–7 (2000).

55. R. L. Farrow, D. A. V. Kliner, G. R. Hadley, and A. V. Smith, "Peak-power limits on fiber amplifiers imposed by self-focusing.," Opt. Lett. **31**, 3423–5 (2006).

56. D. Marcuse, "Influence of curvature on the losses of doubly clad fibers.," Appl. Opt. **21**, 4208–13 (1982).

57. J. P. Koplow, D. A. V. Kliner, and L. Goldberg, "Single-mode operation of a coiled multimode fiber amplifier," Opt. Lett. **25**, 442 (2000).

58. M.-J. Li, X. Chen, A. Liu, S. Gray, J. Wang, D. T. Walton, and L. A. Zenteno, "Limit of Effective Area for Single-Mode Operation in Step-Index Large Mode Area Laser Fibers," J. Light. Technol. **27**, 3010–3016 (2009).

59. "NKT Photonics," http://www.nktphotonics.com.

60. F. Stutzki, F. Jansen, A. Liem, C. Jauregui, J. Limpert, and A. Tünnermann, "26 mJ, 130 W Q-switched fiber-laser system with near-diffraction-limited beam quality.," Opt. Lett. **37**, 1073–5 (2012).

61. T. Eidam, C. Wirth, C. Jauregui, F. Stutzki, F. Jansen, H.-J. Otto, O. Schmidt, T. Schreiber, J. Limpert, and A. Tünnermann, "Experimental observations of the threshold-like onset of mode instabilities in high power fiber amplifiers.," Opt. Express **19**, 13218–24 (2011).

62. M. E. Fermann, "Single-mode excitation of multimode fibers with ultrashort pulses," Opt. Lett. **23**, 52 (1998).

63. C.-H. Liu, G. Chang, N. Litchinitser, D. Guertin, N. Jacobsen, K. Tankala, and A. Galvanauskas, "Chirally Coupled Core Fibers at 1550-nm and 1064-nm for Effectively Single-Mode Core Size Scaling," Conf. Lasers Electro-Optics 1–2 (2007).

64. L. Dong, X. Peng, and J. Li, "Leakage channel optical fibers with large effective area," J. Opt. Soc. Am. **24**, 1689–1690 (2007).

Chapter 3.

Tunable thulium fibre lasers

3.1 Introduction

High brightness sources operating in the 1700-2100nm wavelength range can enable many potential applications. Medical applications, such as soft tissue surgery [1] and acne treatment [2], benefit from the increased absorption seen in this band. For materials processing long wavelength fibre sources allow enhanced processing of polymers, in comparison to shorter wavelength sources [3]. The 1700-2100nm wavelength range is a region of rich chemical absorption features and can be used for gas species identification and determination of atmospheric concentrations [4]. Within the defence community, there is a great interest in the 'eye-safe' wavelength region that thulium allows access to [5]. This is both for direct applications such as LIDAR [6], but also as a platform for further wavelength conversion into the mid-IR [7]. In the research environment, access to high brightness sources in this wavelength range serve as a tool for further laser and component development. As commercial applications of two micron sources become more established within industry, there is a growing need for high brightness, wavelength flexible sources for the characterisation of next generation optical systems. One such system is the thulium-doped fibre amplifier (TDFA) that is currently being explored in long wavelength communications [8]. To date, wavelength coverage of this band has tended to be restricted in availability and/or of a low spectral power density. Low-level commercial maturity is seen within this wavelength range in comparison to Yb or Er sources operating in the 10xx nm and 15xx nm bands. This situation is changing, with the laser community continuing to find advantage in the broad wavelength coverage and unique spectroscopy of thulium sources.

In this chapter we will look at the range of applications enabled by the broad wavelength operation of thulium sources. First introducing thulium spectroscopy, then analysing the

potential wavelength coverage and the issues associated with the varying quasi-three-level behaviour seen in this dopant. We will then review the current state of the art, both within literature and commercial options for (fibre) sources in this wavelength band. Finally, we will demonstrate several tunable source architectures, experimentally showing wavelength coverage from 1660nm through to 2115nm. Extending these results to higher power levels we also investigate the achievable efficiency of two fixed wavelength sources, operating at wavelengths of 1726nm and 1950nm with internal slope efficiencies of 69% and 72% respectively.

3.2 Background

3.2.1 Spectroscopic proprieties

Whilst the thulium florescence from the $^3F_4$ – $^3H_6$ transition can be seen from 1600-2200nm it is in practice extremely difficult to cover this entire emission band with a single fibre source. The combination of varying quasi-three-level behaviour as a function of wavelength (Figure 3.1) and gain saturation effects caused by amplified spontaneous emission, require trade-offs to be made when attempting to access either the long or short wavelength components of this band.

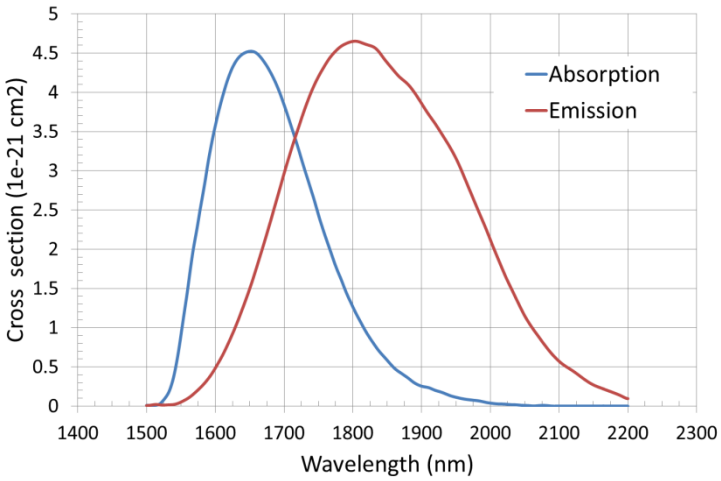

Figure 3.1 Absorption and emission cross-sections for Tm:silica, data from: [9,10].

At low excitation levels, signal reabsorption of shorter wavelengths pushes gain to longer wavelengths where more 4-level behaviour is seen. At higher excitation levels, gain is dominated by short wavelength ASE preventing longer wavelength operation. As a

result, to access the shorter wavelengths of the $^3F_4$ – $^3H_6$ transition, where signal reabsorption is prominent, high excitation density and short cavity lengths are required. This is achievable with low thulium doping concentrations and high brightness (core) pumping. Whilst to access the long wavelength components of the emission band longer device lengths and lower brightness (cladding) pumping is desired. To highlight this behaviour we first define the fractional inversion of the two laser transitions as:

$$F = \frac{N_2}{N_1 + N_2} \tag{18}$$

where N_1 and N_2 are the population densities for the lower ($^3H_6$) and upper ($^3F_4$) laser manifolds. With the resulting the net gain cross-section:

$$\sigma(\lambda_l) = F\sigma_e(\lambda_l) - (1 - F)\sigma_a(\lambda_l) \tag{19}$$

where $\sigma_a(\lambda_l)$ and $\sigma_e(\lambda_l)$ are the absorption and emission cross-sections at the operating wavelength λ_l.

The wavelength dependent net gain cross section of the $^3F_4$ – $^3H_6$ transition in Tm:silica is plotted in Figure 3.2 for a range of fractional inversion levels. Cladding pumped fibre lasers with low brightness pumping (generally by 79xnm diode sources) and high thulium concentrations (to maximise two-for-one efficiency) tend to operate with low excitation density, operating in the 1900-2100nm wavelength range. Whilst core pumped systems (generally pumped by high brightness 156xnm fibre sources), tend to have lower dopant concentrations and much higher excitation density leading to operation in the 1700-1950nm wavelength range.

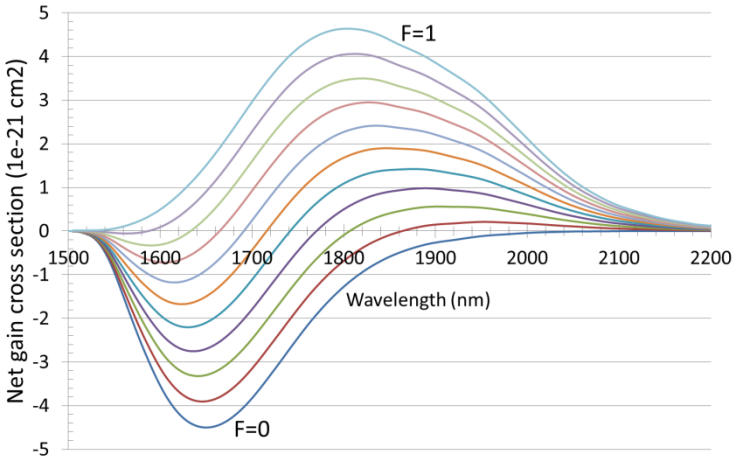

Figure 3.2 Calculated net gain cross sections of Tm:silica over a range of fractional inversion levels. Successive lines represent increasing fractional inversion levels in 0.1 increments from 0 (lower curve) to 1 (upper curve).

3.2.2 Applications

3.2.2.1 Chemical sensing and medical use

As we have seen above, the emission band of Tm:silica covers an extremely broad wavelength range of greater than 1700-2100nm. Because of this broad wavelength coverage it is an interesting source for spectroscopic characterisation and the targeting of various species and materials. In the gaseous state, CO_2, CH_4 and H_2O all show absorption features within this wavelength range (Figure 3.3). Using various techniques of absorption spectroscopy these species can be specifically targeted to allow concentrations to be determined over short or long distances [4,11–13].

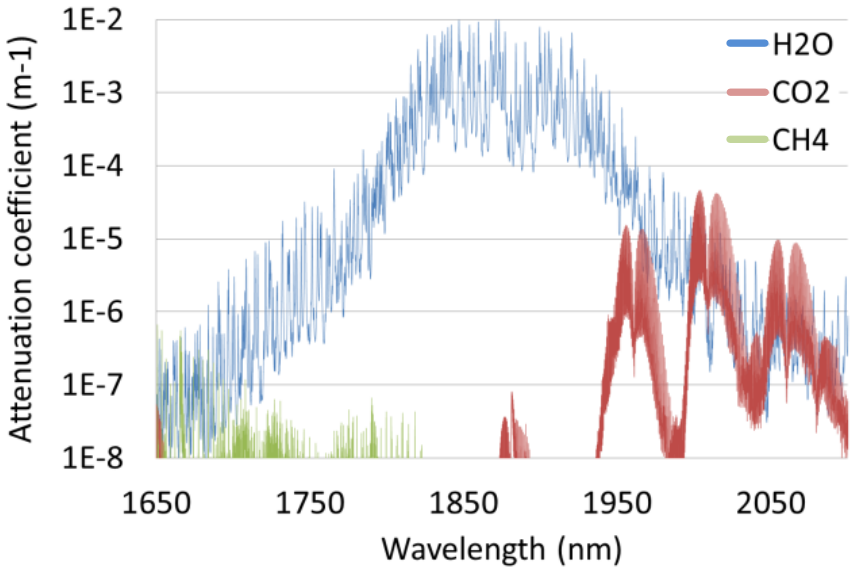

Figure 3.3 Atmospheric absorption bands of several gas species in concentrations typically found in the atmosphere, data from: [14].

Within this band liquid water shows a local maximum in absorption at ~1940nm (of α=120cm^{-1}, see Figure 3.4) but also reduces to a local minimum (α=4.5cm^{-1}) at 1700nm. This is of interest within the medical field, where soft tissue absorption closely matches that of liquid water and allows a tailoring of penetration depth from ~0.085-2.2mm across the thulium emission band. This range of penetration depths sits in between that of CO_2 sources (~10µm) and Yb sources (2-8cm) and can be advantageous for soft tissue cutting and promotion of coagulation [15]. Thulium sources are also commonly used in lithotripsy and other urology applications [16].

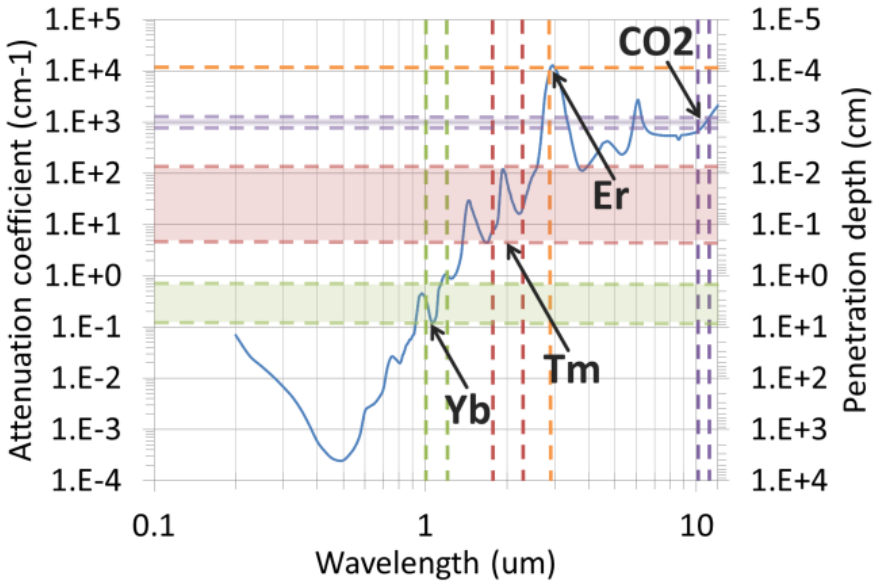

Figure 3.4 Liquid water absorption spectra with highlighted sections detailing the penetration depth across several laser operating windows, data from : [17].

3.2.2.2 172x nm C-H stretch bond absorption

At the shorter end of the thulium emission band strong absorption features relating to C-H bond stretch resonance (1st overtone) are seen in materials containing hydrocarbons [18]. These features are generally within the 172xnm wavelength range. Within this same wavelength range liquid water demonstrates a local minimum in absorption, this allows the preferential targeting of hydrocarbon rich materials.

Laser acne treatment

A promising medical application has been identified to take advantage of this fortuitous combination, at wavelengths of 1726nm fat/lipid rich tissues within the human body show local absorption maxima. At this same wavelength, soft tissue shows a local absorption minima (due to high water content). The result is a situation where lipid absorption is stronger than that of the surrounding soft tissue, this allows preferential absorption within lipid rich tissues, such as the sebaceous glands (see Figure 3.5). As described in [2] this effect can be employed in the treatment of skin conditions such as acne, allowing the preferential heating of these sebaceous glands whilst leaving the surrounding tissue relatively unharmed.

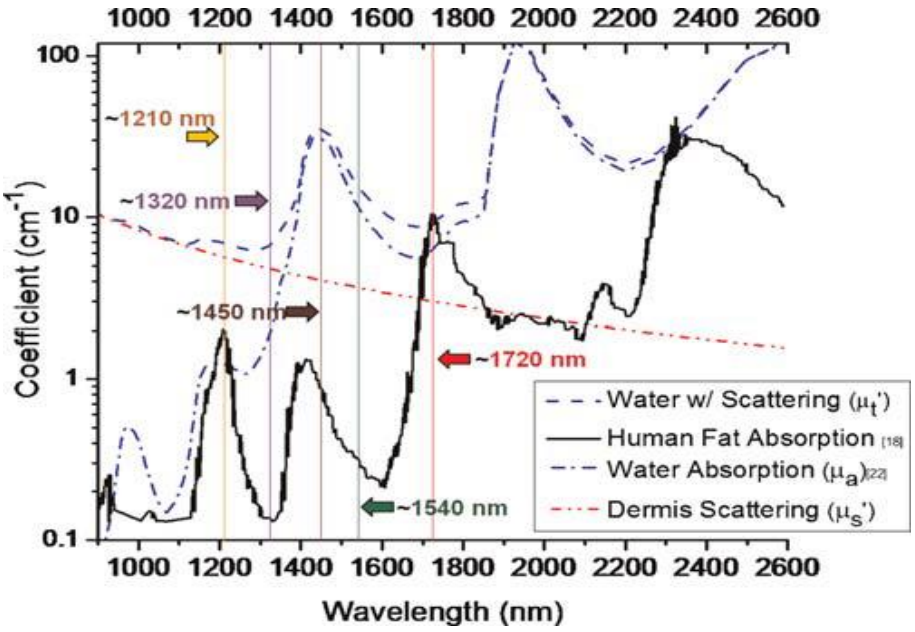

Figure 3.5 Comparison of absorption coefficients for water and fat tissue absorption within the 900-2600nm wavelength range. At a wavelength of 172xnm, water absorption shows local minima and within the same range, fat absorption shows local maxima, from [2].

3.2.2.3 Absorber free polymer materials processing

In addition to the promising medical applications of thulium sources within the 1700-2100nm wavelength range, organic polymers demonstrate strong absorption features due to O-H, O-C and C-H bond resonances. Figure 3.5 shows the absorption features of 1.6mm thick samples of several common plastics in the 500 to 2500nm wavelength range. Here we see prominent absorption features within the thulium emission band. At around 1720nm C-H overtones result in absorption features many times stronger than that of 10xx nm or 15xx nm absorption. At longer wavelengths absorption features due to O-H bonds are also seen. These prominent absorption features (particularly at shorter wavelengths) have the potential to allow laser welding and processing of plastics without the need for absorption enhancing additives [3] . It should also be possible to exploit the differing absorption features within this range to target specific plastics for preferential heating via wavelength selection and tuning.

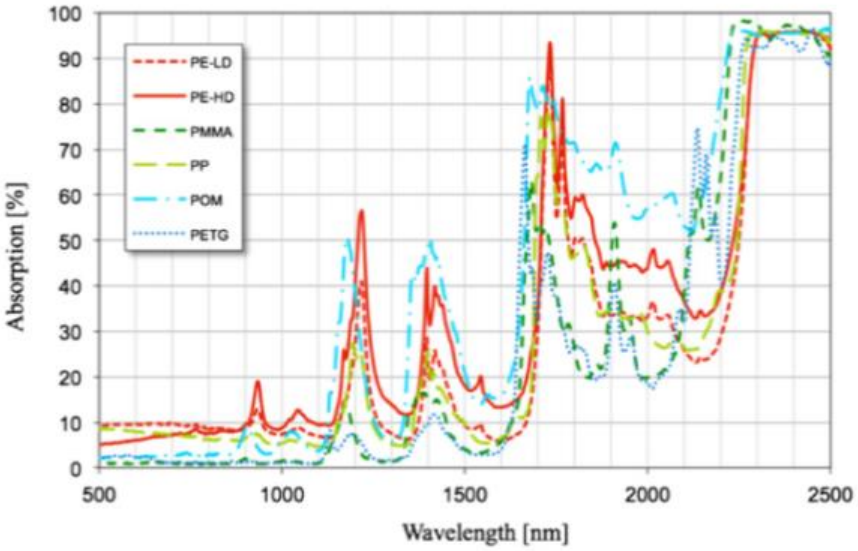

Figure 3.6 Absorption spectra for several common polymers types (sample thickness 1.6mm), from [3]

3.2.2.4 Thulium as a pump source

Thulium fibre sources have also proved useful for laser pumping of other dopants. Holmium shows useful absorption features within the thulium emission band from ~1900 - 2000nm for crystal and glass hosts [19,20]. Cr doped laser materials can also be pumped with thulium sources, allowing access to the 2-3µm wavelength range [21]. Proposals have been made for in-band pumping schemes where shorter wavelength operation thulium fibre lasers are used to pump longer wavelength thulium sources [22,23]. The advantage of such an arrangement is the low quantum defect between pump and signal (18xx-19xx>19xx-20xx nm) and may allow significant power scaling. More recently the very short wavelength operation of thulium (1686nm) has been highlighted as a potential pump source for Dy:fluoride to allow laser access to 3.7 and 4.7µm laser operation [24].

3.2.3 Tuning techniques for fibre lasers

As we have highlighted above, there is a large application space available for thulium sources that covers the entire $^3F_4$ – $^3H_6$ emission band. Because of this it can be advantageous to operate thulium sources in tunable configurations, this is both for the range of applications mentioned above and also as an invaluable piece of diagnostic equipment for component testing and system characterisation.

There are many options for wavelength selection and tuning within a fibre laser cavity, the high small signal gain and low thresholds result in a very forgiving architecture and allow for techniques that would not normally be appropriate in lower gain systems.

Most fibre laser tuning techniques require the movement away from an all fibre cavity, with the introduction of external cavity free-space components. However, much success has been had with 'fiberising' of these components, where a robust and compact package is designed to allow the propagating light within a fibre to exit into free space, through a desired component and then back into the fibre with a minimum of loss and without the need for any user alignment. Such a high level of sophistication has been achieved within these packages that they are commonly thought of as 'all-fibre' components. Although many components within the two-micron wavelength range have not reached this level of integration, the barriers are financial rather than physical.

Here we will review several different tuning techniques relevant to this thesis, and afterwards cite the relevant work utilising these techniques when applied to thulium sources.

3.2.3.1 Diffraction grating

Diffraction gratings are commonly used, and widely available, wavelength dispersive elements; most often found in wavelength diagnostics instruments such as monochromators. The principle of operation is based on the wavelength dependent diffraction from a periodic structure. Where the incident light is dispersed in angle, dependent on both the spatial frequency of the periodic structure and the wavelength of the incident light. As a wavelength selective element, they have found wide use in fibre laser sources; this is due to their wide wavelength coverage, commercial availability and simplicity in wavelength control. The characteristic diffraction equation for a periodic structure is given by:

$$m\lambda = d(sin\theta + sin\theta') \tag{20}$$

Where m is the diffracted order and θ & θ' are the incident and diffracted angles with reference to the grating normal and d is the spatial period of the structure. The grating can be operated in a retroreflective configuration where incident and diffracted angles (of orders above 0) are equal (Figure 3.7(a)). In this configuration, the so-called Littrow

configuration, wavelength tuning can be achieved by varying the angle of the diffraction grating.

$$m\lambda = 2d(sin\theta) \tag{21}$$

Through the use of an additional adjustment mirror it is possible to operate the grating in a 'Littman-Metcalf' configuration (Figure 3.7(b)) where the grating angle is fixed and adjustment of the feedback mirror is used for wavelength tuning. In this configuration, grating resolution is enhanced through a double-pass arrangement.

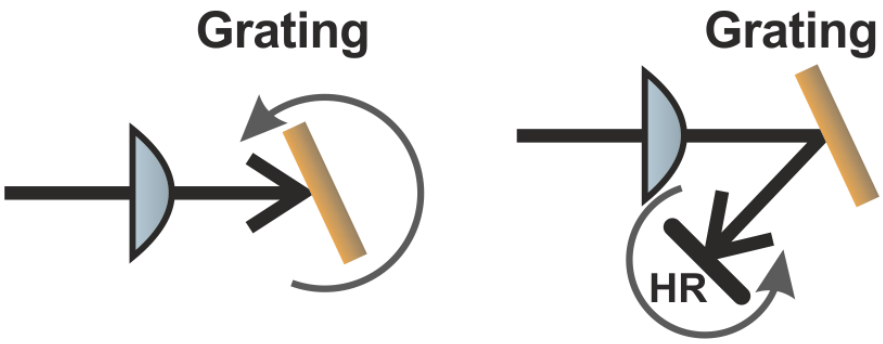

(a) (b)

Figure 3.7 Diffraction grating in (a) Littrow configuration and (b) Littman-Metcalf configuration.

Depending on the substrate reflectivity and the grating's periodic structure shape the diffraction efficiency of a reflective diffraction grating can be upwards of 90% in a Littrow configuration for a given polarization and design wavelength.

3.2.3.2 Volume Bragg grating (VBG)

Volume Bragg gratings, where a periodic refractive index modulation is written into the volume of a photo thermal refractive (PTR) glass, demonstrate high wavelength selectivity and high power handling capability. The glass for these devices shows a broad wavelength transparency (from 350nm to 2500nm) and high thermal stability [25], allowing broad wavelength coverage. Relying on Bragg diffraction these elements can be operated in either a transmissive or a reflective configuration. Due to a relatively large refractive index modulation and long interaction length, a typical VBG can be very efficient, with reflectivities of >95% commonly achieved with sub-nm bandwidths. This

allows compact narrowband wavelength selection without the need for beam expanding optics. The relationship between operating wavelength and grating period is given by:

$$\lambda_{VBG} = 2\Lambda \cos\theta \tag{22}$$

Where, Λ is the period of the index modulation and θ is the angle of incidence relative to the grating normal. Through the use of angle tuning a VBG can be configured as a wavelength selective external cavity element. Here the reflected beam of the VBG (when operated away from normal) is back reflected via secondary mirror (Figure 3.8) and allows a down tuning of the resonance wavelength and a doubling of the VBG wavelength selectivity.

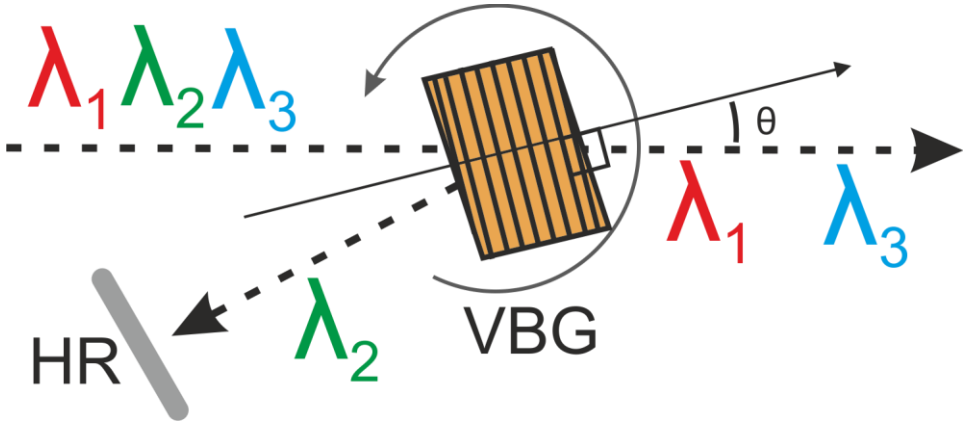

Figure 3.8 Schematic of a reflection type volume Bragg grating in angle-tuned retro-reflective configuration.

3.2.3.3 Strain tuned fibre Bragg gratings

Fibre Bragg gratings, where a periodic index modulation is now written directly into the core of a fibre waveguide, are true all-fibre components that do not require any free space elements. Due to the strong overlap between the index modulation and the guided mode, as well as long interaction lengths, wavelength reflectivity and selectivity can be very high; with 99.9% reflectivities regularly achieved and spectral bandwidths in the tens of picometres. The first order resonance wavelength for a fibre Bragg grating is given by:

$$\lambda_{FBG} = 2n_{eff}\Lambda \tag{23}$$

Where n_{eff} is the effective index of the propagating mode. During the fabrication process, some increase in optical fibre absorption is seen, but in well-designed packages FBG's can allow power scaling from the 100's of Watt to the kW level. By changing the effective Bragg period ($n_{eff}\Lambda$) it is possible to achieve a degree of wavelength flexibility. Often this is accomplished by temperature control or by either straining or compressing the length of the grating. Strain tuning, where the grating is placed under sufficient tension to physically increase the separation of the Bragg period, can be used to shift the operating wavelength to longer values. However, due to the tension experienced by the optical fibre this method is prone to microcrack formation and can suffer low reliability. Wavelength shifts of the order of 3% (of λ_0) are achievable [26].

Another technique involves the longitudinal compression of the optical fibre containing the FBG, here the physical separation of the Bragg period is decreased and thus shorter wavelength operation is achieved. Due to the use of compressive forces rather than tension, microcrack formation is hindered and results in a higher reliability device with a wider tuning range. Using this technique over 100nm of wavelength down-tuning has been demonstrated at an operating wavelength of 1600nm [27], corresponding to a physical compression of the glass of over 8%. Due to the mounting arrangement required for reliable compression tuning, effective heat sinking of the FBG is difficult and to date operation at higher power levels is unproven.

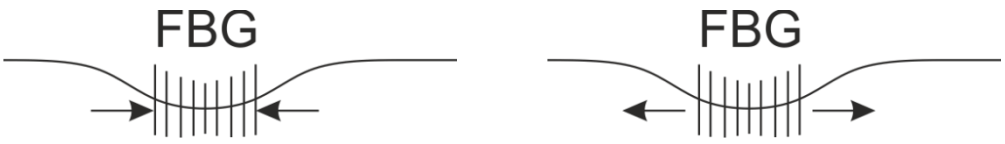

Figure 3.9 Fibre Bragg gratings in (a) compression and (b) tension tuned configurations.

3.2.3.4 Acousto-optic tunable filter (AOTF)

An acousto-optic tunable-filter, based on the acousto-optic effect, is an electronically controllable band pass filter that provides high power handling and rapid wavelength selection without the need for moving parts. Through the use of an acoustic transducer driven by an RF input signal, an acoustic wave is formed within a crystal. The propagation of this acoustic wave leads to an index modulation within the crystal. When

driven by an appropriate RF frequency, a diffraction grating forms within the medium and is used to deflect a narrow band of wavelengths into a fixed angle (Figure 3.10).

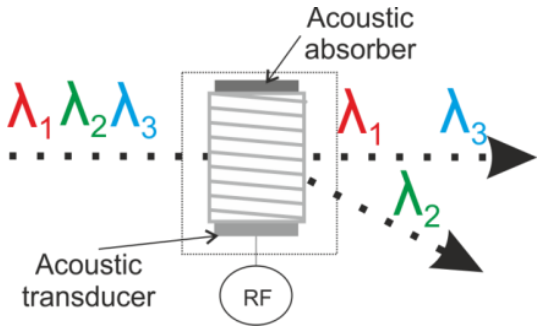

Figure 3.10 Schematic of an AOTF, defecting λ_2 into the 1st order whilst transmitting λ_1 & λ_3 in to the 0th order.

A unique property of the AOTF is the angle of deflection of the diffracted beam is fixed and independent of resonance wavelength. This allows the 1st order diffracted beam to be backreflected using a static mirror, with wavelength selection achieved by simply changing the RF drive frequency.

As there are no mechanically moving parts within the AOTF the selection and switching of wavelength can be much faster than would be possible in a mechanical system, limited only by the acoustic wave build-up time. Based on the same crystal technology used in high power Q-switchers, AOTFs are capable of high power handling and high diffraction efficiency, and due to the large transparency windows of the AO crystals used wavelength coverage can be extremely broad, often covering over an octave of wavelength spread. Spectral selectivity of high performance AOTFs can be of the order of a few nm for near-IR light and can be enhanced by double passing the device.

3.2.4 Review of two microns source wavelength coverage

Within this section we will look at tunable and fixed wavelength sources within the 1700-2100nm wavelength range, paying particular attention to thulium fibre sources.

The commercial availability of sources within the 1700-2100nm wavelength range has, to date, been limited, although this is changing. Within the past few years, due to the increasing availability of components, a number of companies have introduced products in this area [28–34]. Notable products include supercontinuum sources, where broad wavelength coverage can be extended through the thulium emission band through to

beyond 2400nm [35–37]. For higher output power options also exist for single wavelength or tunable sources. IPG photonics is perhaps the most developed in this wavelength range, with tunable Thulium source operating across 1900nm-2100nm at power levels of up to 50W and fixed wavelength options at powers of up to 200W. Nufern, originally only supplying thulium doped fibre, now offer a fixed wavelength 1940nm source with power levels up to 40W and Advalue photonics offer a range of pulsed and CW sources with power levels up to 10W. Fibre coupled multimode bulk laser sources are also available within this wavelength range and have been primarily intended for medical applications at power levels of up to 200W [38,39]. The cost of entry for this wavelength range is dominated by expensive diagnostic equipment and componentry, but is continuing to fall as the market expands.

Within published literature, a significant amount of work has been demonstrated for both power scaling and broad wavelength coverage. The current power records for single frequency and broader linewidth thulium operation sit at 608W [40], demonstrated in 2009, and ~1.1kW [41], demonstrated in 2010, both at a wavelength of ~2040nm. These results were achieved under cladding pumped operation with 79xnm diode pumps and operated with slope efficiencies of >50%. For higher brightness pumping with 1567nm Er fibre sources, Meleshkevich et.al have demonstrated 415W of output power at a 1940nm wavelength with slope efficiency of ~60% [42].

For wavelength tunable operation, wide wavelength coverage has been achieved in thulium fibre sources using external cavity configurations. Using a diffraction grating in Littrow configuration, Clarkson et al. demonstrated a 230nm wide tuning range from 1860-2090nm with up to 7W of output power in a cladding pumped thulium source with maximum slope efficiency of ~25%. [43]. Shorter wavelength operation was then demonstrated in [44] with the use of a core pumping configuration. Laser tunability of this source was over ~250nm ranging from 1726nm-1973nm. High brightness pumping was provided by a 1565nm pump source, resulting in ~46% slope at the gain peak as well as much shorter wavelength operation. Highlighting the effect of laser threshold on operating wavelength within the three level system, Tang et al. [45] demonstrated a ~100nm tuning range using broadband reflectors and changing only the cavity feedback level. For low feedback levels (4%) laser operation was at 1949nm and by increasing cavity feedback (to 95%), the operating wavelength was pushed to 2055nm. This effect was also demonstrated in [46], where a maximum of long wavelength emission at

2138nm[3] was achieved with a combination of a diffraction grating and a high level of optical feedback (R=35%). The approach of external grating wavelength tuning has been extended in [47] to a master-oscillator power-amplifier (MOPA) configuration. Where in a cladding pumped amplifier configuration >200W was demonstrated from 1927-2097nm.

The above demonstrations all rely on free space external cavities for wavelength selection. 'All fibre' solutions have been demonstrated in [48] and [49], with an electronically controlled Fabry Perot tunable filter and a mechanically tuned fibre-coupled grating. Both of these demonstrations were limited to sub 100mW output powers, but show broad wavelength coverage from 1840-2040nm and 1810-2080nm from the two respective sources.

Demonstrations of fixed single wavelength operation within the thulium gain band have also shown wide wavelength coverage, generally through the use of fibre Bragg gratings [40,50–58]. To date demonstrations of short wavelength thulium fibre operation have been limited. In [44] 2W was shown at a wavelength of 1723nm for 20W of launched pump power (1565nm) in a slightly multimode configuration. Other than this result only very low power sources have been demonstrated, with 1740nm operation shown in [51] (power level not quoted but < 50mW). 1mW of output power was demonstrated for single frequency operation at 1735nm [53] and 1684nm reported in [52]. The output power for the laser was not reported, but estimated to be of the order of 1mW.

From bulk thulium sources wavelength coverage and tunability can be dependent on host material and dopant concentration, within a YAG host thulium has demonstrated wavelength coverage from 1870nm-2180nm within several different configurations [59–63]. Other notable fixed wavelengths demonstrations include 115W & 120W generated from diode pumped Tm:YAG at wavelengths of 2010nm [64] & 2020nm [65] respectively. Additionally the shorter wavelength range of the thulium emission band can be accessed by Er:bulk in a range of different hosts with discrete wavelength operation at wavelengths within the 1640nm-1730nm range [66–70]

[3] There is some confusion as to the actual maximum operating wavelength within this paper. With the conclusion listing 2188nm as the maximum operating wavelength, however this value is not demonstrated within the results section of the text.

Using nonlinear frequency conversion, Er:fibre pumped Raman sources have also been demonstrated within the short wavelength end of the thulium gain band. Vinay et al. reported 4W of single mode output power at an operating wavelength of 1708nm in a Raman laser configuration. This was pumped by 11W of 1542nm [2]. Codemard et al. reported 10.2W at 1660nm, pumped with 21.4W at 1552nm [71].

3.3 Wavelength-agile thulium fibre laser

3.3.1 Introduction

Here we present a thulium fibre laser arrangement with external cavity comprising of an electronically addressable acousto-optic tunable filter (AOTF) and a broadband reflector for wavelength control. This simple arrangement allows a broad wavelength coverage and high power handling capability. As the AOTF is an electronically-controlled wavelength selective element no moving parts are needed within the laser cavity, allowing the fast and precise selection of operating wavelength. Moreover, this design allows for the possibility of selection and switching between multiple simultaneous wavelengths at speeds that far exceed those possible in mechanically-tuned systems. The use of an AOTF also allows wavelength selection and sweeping in non-traditional ways. Mechanically tuned systems must access operating wavelengths in a linear way, with the sequential selection of increasing or decreasing wavelength. Because of the lack of moving parts, the AOTF can select operating wavelength in non-sequential formats with non-linear sweep profiles. As input drive frequency defines operating wavelength, sophisticated computer control is possible and should allow the more targeted use of available light.

As mentioned within the background section, to cover the entire wavelength range of the thulium gain band multiple sources must be used. These target either longer wavelengths with long device lengths and low excitation densities or shorter wavelength through high excitation density and short active fibre lengths. Within this section, we first demonstrate a cladding pumped source, exploring the unique features of the AOFT within the longer wavelength region of the thulium gain band. This same approach is then applied to short wavelength operation with core-pumped low concentration thulium doped fibre (TDF).

The AOTF used within this work was supplied by Gooch and Housego and had an electronically addressable wavelength coverage from 1200-2200nm with an acoustic wave build-up time (and optical rise time) of ~ 20μs (for 10% to 90% transmission). Its behaviour was polarisation dependent with a 0-70% diffraction efficiency for a linearly polarised input. The single-pass spectral selectivity of the AOTF was wavelength dependent and showed a 2nm (FWHM) pass band when operated at 2000nm. Control of the resonance wavelength of the AOTF was achieved with a dual channel arbitrary waveform generator providing the appropriate RF drive signal (between 29-31MHz @ 200mW for the 1700-2100nm wavelength range).

3.3.2 Cladding pumped AOTF source

3.3.2.1 Experiential arrangement

The experimental layout is shown in Figure 3.11. A 4-meter length of polarisation-maintaining thulium-doped active fibre with a 10μm core diameter and 130μm cladding diameter was used as the laser gain medium. The fibre had a ~2.2 wt.% thulium concentration and a core numerical aperture (NA) of 0.15. The active fibre was cladding-pumped by a fibre-coupled multimode 795nm diode source, which was coupled into the inner-cladding of the active fibre using the free-space in-coupling arrangement shown in Figure 3.11. Feedback for lasing was provided by the ~4% Fresnel reflection from a perpendicularly-cleaved fibre facet at the pump in-coupling end of the fibre. At the opposite end, an external cavity containing AOTF and HR mirror provided feedback for the diffracted beam. The fibre facet adjacent to the external cavity was angle-cleaved at 14° to suppress broadband feedback and hence unwanted parasitic lasing between the fibre ends. The stress rod orientation in the polarisation maintaining active fibre was carefully adjusted, prior to angle cleaving, so that the fast (or slow) axis was parallel to the plane of incidence of the angle cleave. This simplified fibre rotation alignment, removing the need for a waveplate to align polarisation within the external cavity. Due to the strong birefringence seen in the AO crystal used within the AOTF (TeO_2), the AOTF served as a linear walk-off polariser within the external cavity and ensured single polarisation operation across the lasing band.

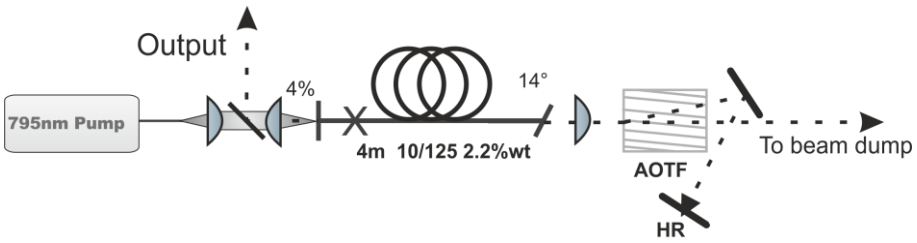

Figure 3.11. Experimental arrangement for the cladding pumped AOTF tunable thulium fibre laser.

Diagnostics arrangement

A typical diagnostics arrangement for recording laser output power spectra etc. is shown in Figure 3.12, this consists of an uncoated optical wedge used as a beam sampler with the bulk of the laser output directed towards a thermal power meter. The use of uncoated wedge allows access to a ~4% pick-off from the main output and demonstrates only very week wavelength dependence. These 4% beam samples can then be directed towards optical spectrum analysers (OSA) and oscilloscope (CRO) enabling the spectral and temporal behaviour of the laser to be measured. Beam sampling wedges can also be cascaded to allow further attenuation (0.16%, 0.064% etc.) of the output beam and can come in use when performing beam quality measurements with higher sensitivity photodetectors.

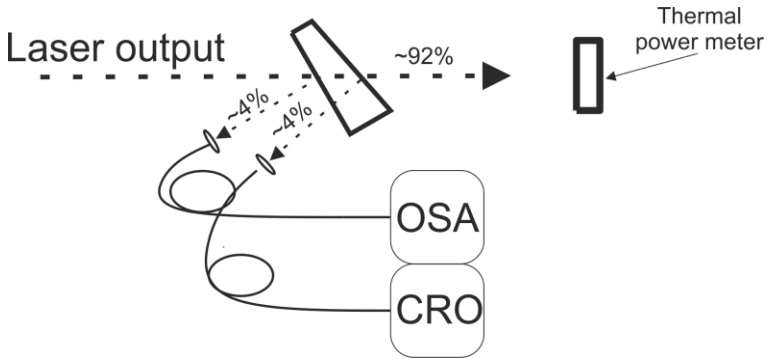

Figure 3.12. A typical laser diagnostics arrangement, demonstrating average power measurement as well as spectral and instantaneous temporal measurements.

3.3.2.2 Results

The laser yielded a maximum output power of 5W at 1975nm for 18W of launched pump. The spectral width of the output was 0.09nm FWHM and the polarisation extinction ratio

(PER) was 14.5dB. By changing the RF driver frequency to the AOTF the laser could be tuned from 1917nm to 2115nm with > 4W output power across 1930-2080nm (see Figure 3.13). Further increasing pump power beyond 18W lead to a reduction in the laser tuning range. This was due the onset of parasitic lasing at the fibre gain peak (1980-2000nm) when attempting to access the extremities of the tuning range. Threshold pump power was measured as a function of lasing wavelength by noting the pump power required for the onset of relaxation oscillations. The latter were monitored with the aid of a fast photodiode. The results (shown in Figure 3.13(a)) indicate that the minimum threshold pump power was 1.5 W at 2000 nm and that this increases to ~2.6W at the extremes of the wavelength tuning range. The increase in threshold at the short wavelength end of the tuning curve is attributed to increases in the three-level character and, at the long wavelength end, to a decrease in the emission cross-section.

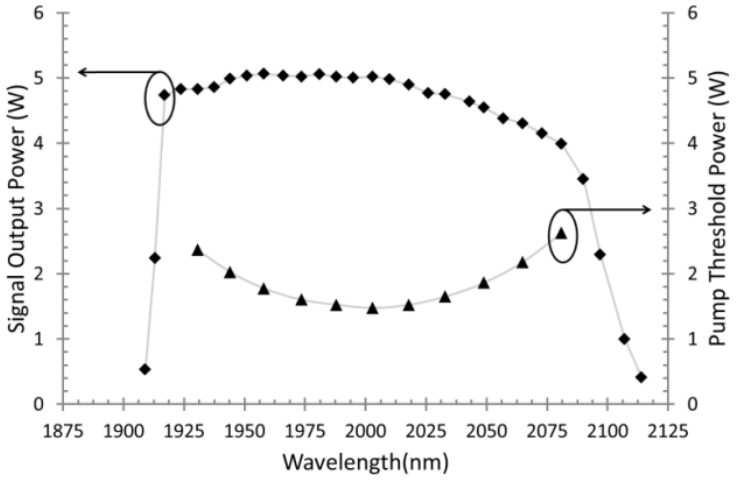

Figure 3.13 Laser output power (left axis) and threshold pump power (right axis) versus lasing wavelength

Under fixed wavelength operation the output of the fibre laser was continuous-wave (Figure 3.14), with no evidence of self-pulsing regardless of the operating wavelength. An advantageous feature of the simple linear cavity arrangement used in our experiments is that the inversion clamped at a safe level when the AOTF was switched off. When no feedback from the external cavity is present, parasitic lasing is able to reach threshold and occurs between the fibre end facets of the cavity. The large difference between the effective feedback reflectivities for the perpendicular facet and angled facet, cause most of the power generated by parasitic lasing to exit the cavity via the AOTF zero-order. The ratio of output powers between two laser output couplers can be described by

$\frac{P_1}{P_2} = \frac{1-R_1}{1-R_2}\sqrt{\frac{R_2}{R_1}}$ for a laser in the saturated regime [72]. We estimate the feedback reflectivity (R2) of the angle cleave to be ~ 10^{-5} %. This coupled with the relatively high 4% feedback from Fresnel reflection lead to the majority (>95%) of laser output under parasitic operation to be directed towards the angle cleave and eventually dumped by the AOTF. This inversion clamping behaviour reduces the likelihood of catastrophic damage due to self-pulsing events and allows the AOTF to be operated at a low duty cycle without detrimental consequences. We investigated this behaviour by driving the AOTF with a 50% duty cycle and 100Hz switching frequency. Figure 3.14(b) shows the time profile of the laser output. As can be seen during the 'off' period, minimal light is directed towards the laser output and in the 'on' period the laser quickly settles down to CW behaviour. Figure 3.14(c) shows a close-up of the laser turn on dynamics. Following an initial period of relaxation oscillation (~20 µs) the laser output quickly settles down to CW behaviour.

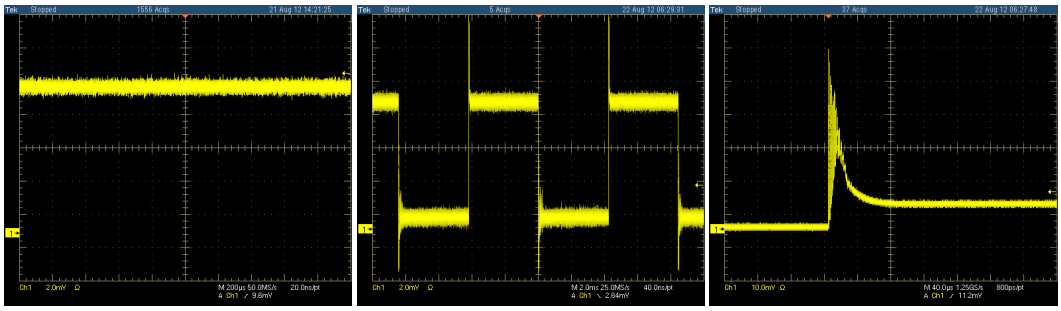

(a) (b) (c)

Figure 3.14 Oscilloscope traces of laser output under, (a) CW operation (200µs/dev). (b) Laser switching behaviour for 100Hz on-off modulation (2ms/dev). (c) Close-up of laser turn on dynamics showing initial relaxation oscillation of ~20µs (40µs/dev).

By driving the AOTF with multiple RF signals it is possible, in principle, to provide resonance for more than one wavelength within the external cavity. To investigate this behaviour, we used the dual channel output of the function generator to simultaneously drive the AOTF with two different RF frequencies and thus provide resonance at two wavelengths simultaneously. Under this mode of operation we could indeed demonstrate lasing at two independent wavelengths. Figure 3.15 shows the laser operating at 1960nm and 2010nm simultaneously with approximately equal output powers. The relative powers in the two lasing lines are adjusted by simply changing the RF drive power of each channel. In this way it was possible to produce an arbitrary ratio of powers between

the two wavelengths, compensating for the wavelength dependent gain in the fibre gain medium.

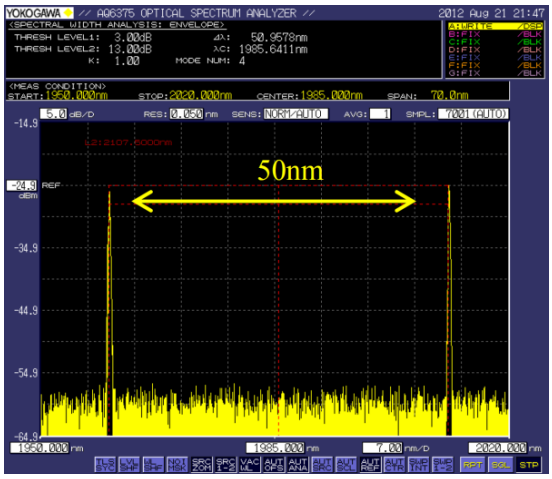

Figure 3.15 Laser output spectrum showing dual lasing operation with λ_1=1960nm & λ_2=2010nm.

As the separation of the two lasing wavelengths is decreased, beating between the RF signals used to drive the AOTF lead to complicated laser behaviour. Figure 3.16 shows the effect of decreasing wavelength separation (and hence RF drive frequency separation) on the temporal behaviour of the laser output. For wavelength separations above ~40nm we see simple CW behaviour. However, as separation is decreased below 40 nm a periodic modulation of the output power was observed with the modulation depth increasing and modulation frequency decreasing with decreasing wavelength separation. For a wavelength separation of 30nm a modulation frequency of ~500kHz is seen. Whilst for 10nm separation this decreased to < 200kHz. This behaviour arises due to the beat frequency of the RF signals falling within the AOTF response time as the RF frequency spacing decreases. As the wavelength separation of excited wavelengths decreases, the beat frequency between the RF signals also decreases, and eventually falls within the frequency response of the AOTF. This leads to a modulation in diffraction efficiency of the AOTF and eventually manifests as a modulation of the laser output via cavity 'Q' switching. This behaviour could be avoided by using multiple AOTFs, allowing simultaneous lasing on lines with greater flexibility in the wavelength separation.

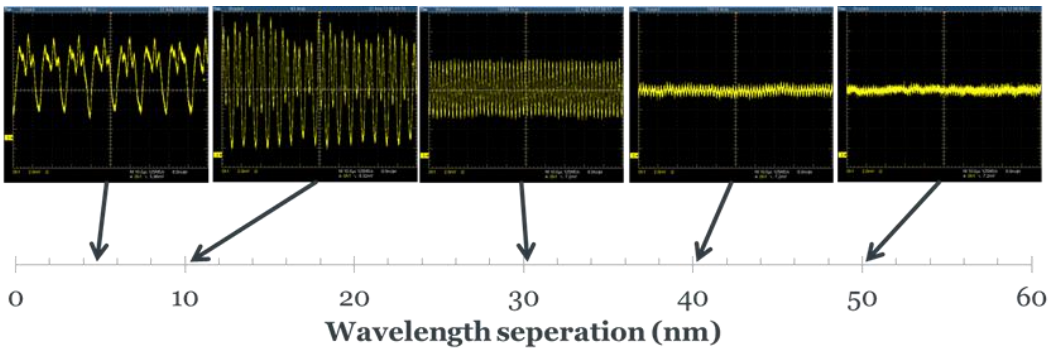

Figure 3.16 Right-to-left, oscilloscope traces of laser behaviour in the time domain for dual wavelength operation and decreasing wavelength separation (10µs/div). CW operation is seen for wavelength separations above 40nm.

3.3.3 Core pumped AOTF source

3.3.3.1 Experiential arrangement

In order to access the shorter wavelength side of the thulium gain band a core pumped system was constructed, this contained the same external cavity arrangement as used in the cladding-pumped system; however the 2wt% active fibre was replaced with a 0.2wt% thulium concentration fibre. The fibre had core and cladding dimensions of 6/125µm (diameter) and a core NA of 0.20. The active fibre device length of 1-meter provided approximately 18dB pump absorption. This fibre was end pumped with a single mode 1565nm source with up to 7W of output power. Pump in-coupling and signal out-coupling was achieved with a free space arrangement configured with a relay imaging arrangement. A dichroic mirror was used for separation of signal and pump. A passive fibre lead-in (SMF28) was spliced to the active fibre and was used to reduce thermal load at the pump in-coupling point.

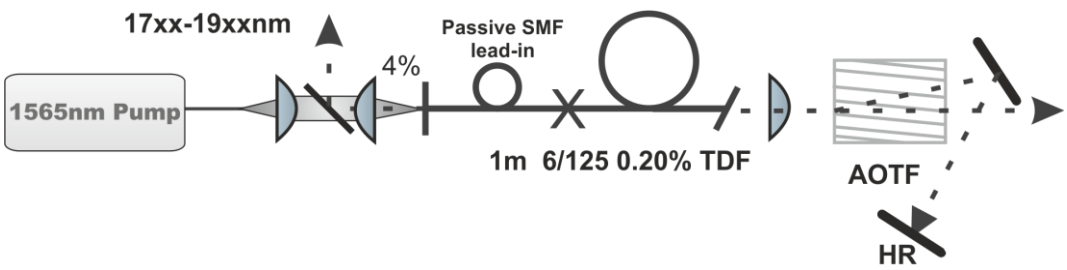

Figure 3.17 Core pumped short wavelength AOTF tunable thulium source.

3.3.3.2 Results:

At a launched pump level of 6.8W wavelength tunability from 1700-1970nm was achieved, with greater than 1W of output power seen when tuning from 1720-1950nm. At the power maxima of 1800nm the fibre showed a slope efficiency of 30%.

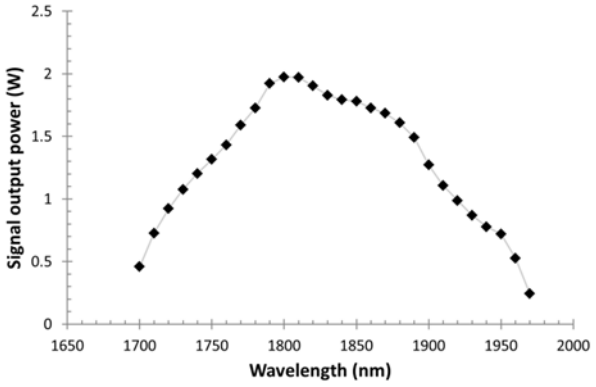

Figure 3.18 Core pumped thulium laser tunability for 6.8W of launched pump power

Here we can see the combination of high brightness core pumping and lower thulium concentration has resulted in much shorter wavelength operation of the tunable source. This is due to the higher excitation density and the shorter device lengths needed resulting in reduced signal reabsorption at the shorter wavelength portion of the thulium emission band.

3.3.4 Wavelength combination

Within this section we have demonstrated wavelength coverage from 1700 to 2115nm from two independent fibre gain stages, with 1700-1970nm tunability achieved with high brightness pumping and short cavity lengths and 1915-2115nm achieved with lower brightness cladding pumping. For many applications it is desirable to access this entire wavelength range within a single output. With this in mind, several steps have been taken to allow the spectral beam combination of the two fibre sources.

As a future extension to this work, a proposed layout allowing combination of these sources is shown in Figure 3.19. Here we spectrally combine the output of the two gain stages using dichroic mirrors. This arrangement has the advantage of needing only one external cavity tuning element, and should allow the seamless transfer from one laser gain

stage to the other. This arrangement will enable watt level output powers to be achieved across a 400nm wavelength range, controlled by a single AOTF drive signal.

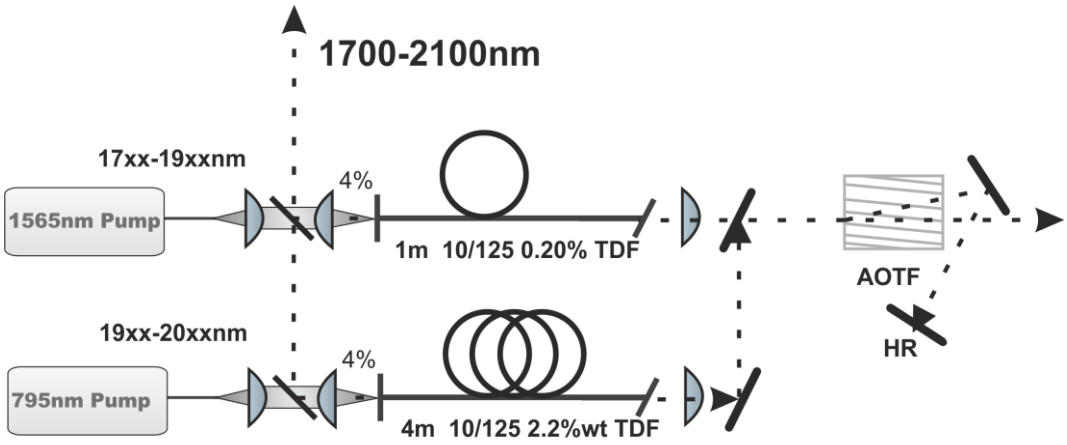

Figure 3.19 Diagrammatic layout of the purposed dual gain stage spectrally combined fibre source.

Due to time constraints the above configuration is yet to be realised experimentally, however a custom run of bandpass filters has been commissioned (Figure 3.20) and successfully tested within the group. With the combination of two external cavity wavelength swept sources (one cladding pumped and one core pumped) more information on this source can be found in [73].

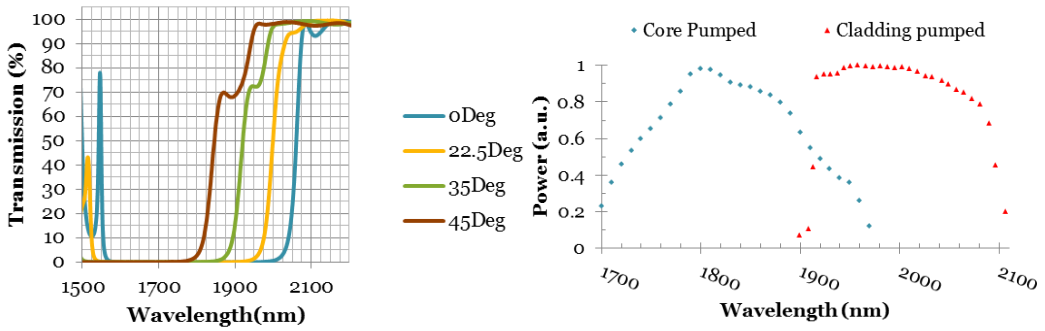

(a) (b)

Figure 3.20 (a) Spectral transmission properties of the commissioned band pass filters, the precise cut-on band of the filters can be fine-tuned via angle control. (b) Normalised tuning bands of the two gain stages demonstrating the possibility for over 400nm wavelength coverage

3.4 Compression tuned FBG for ultrashort wavelength thulium operation

Within this section we look at the extreme lower wavelength limits of the thulium $^3F_4$ – $^3H_6$ transition. Here a core pumped configuration was constructed with a compression tuned FBG for wavelength selection (Figure 3.21). By replacing the external cavity tuning arrangement with an all-fibre solution, higher efficiency wavelength-dependent feedback is achieved. This is due to the high reflectivity of the FBG arrangement as well as much lower coupling losses associated with the fibre fusion splices. The estimated feedback efficiency of this arrangement is ~90%, this is in comparison to the externally-tuned cavity operating at an estimated 40% efficiency. The high efficiency of this compression-tuned arrangement comes at a cost of limited wavelength tunability and potently limited power handling (due to the compression mounting arrangement). Within the following experiment, a Bragg grating with central wavelength of 1726nm is tuned down to 1660nm without damage, providing sufficient wavelength coverage to be limited by the gain of dopant rather than the tuning element.

3.4.1 Experimental arrangement

We constructed an all-fibre cavity for these short wavelength experiments, containing a compression-tuned fibre Bragg grating (constructed by M. Ibsen) to provide wavelength selective HR feedback and terminated at the opposite end with flat cleave for laser output coupling. The central wavelength of the FBG in its uncompressed state was 1726nm with a specified reflectivity of >99.9%. The active fibre had a thulium concentration of 0.2wt%. and core and cladding diameters of 10/100μm respectively. The core NA was 0.13 and thus operated in a single mode for both the pump and signal wavelength. This active fibre was core pumped with a commercially available 1565nm source. Pump coupling provided by a custom ordered filter type WDM (AFR), containing a dichroic mirror rather than a fused fibre coupler as would normally be used. The use of a dichroic filter within the WDM allowed broadband operation and a sharp transition between pump and signal wavelength. The WDM operated to combine 1565nm pump light with signal light operating at 1650-2100nm. Due to the limited specified power handling of the WDM, a maximum of 4.5W of pump light was incident. At this pump power. 4.05W was coupled into the active fibre. At the laser output residual pump light unabsorbed by the

active fibre was separated from the signal light using a dichroic mirror of 95% reflectivity (at pump wavelength). All signal power measurements were corrected for residual pump levels. The experimental layout of this cavity is shown in Figure 3.21.

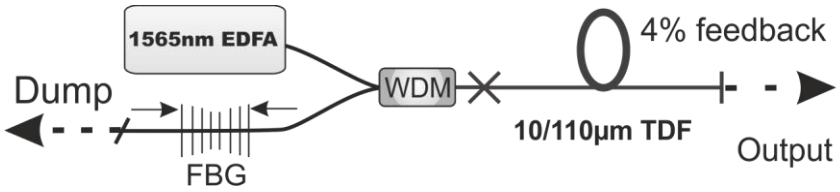

Figure 3.21 Experimental layout for compression tuned short wavelength thulium fibre laser.

3.4.2 Results

After an initial fibre cutback a 0.6m length of active fibre was chosen for these experiments. This allowed maximum wavelength tuning without the onset of parasitic lasing when operating at the wavelength extremes. The fibre Bragg grating was compression tuned from an initial wavelength of 1720nm down to 1660nm in 5nm increments. Over this wavelength range the maximum laser output power and pump power at laser threshold were recorded (Figure 3.22). At a maximum launched pump power of 4.05W the laser produced 1.5W of signal output at a wavelength of 1720nm. At this wavelength unabsorbed pump power was 0.53W. When tuning to shorter wavelengths laser threshold continually increased to a maximum value of 3.6W of launched pump power (2.4W absorbed). This was at a remarkably short lasing wavelength of 1660nm. Due to the relatively high threshold and limited power handling of the WDM, output power at this wavelength was limited to 65mW.

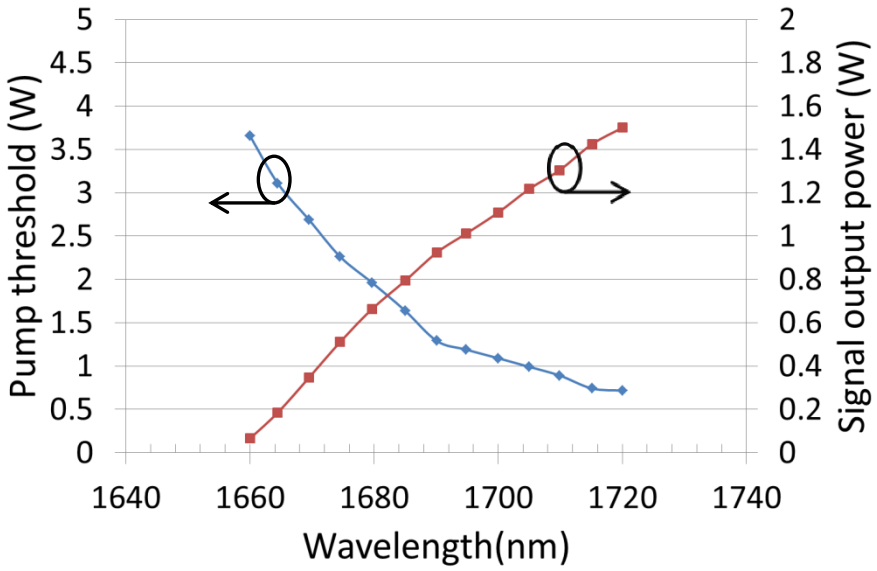

Figure 3.22 Pump threshold (left axis) and maximum out power (right axis) over a range of operating wavelengths.

The laser slope efficiency was measured at 20nm increments from the uncompressed FBG wavelength of 1720nm downwards, the results of which are shown in Figure 3.23. The laser demonstrated slope efficiencies of 47% (56%), 40% (51%) and 26% (36%) with respect to launched (absorbed) pump power, at wavelengths of 1720nm, 1700nm and 1679nm respectively. At these wavelengths, when operating with maximum pump power, pump absorption was 87%, 79% and 70% of total launched power.

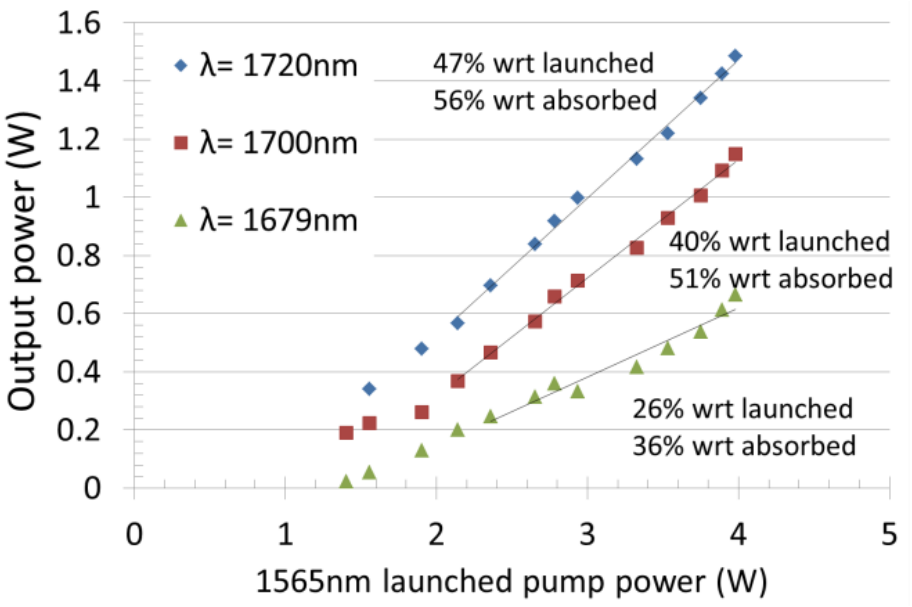

Figure 3.23 Laser slope efficiency for 1720nm (blue diamond), 1700nm (red squares) and 1679nm (green triangles)

The laser output spectrum across the laser tuning range is shown in Figure 3.24. Here we can see a >40dB signal level above ASE background. These measurements confirm the absence of parasitic lasing even at the shortest operating wavelength.

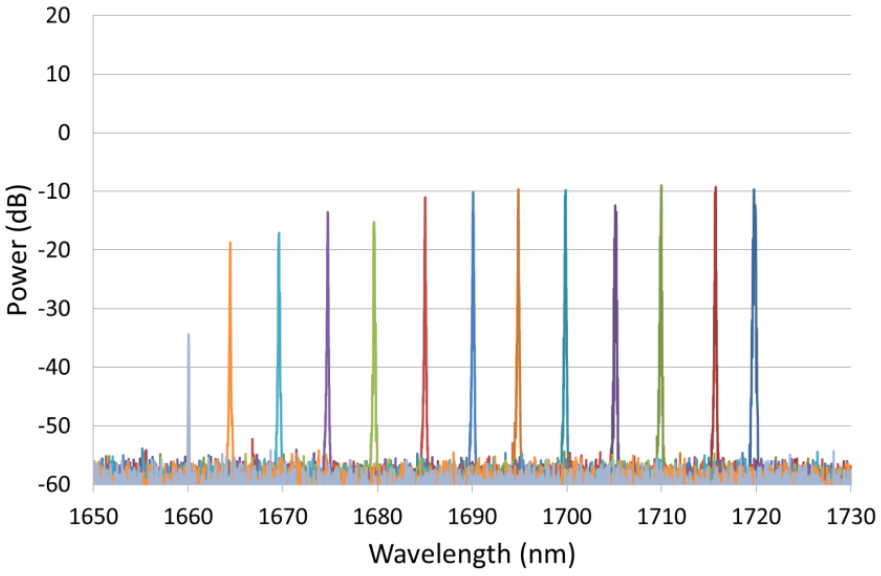

Figure 3.24 Laser output spectra across the tuning range from 1660nm to 1720nm demonstrating a >40dB height above ASE background (as measured with a 2nm spectral resolution).

These results represent the shortest wavelength operation or tunability of a thulium doped fibre laser within the published literature. This surprisingly short wavelength operation is enabled through the high efficiency of the compression tuned feedback arrangement. Here we can see a 40nm extension to the short wavelength operation of the thulium cavity in comparison to the AOTF tuned case. By utilising high efficiency feedback we are able to lower the pump threshold power at these short wavelength ranges and suppress the onset of parasitic lasing. Strong three-level laser behaviour is seen when operating in this short wavelength range and this is demonstrated by the saturation of pump absorption at the shorter wavelength end of the laser tuning curve, indicative of the high excitation density needed to reach transparency.

3.5 High efficiency 1950nm & 1726nm fibre sources

FBG's offer a robust monolithic solution for discrete wavelength selection and allow higher levels of feedback than are possible in external cavity configurations. Through the use of all fibre components system integration and power scaling are greatly simplified and allow the quick construction of high performance sources.

Within this section we demonstrate two core pumped sources operating at wavelengths of 1951nm and 1726nm. Using Bragg gratings spliced directly to the active fibre, we are able to construct these sources into monolithic cavities operating close to the quantum defect limit. The same in-house fabricated TDF was used within these experiments as was used in the previous section. Two fibre Bragg gratings, purchased from an external vendor, are used in the following experiments. The FWHM bandwidth of these FBG's were ~0.5nm at central wavelengths of 1951.1nm and 1726.4nm with reflectivities of 95% & >99% respectively. These gratings were written directly into the core of a length of SMF-28e (corning) and demonstrated single mode behaviour at both the signal and pump wavelengths. We remove the need for discrete WDM within this cavity by pumping directly through the FBG. This increased pump coupling efficiency as well as system power handling. The cavity is formed by either the short or long wavelength FBG spliced to the active fibre, providing HR feedback, and output coupling is provided by 4% Fresnel reflection. Approximately 1m of active fibre was used as the laser gain medium. Splice loss between the active fibre and FBG was estimated to be ~2% at an operating wavelength of ~1950nm.

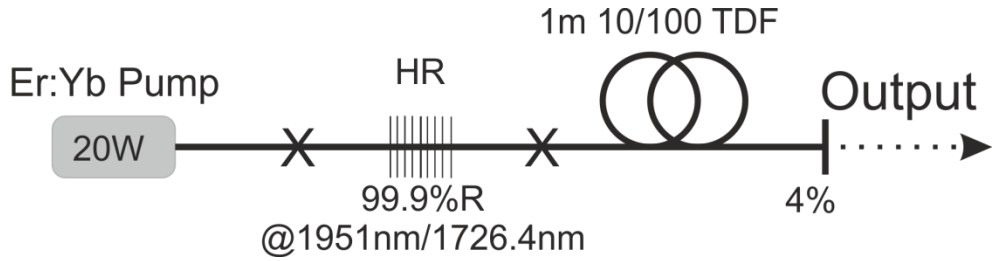

Figure 3.25. Experimental layout of monolithic all fibre source

3.5.1 Results

For an incident pump power of 20.9W, 14W of signal light was obtained at the laser operating wavelength of 1951nm corresponding to an optical to optical efficiency of 67% and slope efficiency of 69% (launched). At an operating wavelength of 1726.4nm output power was slightly reduced to a maximum power of 12.6W and slope efficiency of 63%. Single mode output was taken directly from the active fibre, threshold for the two sources was < 1W.

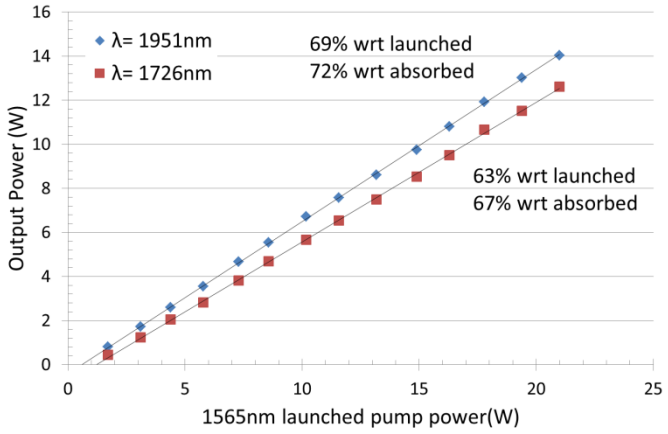

Figure 3.26 Fixed wavelength Laser performance, blue diamond's show 1951nm wavelength operation and red squares show 1726nm output.

When operating with either FBG, the laser demonstrated a narrowband output at a spectral width of <0.07nm, a high-resolution spectral trace of 1951nm operation is shown in Figure 3.27. At low pump powers, self-pulsing was present in both sources but decreased in modulation depth as pump power was increased. An oscilloscope trace of laser output at maximum pump power and 1951nm wavelength operation is shown in Figure 3.27. Here we can see a ~+/-5% ripple at microsecond rates. For 1951nm operation no evidence of ASE was seen at full pump power, with an optical signal to

noise level of >70dB measured. At 1726nm ASE power increased slightly but still maintained an optical signal to noise level of greater than 60dB (as measured at a 2nm spectral resolution).

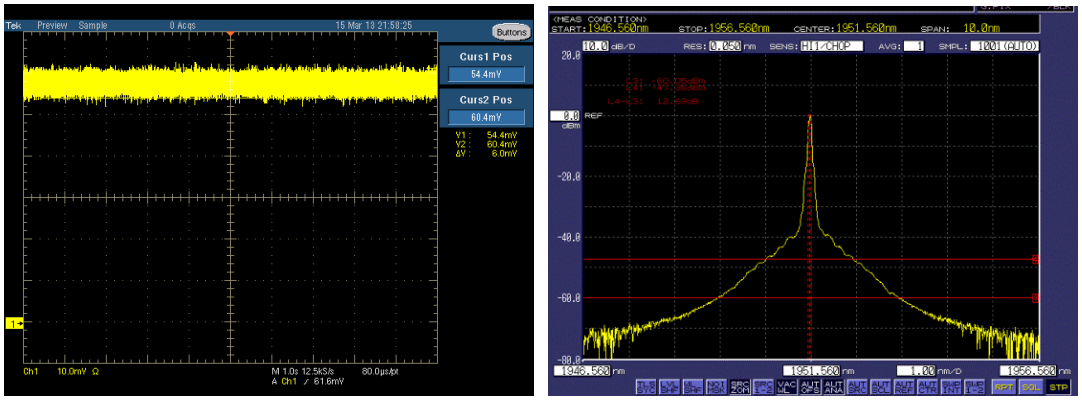

(a) (b)

Figure 3.27 (a) 1951.1nm Laser output stability at 11W output power showing +/- 5% short term variation in output power , 1s/dev. 12.5ks/s (b) laser output spectrum showing emission at 1951.5nm with a 0.06nm FWHM spectral linewidth and no evidence of ASE with a signal to noise ratio of >70dB.

3.6 Conclusion

We have investigated the wavelength coverage of thulium doped silica fibres under core and cladding pumped configurations, highlighting the effects that the varying quasi-three level nature of the $^3F_4$ – $^3H_6$ transition have on laser emission behaviour. With two different tuning techniques, we have achieved wavelength coverage of 454nm from 1660nm-2115nm.

In a cladding pumped configuration with 2.2wt%. thulium concentration and an external cavity containing an electronically addressable AOTF we have demonstrated > 4W of output power from 1930nm-2080nm. In a core pumped configuration with the same tuning element we show >1W of output from 1720-1950nm. These values correspond to a spectral power density of over 3-orders of magnitude greater than commercially available supercontinuum sources. Due to the electronically controllable nature of the AOTF, this laser configuration offers a high degree of flexibility in both operating wavelength and duty cycle. We demonstrate this with the dual wavelength operation of a cladding pumped thulium source, with the individual lasing wavelengths controlled digitally. We

also demonstrate low duty cycle operation of this source with a fast rise time and low off state light leakage. The combination of high power, flexibility in operating wavelength and very high spectral power density afforded by this approach should benefit a range of applications in sensing, spectroscopy and component characterisation as well as proving a platform for nonlinear frequency conversion to the mid-infrared wavelength range.

We extended the short wavelength operation of a core pumped thulium source through the use of a high efficiency compression tuned FBG, allowing laser operation from 1720nm down to 1660nm. This tuning range represents the shortest wavelength operation of a thulium source operating on the $^3F_4$ – $^3H_6$ transition within published literature. Output powers in this tunable configuration were limited by power handling of the filter type WDM, but an initial slope efficiency measurement of >35% close to threshold (at 1680nm) suggest that reasonable conversion efficiencies should be possible. By moving to a fixed wavelength operation it was possible to remove the need for discrete WDM, allowing pumping directly through fixed wavelength FBG's removing the damage limitations of the previous WDM. 1950nm &1726nm wavelength operation was investigated in this configuration, with 14W & 12.6W achieved at internal slope efficiencies of 72% & 69% respectively. Again, the output power of 12.6W at 1726nm represents the highest reported value within literature. Several applications have been highlighted for short wavelength thulium operation, including the targeting of C-H resonances at 172xnm. With the potential to be a very large application space, its use in dermatological applications such as the treatment of acne [2] and for absorber free laser processing of polymers [3] has great commercial potential. At still shorter wavelengths, the pumping of Dysprosium fluoride fibres at 1680nm for direct laser operation in 3400 & 4500nm wavelength bands [24] is another attractive application.

References

1. D. Theisen, V. Ott, H. W. Bernd, V. Danicke, R. Keller, and R. Brinkmann, "Cw high power IR-laser at 2um for minimally invasive surgery," in *Therapeutic Laser Applications and Laser-Tissue Interactions* (2003), Vol. 5142, p. 5142_96.

2. V. V Alexander, K. Ke, Z. Xu, M. N. Islam, M. J. Freeman, B. Pitt, M. J. Welsh, and J. S. Orringer, "Photothermolysis of sebaceous glands in human skin ex vivo with a 1,708 nm Raman fiber laser and contact cooling.," Lasers Surg. Med. **43**, 470–80 (2011).

3. I. Mingareev, F. Weirauch, A. Olowinsky, L. Shah, P. Kadwani, and M. Richardson, "Welding of polymers using a 2μm thulium fiber laser," Opt. Laser Technol. **44**, 2095–2099 (2012).

4. P. Kadwani, R. Sims, J. Chia, F. Altat, L. Shah, and M. Richardson, "Atmospheric Propagation Testing Using Broadband Thulium Fiber Systems," in *Advances in Optical Materials* (OSA, 2011), p. FWB3.

5. *IEC 60825-1: Safety of Laser Products Part 1: Equipment Classification, Requirements and User's Guide* (International Electrotechnical Commission, 2001).

6. J. Cariou, B. Augere, and M. Valla, "Laser source requirements for coherent lidars based on fiber technology," Comptes Rendus Phys. **7**, 213–223 (2006).

7. A. Hemming, J. Richards, A. Davidson, N. Carmody, S. Bennetts, N. Simakov, and J. Haub, "99 W mid-IR operation of a ZGP OPO at 25% duty cycle," Opt. Express **21**, 10062 (2013).

8. Z. Li, a. M. Heidt, J. M. O. Daniel, Y. Jung, S. U. Alam, and D. J. Richardson, "Thulium-doped fiber amplifier for optical communications at 2 μm," Opt. Express **21**, 9289 (2013).

9. B. M. Walsh and N. P. Barnes, "Comparison of Tm:ZBLAN and Tm:silica fiber lasers; Spectroscopy and tunable pulsed laser operation around 1.9um," Appl. Phys. B **78**, 325–333 (2004).

10. P. Moulton, "High power Tm: silica fiber lasers: current status, prospects and challenges (Invited)," Eur. Conf. Lasers Electro-Optics (2011).

11. D. M. Sonnenfroh and M. G. Allen, "Absorption measurements of the second overtone band of NO in ambient and combustion gases with a 1.8um room-temperature diode laser," Appl. Opt. **36**, 7970–7 (1997).

12. A. Rocco, G. De Natale, and P. De Natale, "A diode-laser-based spectrometer for in-situ measurements of volcanic gases," Appl. Phys. B **240**, 235–240 (2004).

13. G. Gagliardi, A. Castrillo, and R. Q. Iannone, "High-precision determination of the 13CO2/12CO2 isotope ratio using a portable 2.008-μm diode-laser spectrometer," Appl. Phys. B **77**, 119–124 (2003).

14. J. Flaud, A. Barbe, and N. Husson, "REFERENCES and SOURCES for HITRAN," 4058–4097 (2013).

15. P. Cerny, "Developing thulium lasers for depth-selective scalpels," SPIE Newsroom (2006).

16. N. J. Scott, C. M. Cilip, and N. M. Fried, "Thulium Fiber Laser Ablation of Urinary Stones Through Small-Core Optical Fibers," IEEE J. Quantum Electron. **15**, 435–440 (2009).

17. G. M. Hale and M. R. Querry, "Optical Constants of Water in the 200-nm to 200-micron Wavelength Region.," Appl. Opt. **12**, 555–63 (1973).

18. J. W. Jr and L. Weyer, *Practical Guide and Spectral Atlas for Interpretive Near-Infrared Spectroscopy* (2012).

19. A. S. Kurkov, V. V. Dvoyrin, and A. V. Marakulin, "All-fiber 10 W holmium lasers pumped at λ=1.15 μm," Opt. Lett. **35**, 490 (2010).

20. B. Q. Yao, L. L. Zheng, R. L. Zhou, X. M. Duan, Y. J. Zhang, Y. L. Ju, Y. Z. Wang, G. J. Zhao, and Q. Dong, "Holmium laser in-band pumped by a thulium laser in the same host of YAlO3," Laser Phys. Lett. **18**, 1501–1504 (2008).

21. M. Mond, D. Albrecht, E. Heumann, G. Huber, S. Kück, V. I. Levchenko, V. N. Yakimovich, V. G. Shcherbitsky, V. E. Kisel, N. V Kuleshov, M. Rattunde, J. Schmitz, R. Kiefer, and J. Wagner, "1.9- m and 2.0- m laser diode pumping of Cr(2+) :ZnSe and Cr(2+) :CdMnTe.," Opt. Lett. **27**, 1034–6 (2002).

22. J. Junhua, S. Yoo, P. Shuam, and J. Nilsson, "Minimize quantum-defect heating in thulium-doped silica fiber amplifiers by tandem-pumping," in *Photonics Global Conference (PGC)* (IEEE, 2012), pp. 1–3.

23. D. Creeden, B. R. Johnson, S. D. Setzler, and E. P. Chicklis, "Resonantly pumped Tm-doped fiber laser with >90% slope efficiency," Opt. Lett. **39**, 470 (2014).

24. R. S. Quimby and M. Saad, "Dy:fluoroindate Fiber Laser at 4.5 μm with Cascade Lasing," in *Advanced Solid-State Lasers Congress* (OSA, 2013), p. AM2A.7.

25. I. Divliansky, A. Jain, D. Drachenberg, A. Podvyaznyy, V. Smirnov, G. Venus, and L. Glebov, "Volume bragg lasers," in *Proc. SPIE. Vol. 7751.* (2010), p. 77510Z–77510Z–10.

26. Y. Song and S. Havstad, "40-nm-wide tunable fiber ring laser with single-mode operation using a highly stretchable FBG," Photonics Technol. Lett. IEEE **13**, 1167–1169 (2001).

27. M. Mokhtar, C. Goh, and S. Butler, "Fibre Bragg grating compression-tuned over 110 nm," Electron. Lett. **39**, 509–511 (2003).

28. "3SP Group," http://www.3spgroup.com/3SPG/Home.php?locale=en.

29. "Nova Write," http://www.novawrite.com/.

30. "NP Photonics," http://www.npphotonics.com/.

31. "Golight Technology Co.,Ltd," http://www.go2light.com/en/index.asp.

32. "keopsys," http://www.keopsys.com/.

33. "V-gen Pulsed Fiber Laser," http://www.vgen.com/.

34. "PicoLuz," http://www.picoluz.com/.

35. "NKT Photonics," http://www.nktphotonics.com.

36. "Fianium Ltd.," http://www.fianium.com/.

37. "AdValue Photonics," http://www.advaluephotonics.com/.

38. "Lisa Laser OHG," http://www.lisalaser.de.

39. "StarMedTec GmbH," http://www.starmedtec.de.

40. G. D. Goodno, L. D. Book, and J. E. Rothenberg, "Low-phase-noise, single-frequency, single-mode 608 W thulium fiber amplifier," Opt. Lett. **34**, 1204–1206 (2009).

41. T. Ehrenreich, R. Leveille, I. Majid, G. Rines, P. F. Moulton, Q-Peak, and Nufern, "1-kW All-Glass Tm:fiber Laser," in *SPIE Photonics West* (2010).

42. M. Meleshkevich, N. Platonov, D. Gapontsev, A. Drozhzhin, V. Sergeev, and V. Gapontsev, "415W Single-Mode CW Thulium Fiber Laser in all-fiber format," in *European Conference on Lasers and Electro-Optics* (2007).

43. W. A. Clarkson, N. P. Barnes, P. W. Turner, J. Nilsson, and D. C. Hanna, "High-power cladding-pumped Tm-doped silica fiber laser with wavelength tuning from 1860 to 2090 nm," Opt. Lett. **27**, 1989 (2002).

44. D. Y. Shen, J. K. Sahu, and W. A. Clarkson, "High-power widely tunable Tm:fibre lasers pumped by an Er,Yb co-doped fibre laser at 1.6 μm," Opt. Express **14**, 6084 (2006).

45. Y. Tang, Y. Yang, and J. Xu, "High Power Tm3+-Doped Fiber Lasers Tuned by a Variable Reflective Output Coupler," Res. Lett. Opt. **2008**, 1–3 (2008).

46. Z. S. Sacks, Z. Schiffer, and D. David, "Long wavelength operation of double-clad Tm:silica fiber lasers," in *Proceedings of SPIE* (2007), Vol. 6453.

47. T. McComb, R. A. Sims, C. C. C. Willis, P. Kadwani, V. Sudesh, L. Shah, and M. Richardson, "High-power widely tunable thulium fiber lasers.," Appl. Opt. **49**, 6236–42 (2010).

48. J. Geng, Q. Wang, J. Wang, S. Jiang, and K. Hsu, "All-fiber Tm-doped wavelength-swept laser," Conf. Lasers Electro-Optics JW2A.63 (2012).

49. Z. Li, S. U. Alam, Y. Jung, a. M. Heidt, and D. J. Richardson, "All-fiber, ultra-wideband tunable laser at 2 μm," Opt. Lett. **38**, 4739 (2013).

50. N. Y. Voo, J. K. Sahu, and M. Ibsen, "345-mW 1836-nm single-frequency DFB fiber laser MOPA," IEEE Photonics Technol. Lett. **17**, 2550–2552 (2005).

51. J. Geng, J. Wu, S. Jiang, and J. Yu, "Efficient operation of diode-pumped single-frequency thulium-doped fiber lasers near 2 micro m.," Opt. Lett. **32**, 355–7 (2007).

52. W. L. Barnes, J. P. Dakin, H. O. Edwards, L. Reekie, J. E. Townsend, S. C. Murray, and D. Pinchbeck, "Tunable fiber laser source for methane detection at 1.68 um," in *Fibers' 92. International Society for Optics and Photonics* (1993), Vol. 1796, pp. 110–114.

53. S. Agger, J. Povlsen, and P. Varming, "Single-frequency thulium-doped distributed-feedback fiber laser," Opt. Lett. **29**, 1503–1505 (2004).

54. L. Pearson, J. W. Kim, Z. Zhang, J. K. Sahu, M. Ibsen, and W. A. Clarkson, "High-Power Single-Frequency Thulium-Doped Fiber Master-Oscillator Power-Amplifier at 1943nm," in *Conference on Lasers and Electro-Optics* (2009), pp. 3–4.

55. J. Geng, Q. Wang, J. Smith, T. Luo, F. Amzajerdian, and S. Jiang, "All-fiber Q-switched single-frequency Tm-doped laser near 2μm," Opt. Lett. **34**, 3713–3715 (2009).

56. D. Gapontsev, N. Platonov, M. Meleshjevich, O. Mishechkin, O. Shkurikhin, S. Agger, P. Varming, and J. . Poylsen, "20W single-frequency fiber laser operating at 1.93 um," Eur. Conf. Lasers Electro-Optics 9–10 (2007).

57. L. Pearson, J. W. Kim, Z. Zhang, M. Ibsen, J. K. Sahu, and W. A. Clarkson, "High-power linearly-polarized single-frequency thulium-doped fiber master-oscillator power-amplifier," Opt. Express **18**, 1607 (2010).

58. Z. Zhang, A. J. Boyland, J. K. Sahu, W. A. Clarkson, and M. Ibsen, "High Power , Single Frequency Thulium-doped Fiber DBR Laser at 1943 nm," Quantum 2–4 (2010).

59. N. Coluccelli, G. Galzerano, P. Laporta, F. Cornacchia, D. Parisi, and M. Tonelli, "Tm-doped LiLuF4 crystal for efficient laser action in the wavelength range from 1.82 to 2.06 microm.," Opt. Lett. **32**, 2040–2 (2007).

60. J. M. Cano-Torres, M. Dolores Serrano, C. Zaldo, M. Rico, X. Mateos, J. Liu, U. Griebner, V. Petrov, F. José Valle, M. Galán, and G. Viera, "Broadly tunable laser operation near 2μm in a locally disordered crystal of Tm 3+ -doped NaGd(WO 4) 2," J. Opt. Soc. Am. B **23**, 2494 (2006).

61. A. Physics and P. Bundesanstalt, "Efficient tunable laser operation of diode-pumped Yb,Tm : KY(WO4)2 around 1.9μm," **461**, 457–461 (2002).

62. R. C. Stoneman and L. Esterowitz, "Efficient, broadly tunable, laser-pumped Tm:YAG and Tm:YSGG cw lasers.," Opt. Lett. **15**, 486–8 (1990).

63. V. Petrov, F. Guell, J. Massons, J. Gavalda, R. M. Sole, M. Aguilo, F. Diaz, and U. Griebner, "Efficient tunable laser operation of Tm:KGd(WO4)2 in the continuous-wave regime at room temperature," IEEE J. Quantum Electron. **40**, 1244–1251 (2004).

64. E. C. Honea, R. J. Beach, S. B. Sutton, J. A. Speth, S. C. Mitchell, J. A. Skidmore, M. A. Emanuel, and S. A. Payne, "115-W Tm:YAG diode-pumped solid-state laser," IEEE J. Quantum Electron. **33**, 1592–1600 (1997).

65. K. S. Lai, P. B. Phua, R. F. Wu, Y. L. Lim, E. Lau, S. W. Toh, B. T. Toh, and a Chng, "120-W continuous-wave diode-pumped Tm:YAG laser.," Opt. Lett. **25**, 1591–3 (2000).

66. F. Träger, *Springer Handbook of Lasers and Optics* (Springer, 2007), p. 1332.

67. N. Barnes, R. Allen, L. Esterowitz, E. Chicklis, M. Knights, and H. Jenssen, "Operation of an Er:YLF laser at 1.73 μm," IEEE J. Quantum Electron. **22**, 337–343 (1986).

68. D. Y. Shen, J. K. Sahu, and W. A. Clarkson, "Highly efficient in-band pumped Er:YAG laser with 60 W of output at 1645nm.," Opt. Lett. **31**, 754–756 (2006).

69. H. Jelínková and M. Doroshenko, "Resonant pumping of dysprosium doped lead thiogallate by 1.7 μm Er: YLF laser radiation," Laser Phys. … **353**, 349–353 (2011).

70. N. P. Barnes and R. E. Allen, "Room temperature Dy:YLF laser operation at 4.34 mu m," IEEE J. Quantum Electron. **27**, 277–282 (1991).

71. C. A. Codemard, P. Dupriez, Y. Jeong, J. K. Sahu, M. Ibsen, and J. Nilsson, "High-power continuous-wave cladding-pumped Raman fiber laser," Opt. Lett. **31**, 2290 (2006).

72. W. W. Rigrod, "Saturation Effects in High-Gain Lasers," J. Appl. Phys. **36**, 2487 (1965).

73. M. Tokurakawa, J. M. O. Daniel, S. Chenug, H. Liang, and W. A. Clarkson, "Ultra-broadband Wavelength Swept Tm-doped Fibre Laser," in *European Conference on Lasers and Electro-Optics* (2013), p. CJ–7.5.

Chapter 4.

Temporally incoherent fibre sources

4.1 Introduction

Amplified spontaneous emission (ASE) sources can offer broad bandwidths and low temporal coherence whilst still possessing high spatial coherence and brightness. Such superluminescent sources are of great use for a number of applications. Within the white light interferometry and optical coherence tomography (OCT) sectors the excellent temporal stability and wide wavelength coverage of these sources have ensured wide adoption [1,2]. In this chapter we will present several different techniques for the generation of broad bandwidth ASE light, studying in detail the generation of pulsed ASE light in Q-switched fibre sources. We will then apply this pulsed ASE source to the generation of a broad wavelength band through supercontinuum generation via a simple, low cost, highly nonlinear fibre. Finally, we investigate the suppression of modal interference in multimode amplifiers using this broad bandwidth seed source.

The typical approach for the generation of broadband ASE light is through suppression of feedback in a high gain laser medium. Here the total feedback of an optical cavity is reduced to a level at which round trip gain is less than unity. By doing so, any longitudinal mode generation (through resonator feedback) is suppressed and the cavity output is a broadband amplified spontaneous emission. Generally the spectral output of these sources is simply determined by the gain bandwidth of the lasing material. However, for some applications it is desirable to enhance wavelength coverage of some spectral regions at the cost of others, or to modify the spectral shape or flatness of the source [3,4]. The most direct approach to achieve this wavelength control is through wavelength selective feedback to the ASE source. However, a trade-off must be made

between the desire for strong wavelength control and the need to maintain low enough levels of feedback to suppress parasitic lasing. These issues mean it is more common to spectrally filter the ASE light after generation rather than shape it with an external feedback arrangement.

Within this chapter we explore the use of pulsed fibre sources rather than feedback suppression for ASE generation. It is possible to use the fast dynamics of a Q-switched fibre source as a means of generating ASE light. This is due to a high small signal gain and resulting fast pulse build-up time seen within a fibre cavity when operated in Q-switched mode. Here, longitudinal modes do not have time to become established before the pulse energy is extracted from the fibre. This approach to ASE generation has the advantage of relying on cavity dynamics rather than feedback suppression at the output of the source, allowing for much higher levels of feedback and resulting in strong spectral control and higher extraction efficiencies.

Before describing this behaviour in more detail, we must first clarify what is meant by Q-switch in such an arrangement. Strictly speaking, Q-switching implies resonator behaviour, however within this work we use the term Q-switching to describe a modulation of round trip cavity loss, this definition is more in line with common usage within the fibre laser community and is therefore maintained here for simplicity. A conceptual layout of a Q-switched fibre source is shown in Figure 4.1.

In the ‘off’ state of a Q-switched fibre source, cavity feedback is suppressed and inversion builds up within the gain medium. High levels of inversion lead to amplified spontaneous emission within the cavity, which is directed towards the cavity end with lowest feedback, in this case towards the Q-switch. This ASE light is then dumped by the off-state Q-switch. Eventually, for continued pumping, this increasing ASE will clamp cavity inversion and the source will behave like that of a feedback suppressed ASE architecture. When the Q-switch is then transferred into the ‘on’ state, this nominally dumped ASE light is fed back into the cavity. Here, due to high levels of inversion, this ASE light is strongly amplified through several round trips of the cavity. Eventually this light becomes sufficiently intense to saturate the gain and a pulse is extracted [5]. Due to the low number of round trips required to reach this saturation, longitudinal modes do not have time to become established before pulse extraction; and the output is simply a time gated amplified spontaneous emission. Here the difference to a standard feedback

suppressed ASE source is the larger number of round trips for amplification. This enables much higher extraction efficiency for a given pump power and reduces any excess gain that could lead to parasitic lasing. Within this picture we can think of a Q-switched fibre source as a self-seeded multipass amplifier rather than a traditional laser source. The above picture is in comparison to a lower gain system such as a more traditional bulk laser, where ASE is generally less of a contributing factor and pulse energy extraction is achieved after longitudinal mode formation and a large number of round trips.

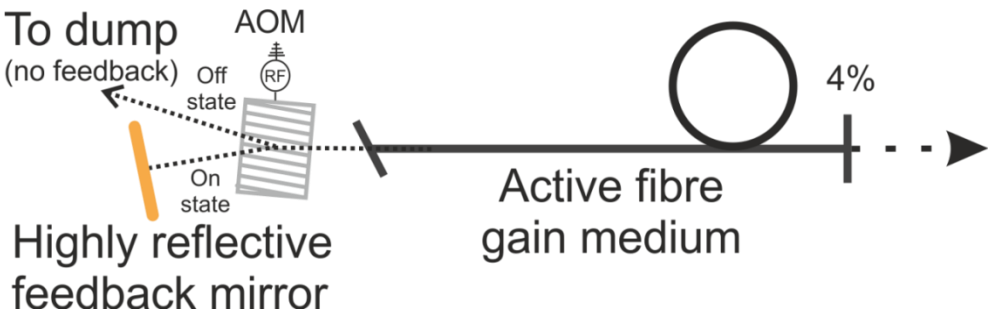

Figure 4.1 Conceptual layout of a typical free space Q-switched fibre laser cavity with acousto-optic modulator (AOM)

As this fibre cavity behaves like a multipass amplifier, seeded by broadband ASE light, we can use spectral control within the feedback cavity to define the spectral bandwidth or the central wavelength of any back reflected light. As this spectral shaping and filtering is used during the initial pulse formation, only low levels of light are lost. Here no significant power penalty is incurred from this wavelength control. This approach allows the spectral shape of the emitted ASE light to be controlled with a high degree of fidelity without affecting the source efficiency or output power. On top of this, the relatively high levels of optical feedback for this cavity result in high extraction efficiencies and reduced sensitivity to back reflection from downstream components. This is in comparison to feedback suppressed ASE sources that show high sensitivity to back reflection and require protection with high performance optical isolators.

4.2 Background

Under steady state conditions the emission from a laser oscillator is made up of a number of longitudinal modes or discrete wavelengths, with the spacing between adjacent modes given by $\lambda^2/2nL$. Interference effects similar to that of a Fabry–Pérot interferometer lead to this discrete mode formation within the resonator. Here preferential lasing occurs at

wavelengths resonant with the cavity. On top of this mode formation is the spectrally dependent gain of the lasing material. The result of these two effects is a laser emission showing a series of regularly spaced wavelengths with a broader band wavelength envelope. An ASE source on the other hand, does not contain longitudinal modes and is simply a continuous spectra defined by the emitted envelope. This can be achieved through the suppression of Fabry–Pérot resonator effects, where in the simplest case the round trip gain of the cavity is reduced to less than unity. Here the cavity experiences a net loss for any oscillating light and so these resonator interference effects are no longer present.

In this picture, for any significant amount of ASE light to be generated, the small signal gain must be very high. This favours waveguided sources, where small transverse dimensions and high spatial overlap between inversion and guided mode is seen.

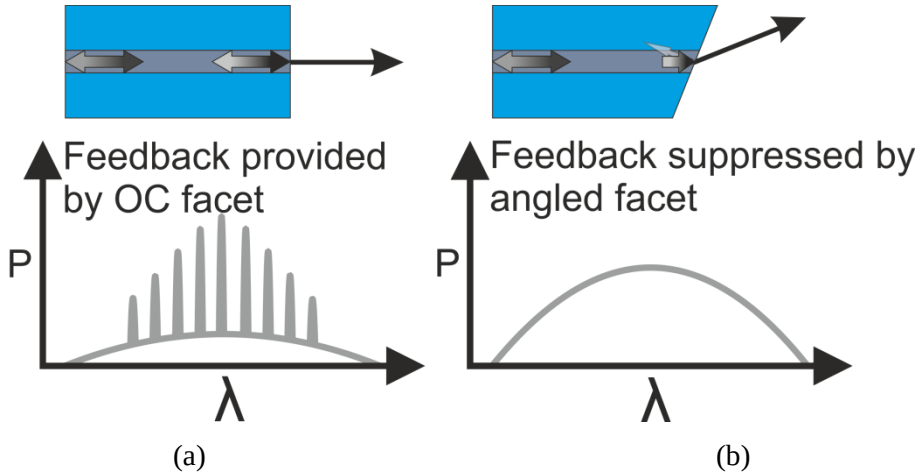

Figure 4.2 Spectral emission behaviour of a Laser (a) and ASE (b) source, demonstrating longitudinal mode formation in (a) and suppression in (b).

In order to suppress lasing within such a cavity, we must ensure that high levels of output coupling are present. For the extremely high gain seen in typical fibre sources this means that even the feedback from the ~4% Fresnel reflection (present at the glass air interface) must be suppressed. Several different approaches have been developed to achieve this aim. Typically feedback suppression within waveguides can be split into two categories. Firstly, suppression of this Fresnel reflection can be achieved through the use of anti-reflective coatings at the air/waveguide interface. Secondly, techniques can be used to suppress the recoupling of the back reflection, rather than suppressing the reflection itself. Within a fibre waveguide this can take the form of angle cleaved end facet, where the

resulting tilt placed on back-reflected wavefront significantly lowers its effective coupling efficiency. The use of angle cleaving can be remarkably successful, with levels of feedback suppression typically in the range of >50dB (loss) for angle-cleaved or polished facets. The lower limits of feedback suppression are ultimately governed by backscatter within the fibre itself.

4.2.1 Prior demonstrations of high power ASE sources

Typical demonstrations of ASE sources are in the 10's to 100's of mW level and are considered standard pieces of equipment within the telecoms industry. However if non-standard wavelengths or high power levels are desired sources must generally be constructed in-house. Within the literature there have been several prominent demonstrations of high power or high configurability ASE sources. Demonstrations utilising Yb doped fibre hosts are the most developed within this area. In 2006 Wang et.al [6] demonstrated 110W of output power within a 37nm bandwidth with a dual ended output. The slope efficiency was 67% and the beam quality of this source M^2=1.6. Later this work was extended to single ended operation at power levels of 62W and amplified to 120W [7]. Both of these demonstrations represented significant power scaling in comparison to previous works [8,9] and were enabled by a novel twisted fibre feedback suppression scheme. A similar approach was applied to thulium doped active fibre in [10]. The output of this source was single ended with up to 11W of ASE light centred at 1950nm. In this work a spectral bandwidth of 280nm was demonstrated at low power levels (~mW), however the bandwidth quickly narrowed to ~30nm for increased pump power. Again the approach taken in this work was feedback suppression through angle cleaving.

The above demonstrations highlight the significant power levels that can be achieved in fibre based ASE sources. However, the reliance on such high levels of feedback suppression and the use of free space configurations is non-ideal. In order for these sources to demonstrate practical application, it is desirable to move to a more fiberized solution. With this in mind demonstrations of all-fibre MOPA configurations have produced very impressive results. With up to 1.1kW of ASE output demonstrated at an operating wavelength of 1030nm [11,12]. More recently all fibre configurations have also been demonstrated at longer wavelengths, with 25W of output power centred at 2000nm [13]. Both of these demonstrations consisted of low power ASE seeds that were

then amplified through several gain stages to the desired power level. In the case of [11] this required a total of 5 amplifier stages to reach an output power of 1.1kW. The reason such a large number of amplifiers were required was the need to maintain low power levels in the ASE seed and ensure suppression of parasitic lasing. In addition to this the authors also used spectral filtering after ASE generation, leading to strong seed attenuation.

As mentioned in the introduction, it is of interest to control the operating wavelength of these ASE sources. Several different approaches can be taken to achieve this. Spectral filtering after ASE generation is straightforward to achieve but must come at the cost of output power. Other approaches have been successfully implemented using intracavity wavelength control [14–16]. For example, the use of an external feedback arrangement containing a diffraction grating for wavelength control [16]. Within this arrangement, light is spatially dispersed by the diffraction grating and an array of variable height metal pins are positioned to attenuate the dispersed spectrum. By changing the height of an individual pin, the level of aperaturing, and hence attenuation, of different wavelength components can be controlled. This allowed the authors to 'flatten' the back reflected ASE light, moving from a bandwidth of ~30nm to 62nm. The approach of intracavity wavelength selection is versatile and does not require the sacrificing of efficiency. The main limitation of spectral control in feedback suppressed sources is the balance that is required between sufficient feedback for wavelength control and the suppression of parasitic lasing. This is demonstrated in the above result, where output powers were limited to <100mW before the onset of parasitic lasing.

Here we see both the impressive results that can be achieved with fibre-based ASE sources, but also the limitations imposed by their high sensitivity to feedback. As mentioned in the introduction, Q-switched fibre lasers can be used as an alternative to feedback-suppressed ASE sources. When operated in a high gain regime, and provided Q-switched gate operation is sufficiently fast, they can be an efficient and robust source of pulsed ASE light. The advantage of this arrangement is the ability to use a relatively high cavity Q. Here we are no longer relying on feedback suppression for ASE generation but rather exploiting cavity dynamics. With this pulsed arrangement, ASE can be produced with relatively low sensitivity to back-reflections from downstream components. In addition to this, due to the higher levels of feedback, more efficient power extraction is achievable in comparison to feedback suppressed sources. Within the

experimental section of this chapter we will explore this behaviour. Investigating the number of round trips required for pulse formation as well as the application of spectral control within the Q-switched cavity.

4.3 Applications of broadband sources

This section provides the background motivation for the two applications that will later be experimentally demonstrated within this chapter. First we will look at long wavelength optical coherence tomography, where the high peak powers and broad wavelength coverage enabled by this pulsed ASE source allows high-resolution depth measurements of semi-transparent samples. We will then look the effects of modal interference within multimode fibres, experimentally demonstrating the suppression of these detrimental effects by use of an ASE source with a broad operating bandwidth.

4.3.1 Coherence length and optical coherence tomography

Optical coherence tomography (OCT) is a non-destructive technique that allows high resolution, volumetric images to be constructed through the depth scanning of a semi-transparent medium [17]. This is achieved using white light interferometry, where through the collection of many depth scans a three-dimensional picture is formed of a sample under test. The most prominent use of this technique is within the medical sector, where it is commonly used as a tool to allow non-destructive volume mapping of various biological samples, such as the human eye. Whilst primarily a tool for the medical sector OCT has found use within many other fields [18–21], such as the recent demonstration of the analysis of individual layers of a multi-layer stacked grin lens [22].

In the most basic sense, an OCT system is simply a Michelson interferometer with a variable length reference arm and fixed sample arm (Figure 4.3). When interrogated with white light, interference fringes will only form when the two arms have matching length. The coherence length of the interrogating light source defines the degree to which these two arms must match and thus the resolution of the technique. If a sample with multiple layers is inserted into the interferometer, interference between the sample and reference arm will occur at several different positions. By recording the position of the reference arm when these interference events occur, the position of the individual layers within the sample can be found.

4.3.1.1 The Michelson interferometer

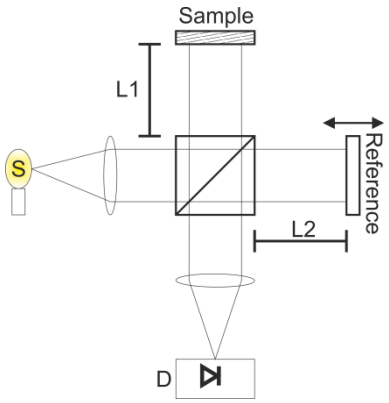

Figure 4.3 Conceptual layout of a Michelson interferometer. S, denotes the incident light source, L_1 & L_2 are the relative path lengths of the sample and reference arms respectively and D is a photodiode used to monitor transmitted power.

The optical path length difference between the sample and reference arms of the above interferometer is given by:

$$\Delta = 2(L_1 - L_2) \tag{24}$$

For monochromatic light, translating the length of L_2 will result in a sinusoidal intensity change as described by [23]:

$$I(\Delta) = I_1 + I_2 + 2\sqrt{I_1 I_2}\cos(k_0 \Delta) \tag{25}$$

where, I_1 and I_2 are the initial intensity in the two arms of the interferometer and λ_0 is wavelength of incident light. In reality the incident light will have a non-zero bandwidth, which for the sake of simplicity we will describe by a Gaussian function:

$$I(k) = I_0 exp - \left(\frac{2\sqrt{ln2}(k - k_0)}{\Delta \mathrm{k}}\right)^2 \tag{26}$$

where $\Delta k \approx 2\pi\ \Delta\lambda\ /\ \lambda^2_0$ is the full width of the spectral bandwidth at half maximum (FWHM) and λ_0 the central wavelength of the source.

With this source now used to interrogate the interferometer, the resulting intensity profile with respect to path length mismatch is given by:

$$I(\Delta) = I_1 + I_2 + 2\sqrt{I_1 I_2} exp - \left(\frac{\Delta k * \Delta}{2\sqrt{ln2}}\right)^2 \cos(k_0 \Delta) \quad (27)$$

We can now define the coherence length L_c of the light source as the value of Δ at which the interferogram drops to half its maximum, i.e.

$$L_c = \frac{2ln(2)}{\pi n}\frac{\lambda_0^2}{\Delta\lambda} \approx \frac{0.44}{n} * \frac{\lambda_0^2}{\Delta\lambda} \quad (28)$$

From Eq.(27) we can see that rather than a continuously oscillating function, the intensity of the interference pattern now decays with a Gaussian shape as the reference arm is scanned. The bandwidth of the source, as well as its central wavelength, dictate the rate at which this Gaussian envelope decays. These two values define the coherence length of the source, as seen in Eq.(28). The coherence length of the source scales as a function of wavelength squared and is inversely proportional to bandwidth. From this we can see that short wavelengths and broad bandwidths are desirable to reduce coherence length, and thus increase the resolution of the technique.

Figure 4.4 plots the behaviour of two white light sources with Gaussian spectral shape. Bandwidths are 50nm and 100nm FWHM, both with a central wavelength of 1000nm. As can be seen the FWHM of this interferogram is ~9μm for Δλ=50nm and ~4.4μm for Δλ=100nm, corresponding to the coherence length of the two sources. From this we can see that two points must be separated by greater than the coherence length if they are to be individually resolved.

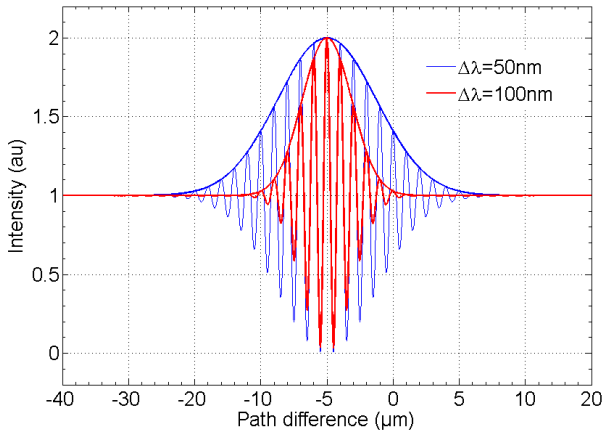

Figure 4.4 Expected intensity profile on detector for a Gaussian shaped input sources and scanned reference arm. With spectral bandwidths of $\Delta\lambda$=50nm (blue) & $\Delta\lambda$=100nm (red) and central wavelength of λ_0=1μm.

4.3.1.2 Long wavelength OCT for art conservation

Within galleries containing historical works, a constant maintenance program must be carried out to maintain the appearance and 'health' of these important works. This is due to aging of protective varnishes and deterioration of previous restoration process. Typical restoration and maintenance process are time consuming and labour intensive. The original components of the painting need identification before restoration can be carried out and this is often dependent on the skill and experience of the restoration worker. Maintenance processes can include the removal of old varnish layers through mechanical and chemical means as well as identification of previous restoration attempts. Towards this aim, a range of different techniques are employed including the use of x-ray and infrared imagery. A promising application of OCT is in the analysis of these features, allowing a sub-surface look within the paintings.

The use of OCT to augment existing diagnostics as well as allowing further identification of individual layers of these paintings is of great interest. Figure 4.5(i.a) shows an example of OCT applied to this application. Taken with a 900nm central wavelength source, the letter 'A' on the image marks the area under test. Figure 4.5(i.b) shows a microscope image of the painting (taken destructively) and Figure 4.5(i.c) shows a two-dimensional OCT line scan of the painting within the same region.

Current commercial options for OCT are non-ideal for imaging paintings. The commonly used pigments within these works tend to lack transparency within both the visible and

short wave infrared. Whilst opaque at shorter wavelengths, a large proportion of these pigments show higher levels of transparency when moving to longer wavelengths. Analysis of commonly used pigments for absorption and transmission properties has identified a window within the 1800-2200nm wavelength range that demonstrates good transparency. The use of light sources within this window shows promise for OCT analysis of these works [24]. Figure 4.5(ii) shows the averaged transparencies across several commonly used pigments (with transparency normalised to one at a wavelength of 2200nm). Current commercial options for broadband sources within this wavelength range are limited. As part of a project involving Nottingham Trent University and the National gallery, several broadband sources were developed within this wavelength range. The results of which will be discussed throughout the chapter.

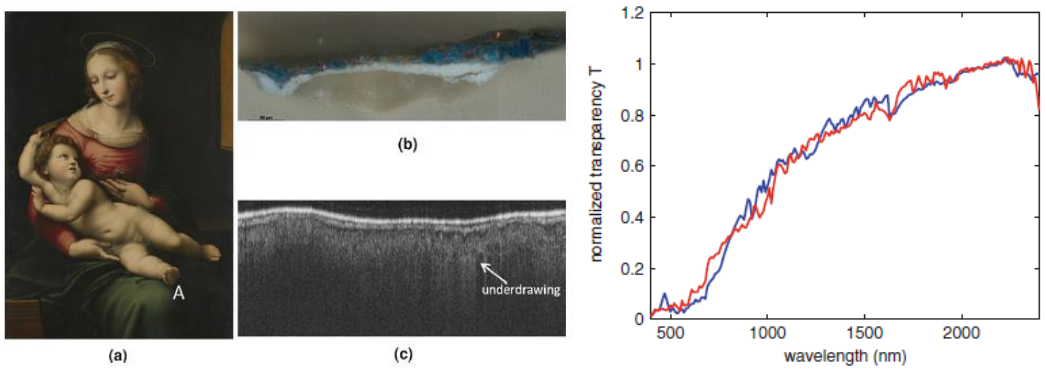

(i) (ii)

Figure 4.5 (i.a) A sample work 'The Madonna and Child ~1600" used to perform comparisons between destructive material removal (i.b) and a non-destructive OCT scan (i.c). Position 'A' on the image denotes the area over which the cross section and OCT scans were taken. (ii) Plot showing the averaged transparency across several pigments normalised to a transparency of T=1 at 2200nm [24].

4.3.2 Power scaling within multimode waveguides

As is a continuing theme within the fibre laser community, the desire for ever increasing output powers pushes fibre core scaling techniques forward. By moving to larger areas, increases of output power and pulse energies are possible. This is due to both increased energy storage as well as decreased effects of detrimental nonlinear processes. However difficulties arise when core size is increased beyond the single mode limit. As core area is expanded to a point where guidance is no longer strictly single mode, steps must be taken to ensure single mode propagation (e.g. via bend loss induced mode-filtering, fibre

design, etc.). For further area scaling, these solutions become less effective and ultimately put a practical upper limit on core size if single mode output is required [25].

An alternative to this approach of maintaining single mode guidance within a multimode fibre is to sacrifice single mode beam quality and move to a multimode output regime. Whilst published literature has in general focused on single mode power scaling, many applications exist that do not require the very high beam qualities of single mode fibre lasers [26,27]. This is seen within industry where the use of multimode beams from high power disk lasers have had wide adoption [28]. As has the common use of multimode delivery fibre for initially single mode sources [29]. Potentially very large gains can be had by moving from multimode delivery of a single mode source to generating the multimode beam directly within the active fibre. The movement to a multimode regime within the active fibre can relax the requirements on componentry such as fibre splices, reduce costs due to simplified fibre designs and the use of lower brightness pumps. This also allows significant increases in pulse energy and output powers in comparison to the single mode case. Both the current records for output pulse energy and CW output powers from fibre lasers are held by multimode architectures, at levels of 82mJ [30] and 100kW [31] respectively. Both well above their single mode counterparts.

However issues can arise when moving to multimode fibres. If the benefits of single mode fibre lasers, such as high pointing stability, are to be maintained care must be taken to manage the undesirable effects of modal interference within these multimode waveguides. When propagating through multimode fibre, interference occurs between guided modes and can lead to unstable output profiles [32–34]. For narrow band seed sources, the effects of modal interference are seen at the outputs of multimode fibres (Figure 4.18). Complex interference patterns between the guided modes define the beam profile. Changes in the relative phase between the modes due to fibre movement, stress or temperature fluctuations produce a constant change in the laser beam profile and beam pointing direction. This results in an unpredictable and unstable laser output, severely limiting the applicability of such sources.

One way to combat this problem is to employ a seed source with a coherence length shorter than the optical path difference of the excited modes [33]. In this case, rather than seeing the defined intensity profile of a narrowband modal interference pattern, the output profile is an incoherent combination of many interference patterns. The net result is an

output beam with a smooth, symmetrical profile, excellent pointing stability and a relative immunity to vibrations or temperature fluctuations.

4.3.2.1 Modal interference

Due to modal dispersion seen within multimode fibre, any initially in phase modes launched into a multimode fibre will experience a walk off between their relative phase. For monochromatic light the resultant intensity profile of these modes (due to coherent superposition) will evolve down the length of the fibre. Any fibre movement or temperature fluctuation within the fibre will lead to a change in the phase relationship between these modes. This change in phase is dependent on the relative overlap of the various modes within the core and cladding and behaves in very unpredictable ways. When applied to an optical fibre exposed to typical temperature fluctuations and movement, these phase changes result in an unstable intensity profile along the fibre length and at the fibre output.

For the case of two guided modes at the same wavelength, the interference of these modes can be described by the same interference equations used in the previous section. For the modal path length difference $\Delta = \Delta n_{eff} l$ we get:

$$I(\Delta) = I_1 + I_2 + 2\sqrt{I_1 I_2}\cos\left(\frac{2\pi\Delta n_{eff} l}{\lambda}\right) \tag{29}$$

This equation describes the periodic interference of the two guided modes. From this we can see that at a fixed l position a periodic interference occurs every time $\Delta n_{eff} l\,/\lambda = m$ (where m is an integer).

The spectral beat period of two modes at a fixed length is then given by:

$$\Delta\lambda_b = \lambda^{m+1} - \lambda^m = \frac{\Delta n_{eff} l}{m(m+1)} \tag{30}$$

Since typical values of interest are: $l{\sim}10m, \Delta n_{eff}{\sim}10^{-4}, \lambda{\sim}10^{-6}m \rightarrow m{\sim}1000$ i.e. m>>1. we can then simplify eq.(30) to:

$$\Delta\lambda_b \approx \frac{\Delta n_{eff} l}{m^2} \text{ (provided m} \gg 1) \approx \frac{\lambda_0^2}{\Delta n_{eff} l} \tag{31}$$

This beat period $\Delta\lambda_b$ defines the range of wavelengths over which one full cycle of modal interference occurs and beyond which the cycle begins to repeat. If we launch a range of wavelengths of equal spacing and intensity into a multimode optical fibre, with a total wavelength span greater than the spectral beat frequency, we can start to 'fill in' these modal interference patterns. This is because we are essentially sampling all the phase relationships of the modes and incoherently combining them. As the number of wavelength components increases within this comb so does the level of filling. Eventually the resultant profile is a smooth, stable sampling of all the intensity combinations of the modal interference. This is essentially the same as increasing the path length difference of an interferometer to greater than the coherence length of the source.

We can estimate the bandwidth required to effectively suppress the effects of modal beating between two modes within a step index fibre by first assuming that modal content is defined by the launch conditions and that the effects of mode coupling is minimal. Figure 4.6(a) plots an estimate of the required spectral bandwidth to suppress modal interference for a fixed fibre length and Figure 4.6(b) plots the estimated fibre length to suppress these effects for a fixed spectral bandwidth. Note: these calculations are based on a mean effective index separation between the guided modes of the fibre (as calculated using Optifibre mode solving software) and the propagation of only two modes; this is intended to highlight the trend of modal interference rather than model an actual fibre.

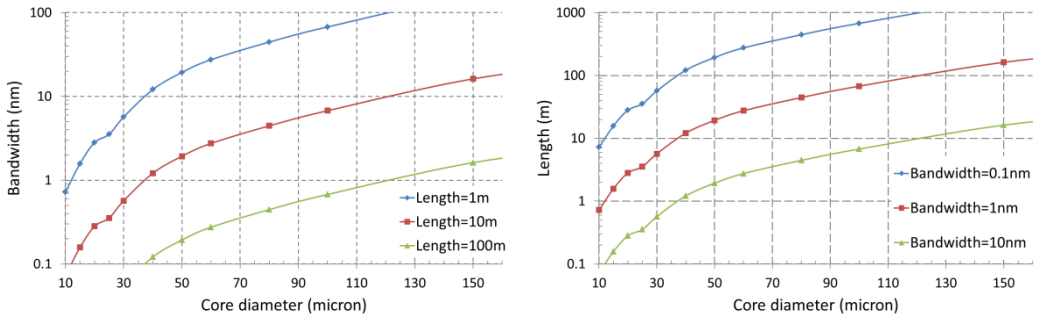

(a) (b)

Figure 4.6 (a) Behaviour of spectral beat period as core size is increased with fixed fibre lengths of 1, 10 & 100m. (b) Fibre length required to suppress the detrimental effects of modal interference for fixed spectral bandwidths of 0.1, 1, & 10nm. Core NA is 0.20.

Here we see the somewhat counterintuitive behaviour of the requirements of increasing bandwidth or fibre length to effectively suppress the effects of modal interference as core size is increased. This is explained as a result of the decreasing modal dispersion as fibre core size (V-number) is increased. The result is a requirement for longer distances or broader bandwidths to obtain the same optical path length difference.

If we now consider the behaviour of many mode excitation within the waveguide, we note a competing effect of this reduced modal dispersion. As core size is scaled the number of modes that can be guided also increases, and for intermediate V-numbers, the number of guided modes is roughly proportional to:

$$M \approx \frac{V^2}{4} \tag{32}$$

If we analyse a fully filled waveguide as core size is scaled, we note that the number of interference nodes (or speckle spots) increases as the number of guided modes [35]. As the fibre becomes more multimode the relative size of these spots must decrease. This behaviour is shown in Figure 4.7, where the propagation of a monochromatic light within fully filled fibres of increasing diameter is modelled (Rsoft BPM). Here we can see a decreasing in the asymmetry of the output profile for increasing fibre core size.

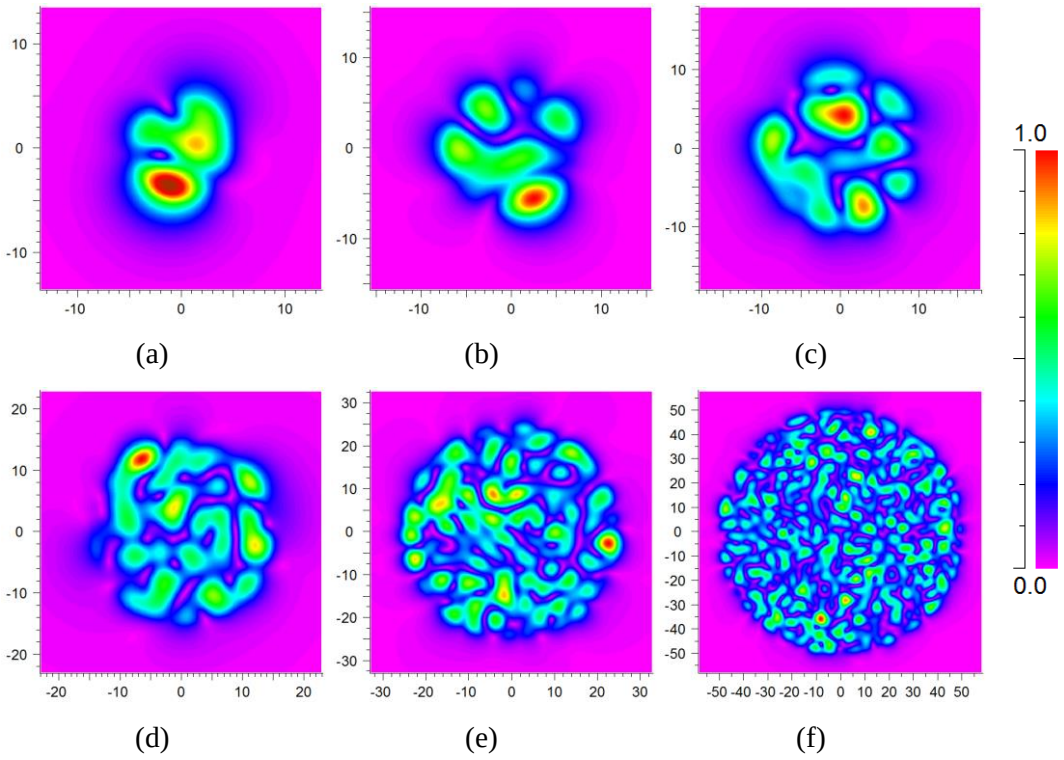

Figure 4.7. Output intensity profiles of fully filled multimode fibres with increasing core size and fixed NA (0.22), for core diameters and resulting V-numbers of: (a) 10µm, 4.6 (b) 15µm, 6.9 (c) 20µm, 9.2 (d) 30µm, 13.8 (e) 50µm, 23 (f) 100µm, 46.

As is demonstrated in Figure 4.7, the result of increasing the number of guided modes is a reduced sensitivity of the net 'centre of mass' of the guided modes to the relative position of the individual spots. For a low number of modes (Figure 4.7(a)), any change in phase relationship between the guided modes will result in drastic changes to the output beam profile. However, for increasing number of modes the relative intensities of the individual speckle spots has less of an effect on the resultant profile. Ultimately tending toward a top-hat profile matching the fibre core diameter (Figure 4.7(f)).

Experimental work

4.4 Thulium ASE source

We first investigate the output behaviour of a low power, feedback-suppressed, thulium ASE source. Here a simple all fibre configuration is constructed and demonstrates the typical behaviour of feedback suppressed ASE sources.

4.4.1 Experimental layout

See Figure 4.8, the cavity consisted of a 4m length of thulium-doped active fibre with 1wt.% thulium concentration. Fibre core and cladding dimensions were 6 and 100 µm, with numerical apertures of 0.22 and 0.46 for the core and cladding respectively. Pump light was provided by a fibre coupled 3W single emitter diode operating at a wavelength of 795nm. This was coupled into the active fibre through a 2+1 tapered fibre bundle (TFB). Due to a cladding diameter mismatch between the active fibre and TFB (125µm into 100 µm), an estimated 30% of pump light was lost in this coupling process. Output from the fibre source was taken from the single mode port of the TFB after a fibreised isolator. Within this configuration we opted for a flat cleave at the active fibre end opposite the fibre output. This choice was to allow the 4% back-reflection of any spontaneous emission, increasing the level and unidirectionality of emitted ASE light [36]. This 4% level of feedback, coupled with the feedback suppression of the fibre isolator, was found to be sufficiently low to prevent the onset of parasitic lasing at maximum pump power.

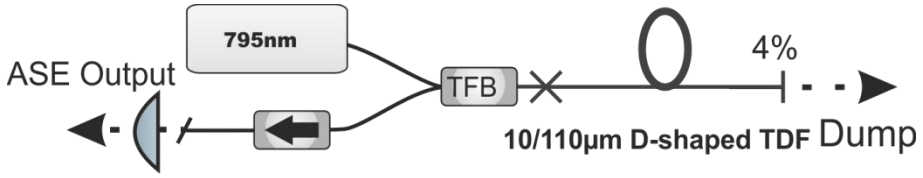

Figure 4.8 Cladding pumped all fibre ASE source in a feedback suppressed arrangement.

4.4.2 Results

Figure 4.9 shows the emitted spectrum of the fibre ASE source for increasing output powers. The central wavelength of this source was 1950nm. At a pump power of 0.3W, a spectral bandwidth of 140nm was obtained, at this pump level the total signal output power was 2µW. Although output power increased rapidly as pump power was increased, gain narrowing of the source reduced the spectral bandwidth by an order of magnitude. At a maximum pump power of 2.1W, 34mW was obtained from the source with a spectral bandwidth of 31nm. At this pump power > 1µW/nm was seen from 1890-2038nm.

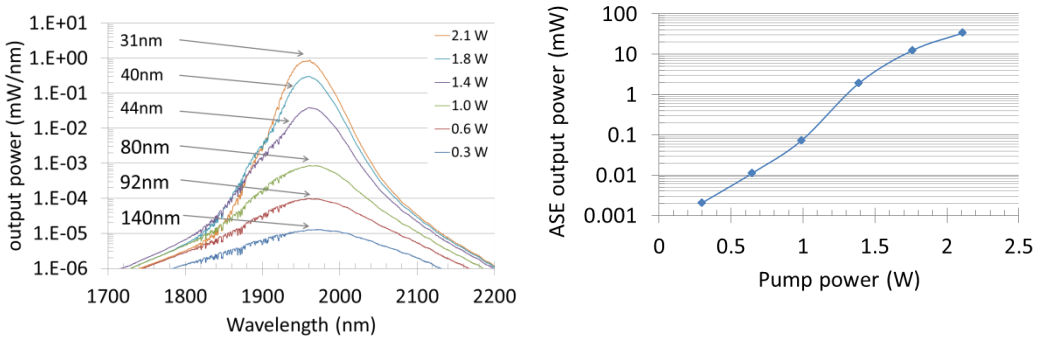

(a) (b)

Figure 4.9 (a) ASE source output spectrum for increasing pump power. (b) Corresponding signal output power

Although the power levels of this source were modest, it does demonstrate the playoffs that must be made between output power and spectral bandwidth in typical ASE sources, particularly when relying on the intrinsic wavelength selection of a passive cavity.

4.5 Bandwidth controllable pulsed ASE source

In an approach similar to that used in [16] we introduce a wavelength selective feedback cavity to the ASE source. However, rather than using a feedback suppressed source we apply this to a Q-switched cavity. Within this cavity we use an acousto-optic modulator (AOM) as a Q-switching element and a diffraction grating and HR mirror arrangement as the spectral control element. This allows a robust ASE generation whilst also allowing strong spectral control.

4.5.1 Experimental layout

A source was constructed from a thulium-doped fibre, with 0.2 wt.% Tm concentration, 0.13NA and a 10 µm core diameter. This active fibre was core pumped by a 1565nm Er,Yb fibre laser source with pump light being coupled into the active fibre via a fused fibre wavelength division multiplexer (WDM). Cavity feedback and output coupling was provided by the ~4% Fresnel reflection from a perpendicularly cleaved fibre end facet. At the opposite end, feedback was provided by an external cavity containing a TeO_2 AOM and a diffraction grating. The AOM has a rise time of 100ns and a drive frequency of 111MHz (corresponding to a 222MHz round trip frequency shift for oscillating light).

The external cavity was aligned so that the first order diffracted beam was incident on the grating. The resulting beam diffracted from the grating was then focused through a variable width slit onto a highly reflecting mirror, see Figure 4.10. By adjusting the position of the slit in front of the HR mirror the mean oscillating wavelength of the cavity could be controlled, and by adjusting the width of this slit the spectral bandwidth of this oscillating light could also be controlled.

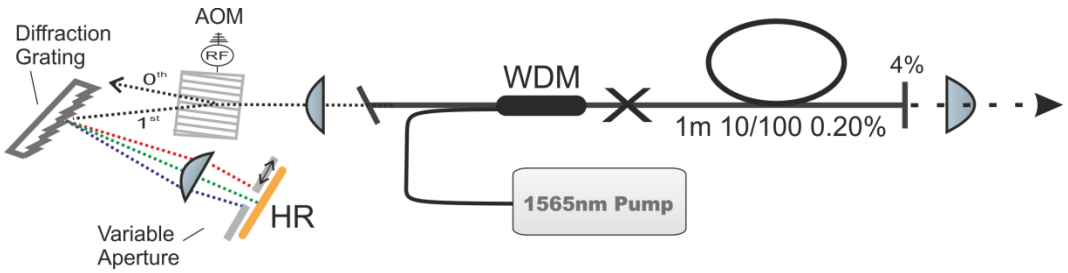

Figure 4.10 Experimental layout of the Q-switched ASE source, with an external cavity containing an acousto-optic modulator (AOM), diffraction grating and variable aperture slit.

4.5.2 Results

We first operated the AO Q-switch in a time gated regime to allow the investigation of the time scales associated with various cavity dynamics, such as the onset of lasing etc. This also allowed confirmation that we are indeed operating in an ASE regime for the initial pulsed output. At a launched pump power of approximately 2W the external cavity AOM was operated at a repetition rate of 1kHz with an on duration of 0.96ms. Gate width and repetition rate were chosen to allow sufficient time for steady state behaviour to become established within the cavity, as well as allowing sufficient 'off' time to ensure the cavity started from noise. Using a fast photodiode and oscilloscope a time trace was recorded and the point at which gate opening occurred was set as zero. Figure 4.11 shows the behaviour of a single turn on event, with the x-axis being expressed in number of cavity round trips for clarity. From this trace we can see that an initial pulse is extracted within ~4 round trips (140ns) of oscillating light. Only after ~760 round trips (~27μs) do other cavity dynamics start to become apparent. With at first, large hybrid Q-switched mode-locking pulses and after ~2500 round trips (~87μs) more stable mode-locking becomes established. This mode-locking is a result of a round trip frequency shift imparted by the AOM [37]. It can be seen from the below trace that the initial pulse appears to be distinct from the other two modes of operation, happening within a very

short number of cavity round trips. This remarkably fast build-up time of the initial pulse further suggests that it is indeed seeded from pre-existing ASE built-up within the cavity in the off state. Given this small number of round trips it is not expected that longitudinal mode formation has time to become established within the initial pulse. Note: Due to the limited dynamic range of the measurement system, it was necessary to operate the photodiode in the saturated regime for the initial Q-switch pulse to allow measurement of the lower power dynamics, Insert (a) of Figure 4.11 was recorded in addition to the initial trace after signal attenuation.

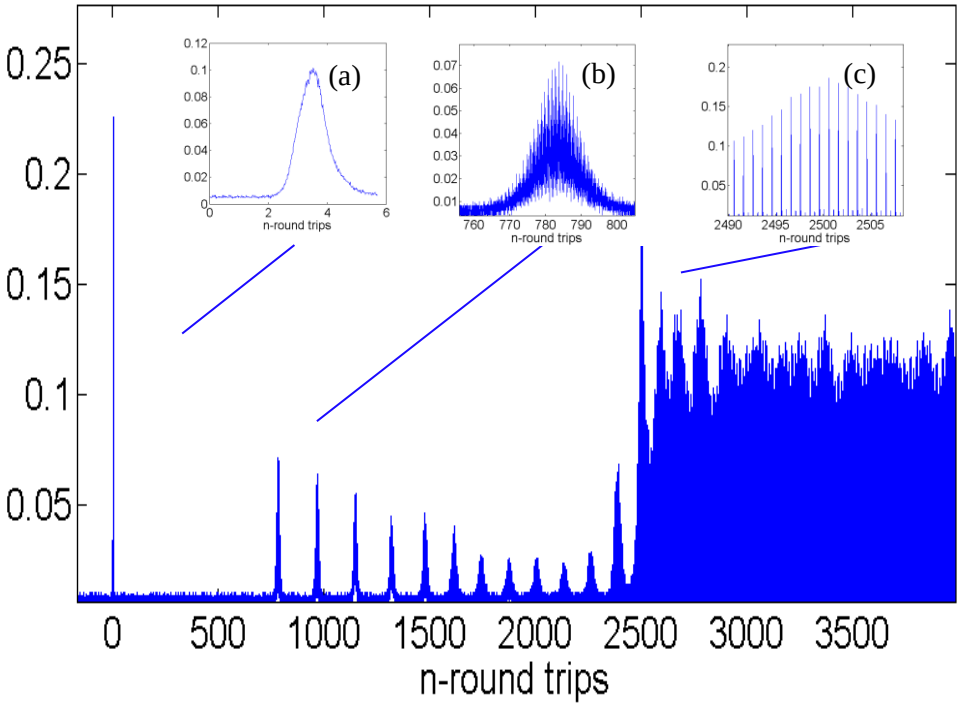

Figure 4.11 A typical oscilloscope trace demonstrating turn-on dynamics when operating the cavity in gated mode. Insert (a) shows the initial Q-switch pulse formation and extraction within several cavity round trips, Insert (b) demonstrates the initial onset of Q-switched mode-locking and Insert (c) shows the cavity operating in a more steady state behaviour.

With the AO drive signal optimised for Q-switched mode of operation and the centre wavelength of the variable slit adjusted to the fibre gain peak of 1850nm, the source produced 10.3W of broadband output. At a repetition rate of 500 kHz and launched pump power of 18.2W, with a corresponding pulse duration of 95ns. A maximum peak power was obtained at a pulse repetition rate of 125 kHz, with up to 7.9 W of output power obtained within smooth 29 ns broadband pulses; the resultant peak power was in excess

of 2kW (see Figure 4.12(b)). At this repetition rate, and with a fully open slit width of 6mm, spectral emission was seen from 1800nm to 1900nm with a FWHM spectral bandwidth of 24nm. No evidence of the sharply modulated spectral structure, normally associated with fibre laser operation, was seen. The fine structure that can be seen within the spectral traces (Figure 4.13(a)) are a result of the atmospheric OH absorption features prominent within the 1800-1900nm wavelength range [38]. To characterise the level of CW background within the Q-switched output, a 4% pickoff was taken from the laser output and was incident on a second acousto-optic modulator. This second AOM was used to time gate the optical pulse, allowing the relative power contained with the pulse (in comparison to CW background) to be measured. This measurement confirmed a greater than 20dB signal-to-noise level at a pulse repetition rate of 125kHz. i.e. >99% of power is contained within the ASE pulse. Pulse-to-pulse stability was measured using a fast photodiode and analysed using the pulse area function of a Tektronix oscilloscope. With a sample size of n >2000 the standard deviation of pulse-to-pulse energy fluctuation was found to be approximately 0.25%.

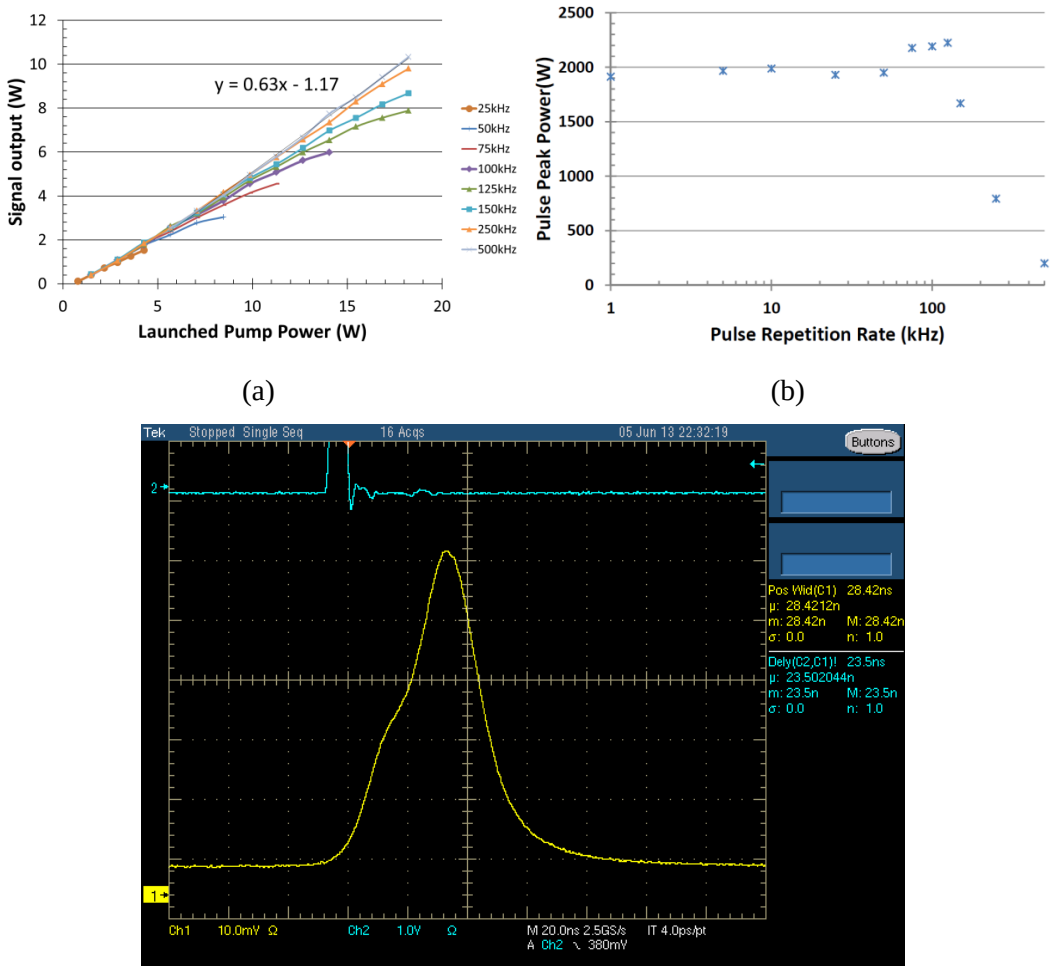

Figure 4.12 (a) Source output power vs. launched pump power demonstrating a slope efficiency of 63% prior to rollover. (b) The maximum peak power obtained vs. pulse repetition rate demonstrating an approximately constant peak power for repetition rates below 125kHz, at pulse frequencies above this a linear decay in peak power is seen due to limited pump power. (c) a typical output pulse profile for a pulse repetition rate of 100kHz and pump power of ~15W.

The roll-over in output power seen in Figure 4.12(a) at lower pulse repetition rates is a result of CW ASE clamping the output pulse energy of the cavity. As the repetition rate of the laser is reduced, the longer 'off' time between cavity pulses eventually allows sufficient CW ASE to build-up between the Q-switched pulse output, and begins to extract cavity inversion. Eventually as pump power is further increased beyond this rollover point parasitic lasing can occur. This is directed towards the 0^{th} order dumped beam of the AOM. When operating in a parasitic lasing regime, the output showed

marked change in pulse shape and spectrum, with unstable multi-pulse behaviour in the time domain and strong spectral narrowing and spiking occurring.

By reducing the slit width within the external cavity, the oscillating bandwidth could be continually reduced from 24nm down to 0.75 nm (Figure 4.13(a)) before a significant drop in power was observed (Figure 4.13(b)). Within this range of spectral bandwidths pulse energy and peak powers maintained approximately constant values, with only the expected increase spectral power density for reduced spectral bandwidths. For linewidths below ~0.75nm the limited resolving power of the diffraction grating meant that attenuation as well as wavelength narrowing occurred for any further reductions in the slit width. By translating the slit position within the external cavity, it was also possible to tune the centre wavelength of the source from 1785nm through to 1935nm.

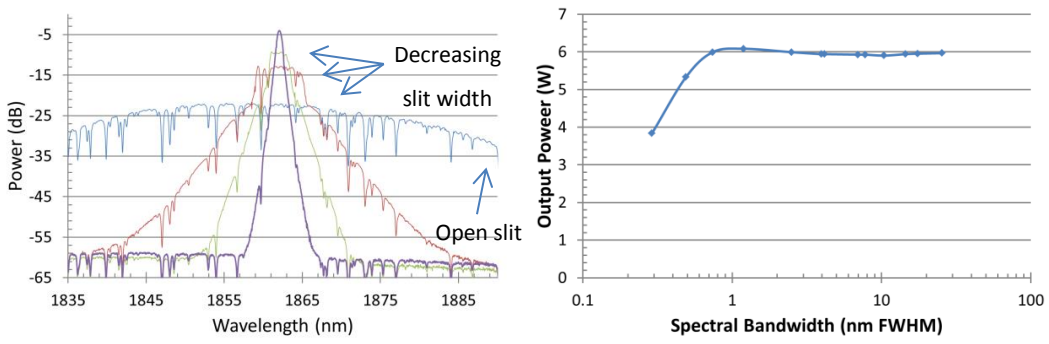

(a) (b)

Figure 4.13 (a) Laser output spectrum for varying slit width. (b) Laser output power for varying output bandwidth.

The temporal behaviour of the individual wavelength components of the broadband ASE pulses was further investigated through the use of volume Bragg grating (λ_0=1932nm, $\Delta\lambda$=0.5nm) as a wavelength filter. The output of the Q-switched source was directed through the VBG, and was used to filter 0.5nm spectral slices from the broad bandwidth output pulse. The narrowband spectral slices were then incident on a fast photodiode, with angle tuning used to scan across the wavelength range of the output pulse. Across this range no evidence of wavelength dependent delay or chirp was observed within the time resolution of the measurements. The individual wavelength slices did however demonstrate a higher level of modulation of pulse shape in comparison to the unfiltered pulse, with the cause of this behaviour is still under investigation. The original smooth

pulse envelope was recovered when several wavelength slices were superimposed in post processing.

4.6 Applications

Within this section, we will detail two experiments utilising the relatively high peak power and broad spectral control of this pulsed ASE source. Firstly this source is used as a seed to initiate supercontinuum generation, increasing the spectral coverage to greater than an octave; this broadband supercontinuum source is then applied to OCT. The second half of this applications section will focus on the suppression of modal interference within a multimode amplifier, here we take advantage of the spectral control of the ASE source. Using this as a seed to characterise and ultimately suppress the detrimental effects of modal interference.

4.6.1 ASE seeded supercontinuum generation

As the coherence length of the white light source limits the spatial resolution achieved within an OCT system it is advantageous to maximise the spectral bandwidth of this source. Here we push beyond the gain bandwidth of the Tm-doped fibre by taking advantage of the high peak power of the pulsed ASE source to generate broadband ASE seeded supercontinuum (SC) light. The single mode output from the pulsed ASE source was directly spliced to a 5m length of small-core germanium-doped, highly nonlinear fibre (HNLF) and was used as a seed source for continuum generation. This HNLF was fabricated by Fibercore, having a 3.8μm germanium doped core and NA of 0.29. The fibre was single mode at the seed wavelength, with a single mode cut-off at 1400nm. The calculated zero dispersion wavelength of this fibre was 1550nm. The mode field diameter was calculated (Optifibre) to be 5.0μm at the seed wavelength of 1850nm.

Initially several different arrangements were trialled to allow the coupling of the free space output from the pulsed ASE source to the small core germanium-doped fibre. The difficulty arose in trying to maintain optical feedback to the Q-switched source whilst also allowing coupling in to the HNLF. As feedback to the Q-switched seed relies on the 4% Fresnel reflection from the flat cleaved fibre output, simply splicing on to the GDF was not a viable option. Free space launching was considered non-ideal due to the difficulty in reliably packaging such an arrangement. A mating arrangement consisting of

two flat cleaves was trialled but ruled out due to etalon effects between the flat cleaves interfering with the seed spectrum. A second mating arrangement was developed consisting of a flat cleave for source feedback and a butted angle cleave to allow core coupling. This simple mating arrangement proved successful, however did introduce a 2dB (~39%) insertion loss into the SMF. Ultimately it was found that back-reflection from an optical isolator spliced directly to the pulsed source provided sufficient feedback for stable pulsing to occur. The power penalty of this arrangement was approximately 12.5% including isolator losses when coupling to SMF28. Due to the large mode field diameter (MFD) mismatch between the SMF28e output from the isolator (12.5µm MFD) and the HNLF (5.0µm MFD) an initially high splice loss of >40% was seen between these two fibres. Through splice optimisation using long duration diffusion splicing, we reduced this value to 26%, resulting in a maximum peak power of 1.13kW launched into the HNLF with this arrangement. This corresponded to a total launched seed power of 4W (at a pulse repetition rate of 50kHz). The limited power handling capability of the isolator placed an upper limit on the average power level coupled into the HNLF. The experimental layout of this supercontinuum source is shown in Figure 4.14.

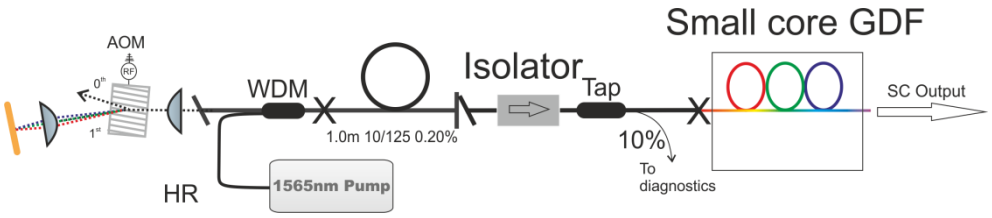

Figure 4.14 Experimental layout of the ASE seeded supercontinuum source, with an all fibreised coupling arrangement.

4.6.1.1 Results

At a 50kHz pulse repetition rate and 1.13kW of launched peak power (40ns pulse width), the HNLF produced a supercontinuum output ranging from 1000nm through to 2450nm as measured with the aid of two spectrum analysers (Figure 4.15). The bulk of the continuum generation occurred at wavelengths longer that than the 1850nm seed. For 4W of launched seed power 1.5W of supercontinuum output was generated, with a spectral power density of > 1.5mW/nm over a 650nm wavelength range from ~1750-2400nm. From 1900-2350nm the source showed excellent flatness with a spectral ripple of only ~1dB. We investigated the effects of seed linewidth on the generated supercontinuum and

found a maximum emission at a narrow seed linewidth of ~1.65nm, this also corresponded to an enhanced low-level visible generation seen across the fibre length. A comparison of the generated supercontinuum for broadband and narrowband seeds is shown in Figure 4.15. The red coloured spectrum denotes the narrowband (1.65nm) seed and blue denotes the broadband (>24nm FWHM) seed.

An important parameter of the usefulness of this source for OCT application is the level of pulse-to-pulse spectral fluctuation. We measured the spectrally dependent pulse-to-pulse energy variations of this supercontinuum source through use of a high-resolution monochromator and fast photodiode. A small area InGaAs photodiode with temporal bandwidth of 50MHz was used for the pulse-to-pulse stability measurements, and allowed the direct measurement of spectrally dependent pulse-to-pulse fluctuations. A spectral selectivity of ~3nm was obtained with the monochromator and detector arrangement. This slightly low resolution was chosen to ensure sufficient signal was incident on the fast photodiode. The pulse energy variance of the SC source was measured from 1100nm to 2500nm. Figure 4.15 shows the pulse energy variance (2σ or 95% confidence) across the supercontinuum emission range. For the broadband seed we can see that the majority of pulses fall within 3% of the signal average from 1200-2400nm, this value increased slightly for the narrowband seed but still stayed within 4% of the mean.

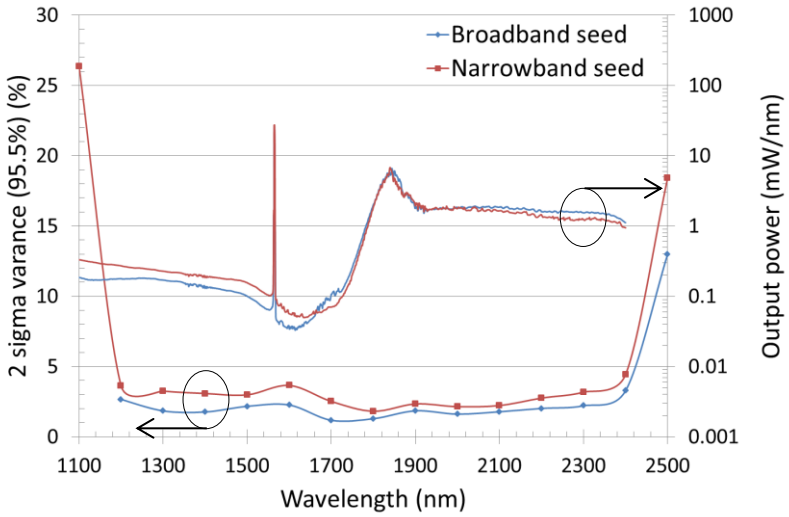

Figure 4.15 (Left Axis) Measurements of the spectrally dependent pulse-to-pulse energy variance (2σ) taken with a spectral resolution of 3nm FWHM. (Right axis) Generated supercontinuum at the maximum launched seed peak power of 1.52kW detailing the difference in spectra for broadband seed (>24nm FWHM) and narrowband seed (1.65nm FWHM).

In Figure 4.16 we plot the spectral evolution of the supercontinuum for increasing seed peak power. On top of this is the calculated group delay (Optifibre) for the first two guided modes of this fibre. Here we can see the smooth generation of broadband light from 1000nm to 2400nm with the spectral evolution closely matching the predicted group delay.

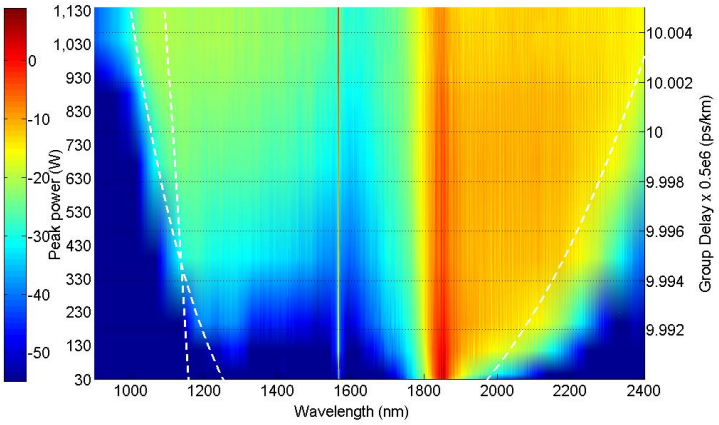

Figure 4.16 Spectrogram detailing the fibre supercontinuum evolution as seed peak power is increased to a maximum value of 1.13kW (1.52kW launched), overlaid on this is the predicted fibre group delay for the first two guided modes, colour variance of the plot expresses spectral intensity in dB. Note: interpolation was utilised between peak power measurements on this graph to aid the eye.

4.6.1.2 Discussion

Due to the relatively long pulse widths as well as the pump wavelength being within the anomalous dispersion regime it is expected that this continuum generation in initiated by the onset of modulation instability within the HNLF [39]. Here a pulse break-up of the initial 30ns pulse into a large number of solitons occurs and can explain the relatively smooth spectra and high pulse to pulse stability. Although the formation of a single soliton in this picture is highly unpredictable. The relatively long pulse width of the pump in comparison to the modulation instability period of the fibre (of the order of 1ps) results in a very large number of solitons being formed within the pulse envelope. Here due to statistical averaging, the result is stable supercontinuum generation within the pulse envelope.

In the above experiment we observed a dependence of the seed spectral bandwidth on the level of continuum generation. When scanning through spectral bandwidths (from a maximum of >24nm down to 0.3nm) we found a peak in continuum generation at a bandwidth of approximately 1.65nm. This corresponded with a maximum in the visible light emission from the HNLF as well as a slight increase in long wavelength emission. This dependence of continuum generation on the pump spectral bandwidth is consistent

with results reported elsewhere [40], and is explained by a matching of the pump coherence time with the modulation instability period of the fibre. Here the fluctuations in spectral beating within the pump match the period of modulation instability and lead to an enhancement of its effects. The result is an increase in the number of high peak power solitons forming and an increase in generated bandwidth. It is expected that this should also come at the cost of increased fluctuations within the generated continuum in comparison to the broadband seed, where such enhancements are not expected to be significant. Whilst we did measure an increase in the pulse-to-pulse fluctuations for the narrow band seed, only limited conclusions can be made from this. Measurements of the pulse-to-pulse energy fluctuations of the initial seed prior to launch into the HNLF found an increased fluctuation for the narrow band seed in comparison to the broadband seed (2σ=0.31% for broadband and 2σ=0.77% for narrowband seed).

Longer-term stability measurements were conducted on this source through the comparison of several spectral measurements taken at half-hour intervals (using an optical spectrum analyser (OSA)). With the generated spectral shape compared across an hour-long timescale we found an approximately 5% (+/- 2.5%) variation in spectral shape. These variations are suspected to be a result of temperature drift of external cavity components within the pulsed ASE seed. By moving to an all fiberized ASE seed it is expected that the source stability can be increased in the future.

In terms of the intended application as a light engine for OCT systems, there are several potential advantages to lower repetition rate high pulse energy SC generation in comparison to the commercially available options operating at repetition rates in the 4-80MHz range (with pico or femtosecond pulse widths). At these relatively low repetition rates it is a viable option to implement a lock-in (or time gated) detection scheme. Here as the pulse is operating with a ~-40dB duty cycle, a time gated detection scheme can effectively reduce the average power requirements for the OCT system by several orders of magnitude whilst still maintaining a reasonable signal to noise ratio. Although this is also technically possible with higher pulse frequencies, the shorter pulse widths become more challenging to effectively time gate and require high cost, high bandwidth detection schemes.

4.6.1.3 Long wavelength OCT analysis of paint pigment samples

(Note: These results were taken in collaboration with Dr. Masaki Tokurakawa and our project partners at Nottingham Trent University (NTU), Dr. Haida Liang and Dr Chi Shing Cheung.)

Initial tests of the coherence length of this broadband source were conducted through the use of a time domain OCT system constructed by NTU. The experimental layout of this system consisted of a broadband 50:50 2000nm fused fibre coupler to split the SC light towards a reference arm (containing a collimation lens and retroreflective mirror mounted on a motorised translation stage) and sample arm (containing a collimation optic and galvo scanner). Samples were mounted onto microscope slides and then interrogated using this system. The back-reflected light from both the sample and reference arms were interfered via the 50:50 coupler and incident on a balanced detection and data acquisition scheme.

Using this supercontinuum source, after first spectrally filtering out the short wavelength components using a Ge filter, measurements were made with a blank microscope cover slip (silica). The initial results of this are shown in Figure 4.17 here we can see a clear interferogram from the air-glass interface. The FWHM of this interference fringes is approximately 10μm and represents the spatial impulse response of the system (limited by the wavelength sensitivity of the balanced detector).

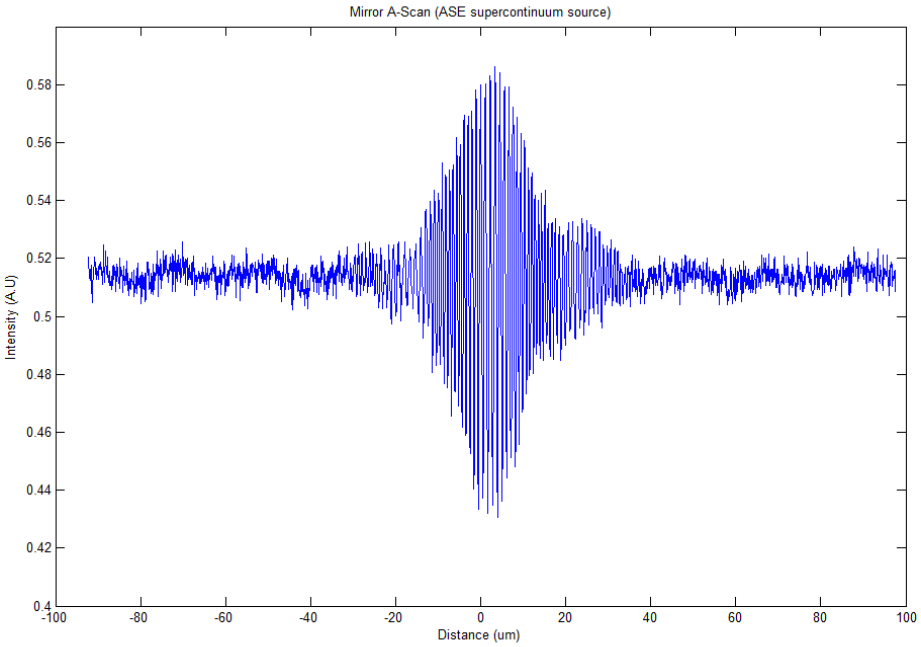

Figure 4.17 OCT depth scan of fused silica microscope cover slip detailing the air glass reflection with spatial resolution of ~10µm.

A second packaged and portable version of this supercontinuum source has been constructed by Dr. Masaki Tokurakawa and is currently with NTU for further research.

Initial results taken by NTU using a long wavelength ASE source (Section 4.4) are promising. Figure 4.18 shows typical line scan ('B-scan') results taken with 930nm & 1950nm light sources. Here a microscope slide painted with titanium white oil paint is interrogated. Figure 4.18(b) shows the results obtained with 930nm light, excess scattering caused by the Ti:white sample at 930nm as well as strong absorption lead to poor image quality with low contrast. By moving to longer wavelengths (Figure 4.18(b)) there is a clear improvement in image contrast. Here the paint layer (of ~100µm) is easily visible, as is the bottom layer of the microscope slide. Note: the 1950nm source used in this work was a packaged version of the ASE source detailed in Section 4.4. This was constructed by Dr. Tokurakawa and myself.

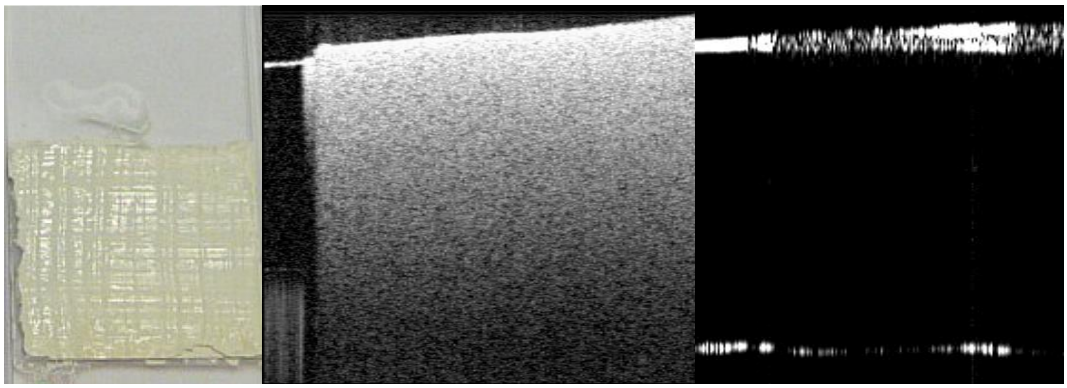

(a) (b) (c)

Figure 4.18 An example of the contrast enhancement obtained by moving from short wavelength OCT (930nm) to long wavelength OCT (1950nm). (a) Shows the sample under test consisting of a microscope slide with top surface painted with titanium white oil paint. (b) Shows OCT measurement taken with 930nm white light source and (c) shows the same sample taken with 1950nm ASE source [41].

4.6.2 Power scaling and suppression of modal interference in multimode fibre amplifiers

As discussed previously, there can be an advantage in moving to multimode fibre amplification schemes. These advantages include increased energy storage and higher thresholds for detrimental nonlinear processes. However, this movement into a multimode propagation regime can also introduce problems associated with modal interference and pointing instability effects. In this section we experimentally explore these effects through the use of a multimode fibre amplifier seeded by the single-mode variable bandwidth seed source (Section 4.5).

4.6.2.1 Experimental arrangement

As detailed in Figure 4.19, a multimode power amplifier was constructed using a 18 µm core-diameter thulium doped double-clad fibre with a Tm concentration of 3.5 wt.% and core NA of 0.22. This resulted in a fibre V-number of ~6 corresponding to 6 guided LP modes. The inner-cladding was D-shaped with an outer dimension of 200µm. A 200µm coreless fibre endcap (of 500µm length) was fusion spliced to both ends of the amplifier to suppress Fresnel back-reflections as well as mitigate any potential optical damage at the fibre endface. Pump light for the amplifier was provided by a 795nm fibre coupled diode source with a maximum power of 50W, launched into the active fibre in a counter-

propagating pump arrangement. The seed for this amplifier was provided by the previously discussed pulsed ASE source. After isolation the seed source was free-space launched into the multimode power amplifier in an NA filling launch arrangement. The choice of NA filling rather than mode matching of this fibre was taken in order to excite the largest number of modes whilst still maintaining reasonable coupling efficiency. Active alignment of the seed source coupling was performed to maximize output power. Optimum output power generally occurred in a slightly off axis launch arrangement. Output from the amplifier was taken from a dichroic mirror orientated at 45°, providing high reflectivity in the 1800-2100nm wavelength range and high transmission in the 795nm wavelength range. A 4% pick-off wedge directed to both a pyroelectric array camera and a scanning slit beam profiler with 200mm focal length lens provided beam diagnostics. A thermal power meter was used to measure output power.

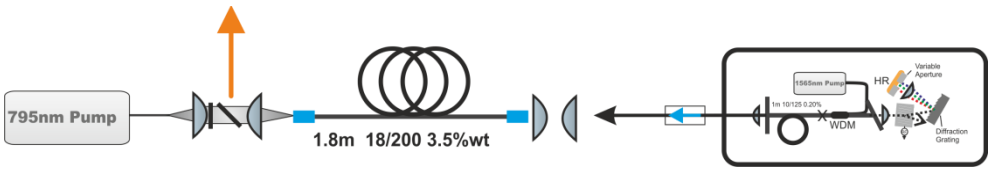

Figure 4.19 The experimental layout of the multimode MOPA system used for the investigation into multimode interference.

4.6.2.2 Results

Figure 4.20(a) shows the amplifier output power as a function of pump power. At a pulsed repetition rate of 100kHz and approximately 1W of launched seed power, 22.2W of amplified signal was achieved for the broadband signal and 20.9W for narrowband signal. Both obtained at a launched pump power of 42.3W (pump power limited) with corresponding slope efficiencies of 54% and 51% respectively.

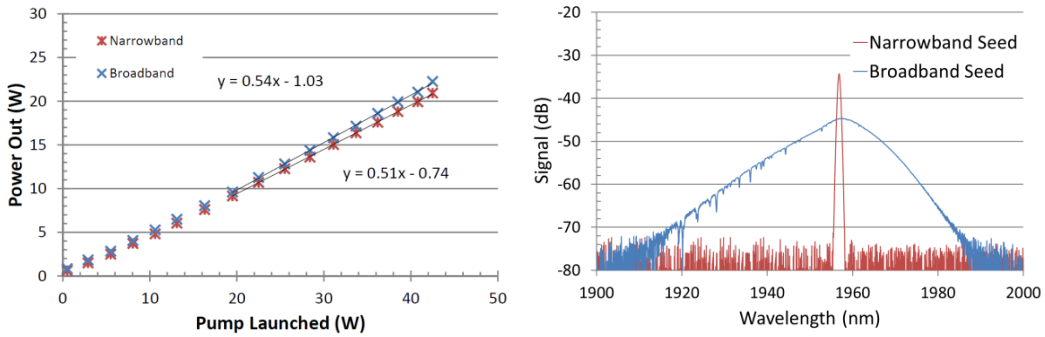

(a) (b)

Figure 4.20 (a) Laser slope efficiencies and (b) spectral bandwidth for narrow and broadband seed operation.

By increasing the spectral bandwidth of the seed source it was possible to transfer the laser output from a regime where modal interference effects were prominent (narrowband seed) to a regime where the modal interference effects were suppressed (broadband seed). With fixed launch conditions we adjusted the bandwidth of the seed source from 0.30 nm to 13 nm FWHM (see Figure 4.20(b)). Output beam profiles for increasing spectral bandwidth are shown in Figure 4.21.

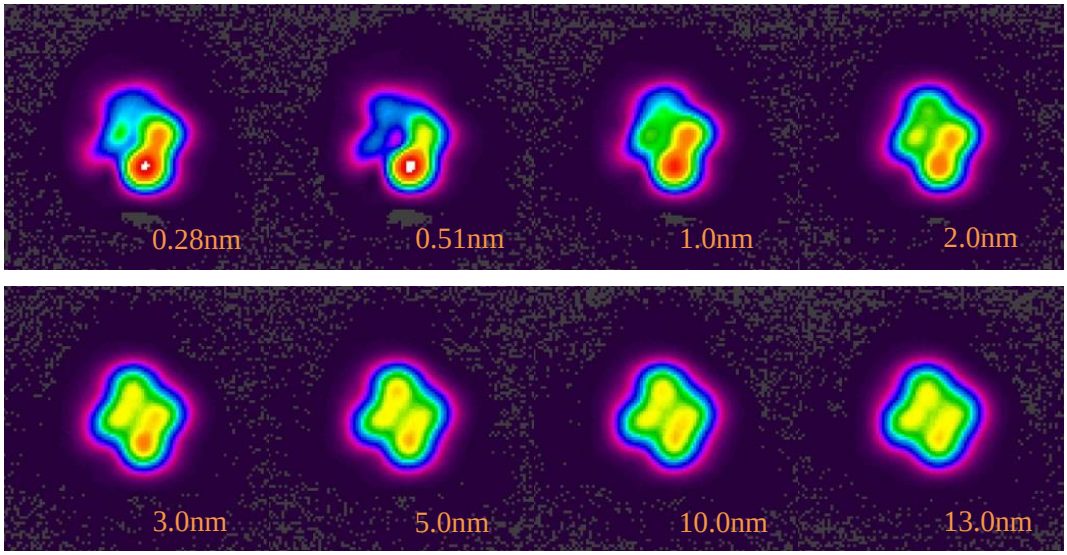

Figure 4.21 Sequence of laser beam profiles at multimode amplifier output for increasing seed bandwidth. (Top left) shows the uneven and unstable intensity distribution when operating with a 0.28nm seed bandwidth. (Bottom right) shows the smoothed output profile when operating with a broadband seed of 13nm.

For narrowband seeding (sub 1nm) the beam profile shows sharp features that were sensitive to fibre movement and unstable in the time domain. Progressively increasing

the seed from 1nm to 13nm resulted in a more symmetric beam that was less sensitive to fibre movement. Above a value of ~3nm only minimal profile change was observed for further increasing bandwidth. For bandwidths greater than ~3nm the fibre maintained a stable profile even when the active fibre was perturbed. At full pump power the beam propagation factor (M^2) was measured for both broadband and narrowband seeding and was found to be to be M_x^2=2.7 by M_y^2=2.9 in both cases.

At a pulse repetition rate of 100kHz a maximum pulse energy of 200µJ was obtained with a pulse width of 50ns, corresponding to a peak power of 5kW. By reducing the pulse repetition rate it was possible to increase the pulse energy to 1.1mJ corresponding peak power above 20kW. However, this was at the expense of signal-to-noise ratio (as measured using a time gated AOM technique), with only 50% of output power contained within the pulse (Figure 4.22).

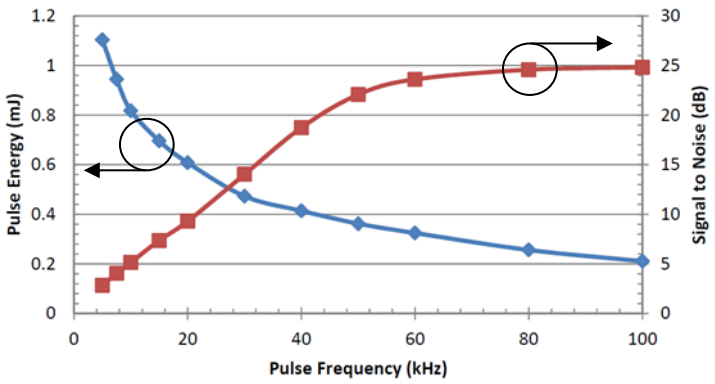

Figure 4.22 (Left axis) laser output pulse energy vs. pulse repetition rate. (Right axis) corresponding signal to noise measurement.

Whilst perturbing the active fibre the output beam profile was measured and recorded using a high accuracy scanning slit beam profiler (Nanoscan). Beam diameter and centre of mass position were recorded for >500 samples for both the narrowband and broadband seeds. Figure 4.23 shows the deviation of the centre of mass of the beam from their mean position, with beam deviation normalised against beam waist in both X and Y-axis. For the case of narrowband seed input, the beam showed a maximum deviation from mean of 11.8% of beam waist with a maximum total deviation of >20%. However with all launch conditions fixed when propagating with a broadband seed the stability of the beam increased considerably, now with a maximum deviation of only 2%.

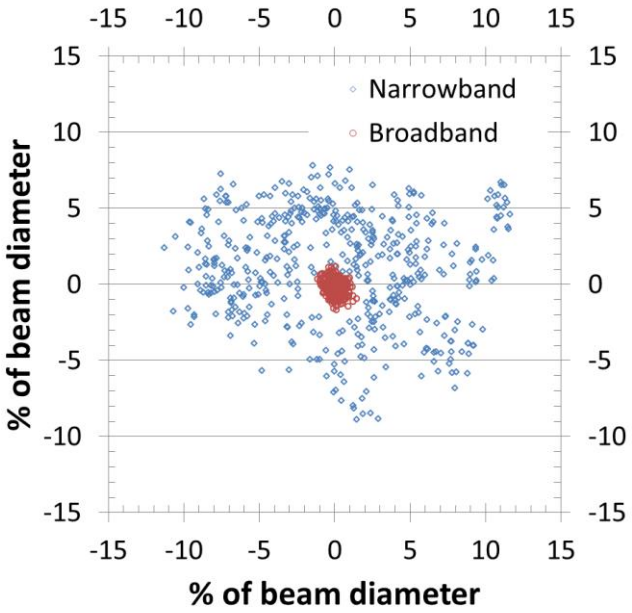

Figure 4.23 Laser pointing stability for the case of narrowband and broadband seed inputs expressed as a % deviation from mean beam potion.

This dramatic reduction in beam movement when operating with a broadband seed demonstrates the effective suppression of the detrimental effects of modal interference through bandwidth tailoring. This large improvement in beam stability greatly enhances the usefulness of this source. This is particularly true for cutting or marking applications, where any movement of beam profile will lead to degradation of process quality.

As an investigation into further core size scaling of both passive beam delivery and active fibre amplification, a multimode passive fibre, with 50/125 µm core and cladding diameters and step index profile (0.22NA), was used to propagate the pulsed ASE seed a distance of 10m. The single mode output of the seed source was offset spliced directly to the multimode passive fibre. This was then wrapped around a rectangular bar several times to increase the number of excited modes. A weight tied to a rotating wheel driven in a circular motion was attached to a section of the passive fibre. This allowed the repeatable movement of the fibre, enabling comparisons between the different seed bandwidths. Using the pyroelectric array camera, the output of this passive fibre was recorded for both the broadband (Figure 4.24(a)) and narrowband (Figure 4.24(b)) cases.

Again, as expected, the case of narrowband signal propagation within multimode fibre demonstrated sharp features with a large intensity variation across the fibre core. When

the passive fibre was perturbed, rapid movement of the intensity profile occurred. While, with fixed launch conditions, increasing the seed bandwidth led to a much more top hat like intensity profile, although still showing intensity fluctuations with fibre movement, the range of these fluctuations was reduced substantially in comparison to the narrowband case.

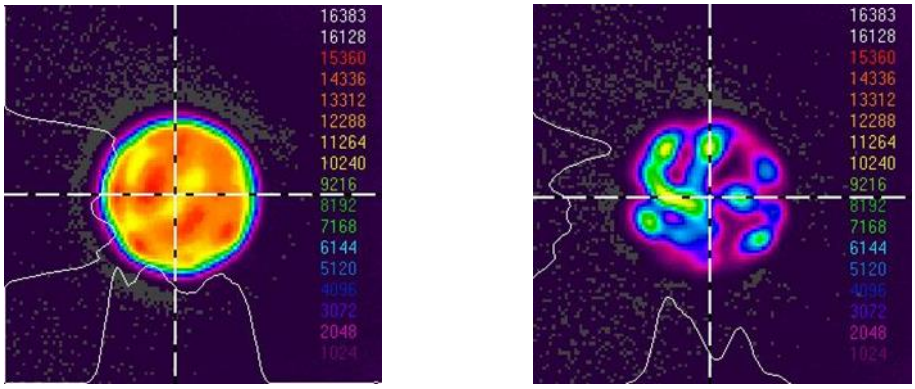

(a) (b)

Figure 4.24 Output profiles from 50/125µm 0.22NA step index passive fibre, for Broadband light propagation (a) and narrowband propagation (b).

4.7 Conclusion

In conclusion, by utilising the extremely fast pulse build-up times associated with pulsed fibre lasers we have demonstrated the ability to generate high power, both average and peak, ASE light. Through the use of external cavity spectral filtering, we have demonstrated the ability to spectrally tailor a pulsed ASE source with a high degree of control. This control is achieved not only in operating wavelength but also in spectral bandwidth and spectral power density. Showing the ability to select operating wavelength over a 150nm range from 1785nm to 1935nm and operating bandwidth over a > 20nm range from 24nm down to 0.3nm. The resulting variation in coherence length was from ~5mm down to ~60 microns. We also demonstrate ASE pulses with greater than 2kW peak power within 29ns pulsewidths at a repetition rate of 125kHz. By increasing the pulse repetition rate to 500kHz over 10W of output power was obtained for 18.2W of launched pump, corresponding to a slope efficiency of 63%. The pulse-to-pulse stability of this source was found to be excellent, with a measured 2σ value of 0.5% for pulse energy. Although we have initially demonstrated simple spectral control, by implementing a more sophisticated wavelength control of the external cavity (such as

through the use of a diffraction grating and digital micromirror device (DMD)) it should be possible to produce a wide range of novel spectral shapes, such as flat toped or other desired profiles. The high degree of flexibility of this source should prove useful for spectral characterisation and sensing as well as a promising seed for further amplification in both single-mode and multi-mode systems.

Through the use of low cost, widely available, highly nonlinear fibre we have produced a simple addition to this pulsed ASE source that allows the expansion of wavelength coverage to many times greater than that of the thulium gain band. Successfully extending the spectral coverage of this source to greater than an octave, beginning at 1000nm and extending to beyond 2400nm. Over 1.5mW/nm spectral power was achieved within the 1800-2400nm wavelength range. This source was characterised for long-term stability through repeated spectral envelope measurements, and short-term stability through spectrally dependent pulse-to-pulse measurements. Both measurements found less than 5% variance of the spectral components. The high levels of pulse-to-pulse stability are a result of both the relatively long pulse durations of the seed source as well as the excellent temporal stability of the ASE seed. Although currently limited by the power handling capability of the available fibre isolator, power scaling of this supercontinuum source is expected to be simply a matter of increasing the pulse repetition rate whilst maintaining pulse peak power. Extrapolating from the current results a doubling of average output power should be easily achievable through use of a new isolator.

The motivation of this work was to provide a long wavelength light engine for OCT experiments in the 1800-2400nm wavelength region. This was successfully achieved with a second packaged version of the source currently with project partners. Initial results obtained with this SC source as well as with a previously built ASE source have been very promising. Due to an increased transparency and reduced scattering; paint samples, previously unmeasurable with short wavelength OCT, have shown high transparency and contrast. Application of this source is an on-going area of research.

Within the final section of this chapter we verify the approach of bandwidth tailoring to suppress the detrimental effects of modal interference. We successfully demonstrate the suppression of these effects within a multimode fibre amplifier through the use of broad bandwidth ASE seed. Utilising a simple MOPA arrangement, the variable bandwidth

ASE seed was used to investigate the effects of source bandwidth on modal interference. Showing that by moving to broader bandwidths we can effectively negate these detrimental effects. In a multimode fibre amplifier we demonstrated a greater than 6 times improvement in beam stability as well as significant reduction in peak intensity fluctuations within the active fibre core. This approach of broadband signal propagation for the suppression of detrimental modal interference effects was successfully demonstrated in both active fibre amplification and passive fibre beam delivery and should serve to inform the design of future iterations of multimode fibre amplifiers.

References

1. H. Lefèvre, "Fundamentals of the interferometric fiber-optic gyroscope," Opt. Rev. **4**, 20–27 (1997).

2. D. Huang, E. Swanson, C. Lin, J. Schuman, W. Stinson, W. Chang, M. Hee, T. Flotte, K. Gregory, C. Puliafito, and A. Et, "Optical coherence tomography," Science (80-.). **254**, 1178–1181 (1991).

3. A. C. Akcay, J. P. Rolland, and J. M. Eichenholz, "Spectral shaping to improve the point spread function in optical coherence tomography.," Opt. Lett. **28**, 1921–3 (2003).

4. D. Sampson and W. Holloway, "100 mW spectrally-uniform broadband ASE source for spectrum-sliced WDM systems," Electron. Lett. **30**, 1611–1612 (1994).

5. Y. Wang and C. Xu, "Actively Q-switched fiber lasers: Switching dynamics and nonlinear processes," Prog. Quantum Electron. **31**, 131–216 (2007).

6. P. Wang, J. K. Sahu, and W. A. Clarkson, "110 W double-ended ytterbium-doped fiber superfluorescent source with M2 = 1.6.," Opt. Lett. **31**, 3116–8 (2006).

7. P. Wang, J. K. Sahu, and W. a. Clarkson, "High Power Single-ended Yb-doped Fiber ASE Source," in *Conference on Lasers and Electro-Optics* (IEEE, 2007), p. CFI6.

8. L. Kong, Q. Lou, J. Zhou, D. Xue, J. Dong, and Y. Wei, "2W Yb-doped double-clad fiber superfluorescent source with 42nm 3dB bandwidth," Opt. Laser Technol. **37**, 597–600 (2005).

9. L. Goldberg, J. P. Koplow, R. P. Moeller, and D. A. Kliner, "High-power superfluorescent source with a side-pumped Yb-doped double-cladding fiber.," Opt. Lett. **23**, 1037–9 (1998).

10. D. Y. Shen, L. Pearson, P. Wang, J. K. Sahu, and W. A. Clarkson, "Broadband Tm-doped superfluorescent fiber source with 11 W single-ended output power.," Opt. Express **16**, 11021–6 (2008).

11. O. Schmidt, M. Rekas, C. Wirth, J. Rothhardt, S. Rhein, A. Kliner, M. Strecker, T. Schreiber, J. Limpert, R. Eberhardt, and A. Tünnermann, "High power narrow-band fiber-based ASE source," Opt. Express **19**, 4421 (2011).

12. O. Schmidt, A. Kliner, M. Rekas, C. Wirth, S. Rhein, T. Schreiber, R. Eberhardt, and A. Tuennermann, "Relative intensity noise characterization of a linear polarized 1.1 kW fiber-amplified narrow-band ASE source," in *Frontiers in Optics* (2011), Vol. 4427, p. FTuW3.

13. J. Liu and P. Wang, "High-Power Broadband Thulium-Doped All-Fiber Superfluorescent Source at 2um," Photonics Technol. Lett. IEEE **25**, 242–245 (2013).

14. P. Wang and W. A. Clarkson, "Tunable Yb-Doped Fiber Amplified Sontaneous Emission Source," in *Conference on Lasers and Electro-Optics* (OSA, 2009), p. CFM6.

15. A. Bouchier, G. Lucas-Leclin, F. Balembois, and P. Georges, "Spectrally Narrowed Amplified Spontaneous Emission Source at 977 nm Based on a Single-Mode Ytterbium-Doped Fiber," IEEE Photonics Technol. Lett. **16**, 2021–2023 (2004).

16. R. Paschotta, J. Nilsson, A. C. Tropper, and D. C. Hanna, "Efficient superfluorescent light sources with broad bandwidth," IEEE J. Quantum Electron. **3**, 1097–1099 (1997).

17. R. Youngquist, S. Carr, and D. Davies, "Optical coherence-domain reflectometry: a new optical evaluation technique," Opt. Lett. **12**, 158–160 (1987).

18. E. Swanson, M. Hee, and J. G. Fujimoto, "Application of optical coherence tomography in nondestructive evaluation of material microstructure," Conf. Lasers Electro-Optics 326–327 (1996).

19. R. Su, M. Kirillin, P. Ekberg, A. Roos, E. Sergeeva, and L. Mattsson, "Optical coherence tomography for quality assessment of embedded microchannels in alumina ceramic," Opt. Express **20**, 4603–18 (2012).

20. L. Thrane, T. M. Jørgensen, M. Jørgensen, and F. C. Krebs, "Solar Energy Materials & Solar Cells Application of optical coherence tomography (OCT) as a 3-dimensional imaging technique for roll-to-roll coated polymer solar cells," Sol. Energy Mater. Sol. Cells **97**, 181–185 (2012).

21. E. Rosen and K. Peterson, "Non-Destructive Evaluation of Gas Turbine Thermal Barrier Coatings," in *International Symposium on Optical Coherence Tomography for Non-Destructive Testing* (2013), pp. 55–57.

22. P. Meemon, J. Yao, K.-S. Lee, K. P. Thompson, M. Ponting, E. Baer, and J. P. Rolland, "Optical coherence tomography enabling non destructive metrology of layered polymeric GRIN material.," Sci. Rep. **3**, 1709 (2013).

23. E. Hecht, *Optics* (Addison-Wesley Longman, Incorporated, 2002), p. 698.

24. H. Liang, C. S. Cheung, M. Tokurakawa, J. M. O. Daniel, W. A. Clarkson, M. Spring, and D. Thickett, "Next Generation Optical Coherence Tomography for Art," in *CHARISMA* (2013), Vol. 111.

25. M.-J. Li, X. Chen, A. Liu, S. Gray, J. Wang, D. T. Walton, and L. A. Zenteno, "Limit of Effective Area for Single-Mode Operation in Step-Index Large Mode Area Laser Fibers," J. Light. Technol. **27**, 3010–3016 (2009).

26. E. Stiles, "IPG Photonics Fiber Lasers : The Flexible Tool for High Power Laser Welding," in *AWS New Welding Technologies Conference* (2010).

27. G. Verhaeghe, "Remote Laser Welding for Automotive Seat Production (keynote)," in *SPIE Photonics West* (2013).

28. "TruDisk - TRUMPF Laser Technology," http://www.trumpf-laser.com/en/products/solid-state-lasers/disk-lasers/trudisk.html.

29. A. Kratky, D. Schuöcker, and G. Liedl, "Processing with kW fibre lasers - advantages and limits," in *International Symposium on Gas Flow and Chemical Lasers and High Power Lasers.* (2008), Vol. 7131.

30. M.-Y. Cheng, Y.-C. Chang, A. Galvanauskas, P. Mamidipudi, R. Changkakoti, and P. Gatchell, "High-energy and high-peak-power nanosecond pulse generation with beam quality control in 200-microm core highly multimode Yb-doped fiber amplifiers.," Opt. Lett. **30**, 358–60 (2005).

31. E. A. Shcherbakov, V. V Fomin, A. A. Abramov, A. A. Ferin, D. V Mochalov, and V. P. Gapontsev, "Industrial grade 100 kW power CW fiber laser," Adv. Solid-State Lasers Congr. **5**, 5–7 (2013).

32. H. Yoda, P. Polynkin, and M. Mansuripur, "Beam quality factor of higher order modes in a step-index fiber," J. Light. Technol. **24**, 1350–1355 (2006).

33. S. Wielandy, "Implications of higher-order mode content in large mode area fibers with good beam quality.," Opt. Express **15**, 15402–9 (2007).

34. J. S. P. Chan, P. Wang, J. K. Sahu, and W. A. Clarkson, "Impact of modal interference on the output beam properties of large-core cladding-pumped fiber amplifiers," Conf. Lasers Electro-Optics **3**, 1–2 (2008).

35. R. J. Bartula, "Estimation of signal noise induced by multimode optical fibers," Opt. Eng. **47**, (2008).

36. W. W. Rigrod, "Saturation Effects in High-Gain Lasers," J. Appl. Phys. **36**, 2487 (1965).

37. H. Sabert and E. Brinkmeyer, "Pulse generation in fiber lasers with frequency shifted feedback," J. Light. Technol. **12**, 1360–1368 (1994).

38. J. Flaud, A. Barbe, and N. Husson, "REFERENCES and SOURCES for HITRAN," 4058–4097 (2013).

39. J. M. J. R. T. Dudley, *Supercontinuum Generation in Optical Fibers* (Cambridge University Press, 2010), p. 404.

40. J. H. Lee, Y.-G. Han, and S. Lee, "Experimental study on seed light source coherence dependence of continuous-wave supercontinuum performance.," Opt. Express **14**, 3443–52 (2006).

41. C. S. Cheung, M. Tokurakawa, J. M. O. Daniel, W. A. Clarkson, and H. Liang, "Long wavelength optical coherence tomography for painted objects," in *SPIE Optical Metrology* (2013), Vol. 8790, p. 87900J–87900J–5.

Chapter 5.

Mode selection in multimode fibre laser oscillators

5.1 Introduction

As we have discussed throughout the thesis there is a strong motivation within industry and academia to increase output power and pulse energy from fibre laser sources. This is generally achieved with core area scaling due to the higher thresholds for detrimental nonlinear processes and also from an energy storage perspective. As we have discussed in the previous chapters, techniques to maintain fundamental mode operation become less effective as core area is increased and can be difficult and costly to implement, leading to undesirable effects such as beam quality degradation and modal interference. Whilst in Chapter 4 we demonstrated a technique for the suppression of the effects of modal interference in a multimode output beam, some applications still require the better beam quality of the fundamental Gaussian mode.

In addition to the fundamental mode operation of multimode waveguides, it has been shown that particular applications can actually benefit from operation on individual higher order modes, such as some laser processing applications, where the desired beam profile and polarization behaviour is dictated by the type of material being processed [1,2]. Indeed, the use of doughnut-shaped beams or beams with adaptable transverse profiles can yield substantially higher processing speeds as well as improved cut quality for laser cutting. Besides the applications potential, operation on higher order modes within an optical fibre laser can also have benefits within the resonator itself. Such as higher thresholds for detrimental nonlinear loss processes [3], reduced sensitivity to mode skew [4] and the potential for improved energy extraction in pulsed systems.

To date, techniques for the selection of the fundamental mode (or individual higher order modes) in multimode fibre oscillators have often been quite difficult to implement and lack the flexibility to select between modes after implementation.

In this chapter we present a simple technique for the selection of individual transverse modes within a multimode fibre oscillator. We exploit the different spectral responses of in-fibre Bragg gratings (FBG's) and free space wavelength selective elements (i.e. volume Bragg gratings (VBG's) or acousto-optic tunable filters (AOTF's)) to simultaneously achieve wavelength selection and spatial mode selection within a simple, multimode fibre laser oscillator with an external cavity feedback architecture. In the experimental section of this chapter we apply this approach to several different fibre laser oscillator designs. Firstly we demonstrate a core pumped thulium-doped fibre laser, with a multimode core and an external cavity containing an electronically addressable AOTF. With this arrangement we successfully demonstrate the feasibility of this mode selection technique, through the selection of the fundamental mode or the next higher order mode within the multimode waveguide with near perfect beam profiles. In addition, due to the electronically controllable nature of the AOTF we demonstrate rapid switching between these laser modes at 10's of kHz rates. Secondly, we demonstrate the electronic control of the time averaged fibre output beam profile. This is achieved through simultaneous selection and incoherent superposition of multiple laser modes within the oscillator. With output beam profiles ranging from flat-toped through to Gaussian and doughnut shapes with a high degree of control. We then extend this approach to a cladding pumped architecture, with the successful implementation of mode control and selection using only passive components. Finally we discuss the prospects for further scaling core area via this technique.

5.2 Background theory

5.2.1 Free space Bragg selective elements

As presented in Chapter 3, the resonance for a free space Bragg grating selective element is given by the grating period, mean refractive index of the medium and the incident angle. The resonance wavelength λ_{FS} of a free space Bragg selective element is given by:

$$\lambda_{FS} = 2n_0\Lambda_{FS}\cos\theta \quad (33)$$

where θ is the angle of incidence of the incoming signal with respect to the grating normal, n_0, is the mean refractive index of the medium and Λ_{FS} is the spatial period of the grating. Volume Bragg gratings (VBGs) and acousto-optic tunable-filters (AOTFs) are common examples of free-space Bragg selective elements. Volume Bragg gratings, where a Bragg period is written into the volume of photo-thermo refractive (PTR) glass, have a fixed resonance wavelength when operated at normal incidence. However, by changing the angle of incidence θ the resonance wavelength of the VBG can be down-tuned to shorter wavelengths allowing narrowband wavelength tuning [5]. In the case of an acousto-optic device such as an AOTF the Bragg period is no longer fixed by photo-inscription, but rather defined by the period of an incident acoustic wave driven by an input RF signal. By changing the RF drive frequency, and hence acoustic wavelength, the resonance wavelength of the AOTF can also be shifted. A unique property of the AOTF is the static position of deflected beam independent of the grating period (RF drive frequency). This allows an AOTF to be used as a wavelength-tunable element without any need for physical movement of the optical system.

5.2.2 Multimode fibre Bragg gratings

For the case of Bragg gratings written into waveguides the effect of mode propagation on the Bragg resonance wavelength must be taken into account. Bragg resonance within a waveguide is dependent on the effective index of the guided modes rather than a mean index of the medium as is seen in free space Bragg selective elements. For in-waveguide gratings the Bragg condition is given by:

$$\lambda_{FBG} = 2n_{eff}^{m}\Lambda_{FBG} \quad (34)$$

where, Λ_{FBG} is the grating period within the waveguide, n_{eff}^{m} is the effective index of the guided mode m and λ_{FBG} is the wavelength at which resonance occurs. The propagation constant and associated effective index n_{eff} of guided modes in a step index waveguide is governed by the core and cladding refractive indices as well as the modal order, where $n_{core} > n_{eff} > n_{clad}$. The fundamental mode has an effective index closest to that of the core, with higher order modes having progressively lower effective indices until the

condition for guidance is no longer met. Thus, for a Bragg grating written into a multi-mode waveguide the Bragg condition for each mode is satisfied at different wavelengths. Hence, higher order modes propagating with a lower effective index to that of the fundamental mode see resonance at shorter wavelengths. This phenomenon manifests itself as a multi-peak behaviour in both the transmission and reflection spectrum of multi-mode FBGs [6,7] as demonstrated in Figure 5.1.

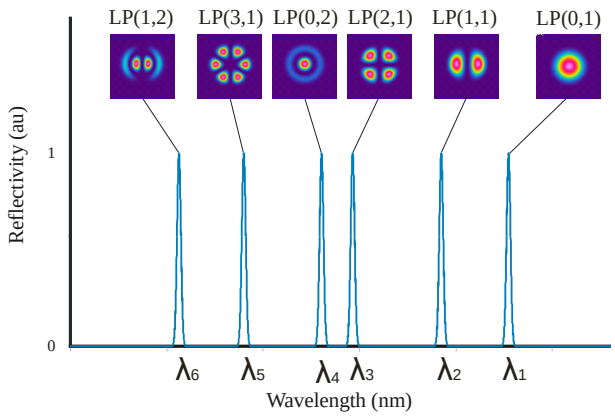

Figure 5.1: Conceptual example demonstrating the modal-dependent nature of the reflection spectrum of a fibre Bragg grating written into a step index multimode fibre.

Other effects such as cross coupling peaks [8] can sometimes be seen in multimode FBG's and are a result of non-uniform grating inscription, these effects are discussed further in section 5.7.3.

5.2.3 Novel mode selection technique

If we construct a laser oscillator consisting of a free space wavelength-selective element and a fibre Bragg grating written into a multimode active fibre (Figure 5.2) we can exploit the modal dependence of the fibre Bragg grating and the wavelength dependence of the free space element (i.e. volume Bragg grating or AOTF). This allows us to selectively excite a single spatial mode within the multimode oscillator. To achieve this we simply set the resonance wavelength of the free space wavelength selective element to be equal to the FBG resonance wavelength of the desired mode *m*.

$$\cos\theta = \frac{n_{eff}^{m}\Lambda_{FBG}}{n_0\Lambda_{FS}} \tag{35}$$

In this situation the resonant mode will experience a lower threshold (due to increased feedback provided by the external cavity) in comparison to other guided modes. In this architecture the FBG can be thought of as a mode discriminating mirror, where at a given wavelength it will only reflect light within a single resonant mode whilst transmitting all other modal content. This technique has the ability to provide a low threshold for the selected mode whilst still maintaining a high threshold for other guided modes.

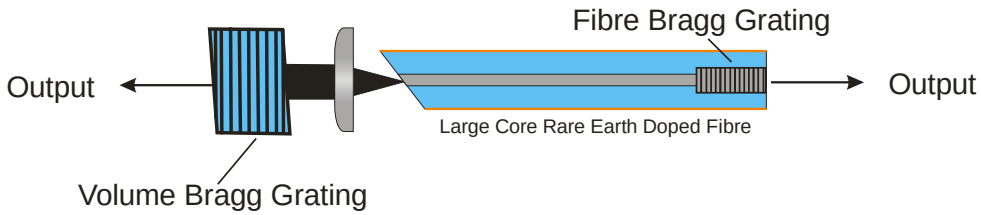

Figure 5.2 Conceptual layout of mode selection technique, demonstrating the free space wavelength selection using volume Bragg grating and modal dependent fibre Bragg grating.

5.2.4 Lasing thresholds with mode selection

For a simple three level laser the threshold of absorbed pump power for the onset of lasing is given by [9]:

$$P_{ths} = \frac{Ah\nu_p}{2\tau_f\eta_q\left(\sigma_e(\lambda_l)+\sigma_a(\lambda_l)\right)}\left[2\sigma_a(\lambda_L)Nl + 2\alpha_L l - \log_e(R_{OC}) - \log_e(R_{HR})\right] \tag{36}$$

where A is the doped area of the waveguide, $h\nu_p$ is the photon energy at the pump wavelength, τ_f is the fluorescence lifetime of the upper laser level, η_q is the pumping quantum efficiency (i.e. the number of electrons excited into the upper laser level for every pump photon), $\sigma_a(\lambda_l)$ and $\sigma_e(\lambda_l)$ are the absorption and emission cross-sections at the lasing wavelength, N is the lasing dopant density, l is the device length, α_L is the cavity background loss at the lasing wavelength and R_{OC} & R_{HR} are the feedback reflectivites of the laser output coupler and HR mirror respectively.

The above equation is based on a simple three level system (Ytterbium) without the additional processes that can be present in thulium such as energy transfer upconversion

(ETU) and other detrimental processes. It also assumes negligible ASE. However for the purpose of this section it is considered sufficient to gain simple insights into the laser behaviour.

We can estimate the difference in threshold between the fundamental mode and higher order modes that can be achieved with this above mentioned mode selection technique by looking at the ratio of threshold powers for the selected mode (*m*) and all other modes (*hom*). Using the approximation for laser threshold as given above (eq.(36)) and solving for the ratio of threshold powers for the selected mode (*m*) and all other modes (*hom*) we find the following:

$$\frac{P_{abs-th}^{hom}}{P_{abs-th}^{m}} = \frac{2\sigma_a(\lambda_L)Nl + 2\alpha_L l - \log_e\left(R_{OC}^{hom}\right) - \log_e(R_{HR}^{hom})}{2\sigma_a(\lambda_L)Nl + 2\alpha_L l - \log_e(R_{OC}^{m}) - \log_e(R_{HR}^{m})} \tag{37}$$

The first two terms of the above ratio correspond to reabsorption and cavity background losses at the lasing wavelength. For a thulium fibre laser operating at the long wavelength end of the emission spectrum we can neglect reabsorption losses (i.e. a four level approximation) and assume negligible background loss across a short device length. The remaining terms correspond to laser output coupling and high reflector feedback efficiency. As the feedback element in this arrangement is a HR fibre Bragg grating with uniform reflectivity for all modes (R_{HR}~90%) and that the only difference in feedback between the modes is between the wavelength selective element (assume R_{OC}~20%) and angle cleaved output facet (assume R_{OC}~10^{-5}%). The result of this is $\log_e(R_{OC}) \gg \log_e(R_{HR})$ and eq.(37) becomes:

$$\frac{P_{abs-th}^{hom}}{P_{abs-th}^{m}} \approx \frac{\log_e\left(R_{OC}^{hom}\right)}{\log_e(R_{OC}^{m})} \tag{38}$$

For this we neglect the effects of ASE and assume a complete overlap with inversion of both the selected mode and higher order modes. This allows us to approximate the lowest difference in threshold between the selected mode and non-selected modes. For the above reflectivity parameters we find the threshold for higher order mode operation is ~6 times that of the selected mode.

This then raises the question of whether the mode selection technique is limited to a given number of times above threshold before parasitic higher order mode operation occurs.

To gain an insight into this question we can look at the situation for fundamental mode selection within a multimode fibre (assuming an initially top-hat inversion distribution across the area of the core). In Figure 5.3 we show the spatial overlap between the selected Gaussian mode and this distribution. Here we can see at the mode centre, where intensity is greatest, spatially dependent gain saturation is expected to be high. However, as we move away from the mode centre into the lower intensity wings, we can expect a much lower level of saturation. In this situation there is the possibility for modes with high spatial overlap with the undepleted region to reach lasing threshold as pump power is increased, leading to a loss of modal purity and a reduction in beam quality. As the difference in thresholds between the selected mode, P_{abs-th}^{m}, and non-selected modes, P_{abs-th}^{hom}, increases, the achievable intensity of the selected mode before P_{abs-th}^{hom} is reached also increases. For sufficiently large differences in threshold between the selected and non-selected modes, the intensity of the selected mode can be high enough to saturate spatially dependent excess gain before P_{abs-th}^{hom} is reached and thus prevent the onset of parasitic higher order mode lasing. The difference in thresholds required to prevent the onset of parasitic lasing will be dependent on the profile of the selected mode, active fibre core diameters, mode confinement and overlap between the guided modes of the fibre.

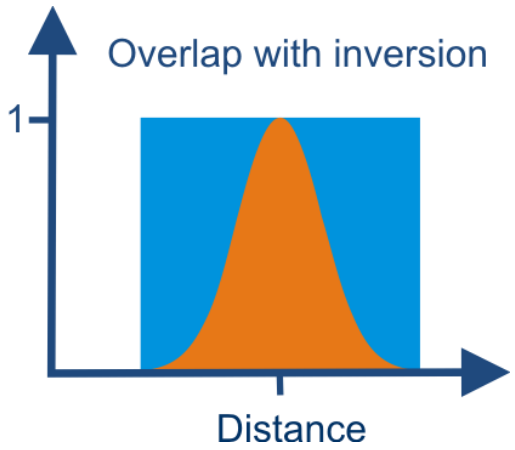

Figure 5.3 Example of the spatial overlap between a top-hat inversion distribution (blue region) and the fundamental Gaussian mode (orange) of uniformly doped step index optical fibre.

Modelling conducted within the group suggests, that for the Gaussian mode and an initially top-hat inversion distribution (Figure 5.3), this saturation behaviour starts to become significant at around 4 times the lasing threshold with level of excess inversion within the wings decreasing from this point. At around 8-10 times threshold, the

extraction efficiency of the fundamental mode is essentially equal to that of a top-hat profile of uniform spatial overlap with inversion [10] and thus expected to suppress the onset of higher order modes. Experimentally, we can check for these conditions by monitoring for beam quality degradation as pump power is increased.

5.3 Application and generation of higher order modes

In the previous chapters of this thesis we discussed the applications of the fundamental Gaussian mode. The high beam quality and focusability of the Gaussian mode is desirable in many applications. Within this section we will look at the motivation for operation on non-Gaussian profiles such as individual higher order modes or a combination of modes.

The differing demands of different laser processing and marking applications means that no one laser beam profile is ideal for all applications. For example, the fine feature formation desired in stent manufacture requires the high beam quality and small spot sizes associated with Gaussian modes. However, for larger volume ablation applications, such as ITO removal used within the semiconductor industry, a more uniform energy deposition is desired; allowing the threshold for ablation to be met but not significantly exceed [11]. Here we will look at a range of applications for non-Gaussian beam profiles within the materials processing sector.

By processing with laser beam profiles other than the Gaussian, a wider parameter space can be accessed. Annular beams with central nulls and doughnut shaped intensity profiles possess some interesting properties. The central null seen in ring shaped intensity profiles has important implications for temperature deposition and material removal, by appropriately selecting the width and radius of the incident beam, much more uniform heat profiles can be achieved than would be possible with Gaussian or top-hat profiles. Leading to uniform processing and reduced heat affected zones [12]. The use of novel beam shapes can also allow higher throughput for complex marking applications. By pre-shaping the indecent laser beam profile to match a desired mark or hole shape it is possible to essentially project this shape on to the material to be processed. Sanner et al utilised a spatial light modulator based beam reshaping system to transform the Gaussian beam of a femtosecond source into a range of different profiles [13], in this work the authors demonstrate the accurate transfer of laser beam profile to marked profile on the work piece (Figure 5.4). Zhang et al utilise a so-called ‘pitchfork’ beam profile to

produce well-defined through holes for a micro drilling application. Here the beam showed a top-hat like shape with a raised ring around the periphery and resulted in an improved hole fabrication with cleaner profile in comparison to a holes drilled with Bessel and Gaussian beam profiles [14]. In [15] Zeng demonstrates the use of large diameter annular beams for 'optical trepanning' where core holes are cut from a surface, here the use of the a large ring shape more efficiently removes material, resulting in reduced heating and faster processing.

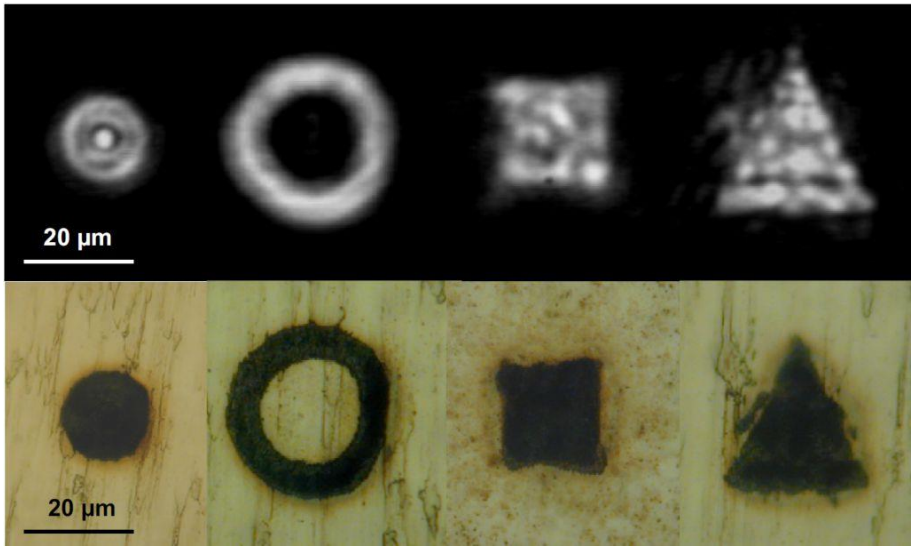

Figure 5.4 Beam profiles from a femtosecond laser system after transformation through a beam shaping system (top). The results of the above beam profiles when used to machine the surface of a stainless steel sample, from [13]

The polarisation properties of some doughnut shaped beams follow a radial or azimuthal profile about the beam radius [16]. This radial or azimuthal polarisation can have some interesting effects on material interactions and has been shown to enhance removal of metals such as mild steel [2].

Although we have highlighted some promising results above, this area of laser processing has to date been largely unexplored, partly due to the difficulty in obtaining appropriate sources, and is a promising area of future research.

5.3.1 Techniques for generation of higher order modes

The generation of higher order modes for laser processing applications can be achieved in a number of different ways. It is possible to use components external to the laser

resonator as beam converters to generate the desired beam shapes. This approach has the attraction of simplicity as well as the ability to use standard laser sources prior to beam reshaping. This external cavity approach can utilise diffractive optical elements [17], microlens arrays [18], axicons [19] and more recently, phase plates [20] and spatial light modulators (SLM's) [21–23] to generate a range of different beam profiles. Commonly an initially Gaussian shaped beam profile is transformed to a top-hat, ring shape or other novel profiles.

Work has also focused on the direct generation of the desired beam profiles within a laser resonator, and can have the advantage of higher quality mode profiles in comparison to external conversion schemes. In bulk laser cavities, aperturing elements can be used to cause the resonator to oscillate on higher order modes [24]. More recently the use of a spatial light modulator in an intracavity configuration has allowed the near arbitrary generation of resonator modes and combinations through computer control [25]. The use of a spatial light modulator in this cavity did come at a cost to laser power and slope efficiency, leading to an increased threshold pump power of 22W and limited output power of 14mW. This was due to increased losses and limited power handling of the intracavity SLM. Generally the use of hard aperturing within a resonator must come at the cost of laser efficiency due poorer overlap with pump profile, although this effect can be mitigated. Through the use of spatially tailored pump profiles it is possible to select higher order modes by virtue of higher overlap with the pump distribution. Here in order to generate a desired mode, the pump beam is spatially reshaped to more closely match the intensity profile of the desired mode. This has been demonstrated with the generation of doughnut shaped modes, where a initially top-hat shaped pump profile was transformed to that of a ring shape. This allowed the generation of modes with radial and azimuthal polarisation [26,27] or an approximation of these polarisation properties [28] to be generated without detrimentally effecting laser slope efficiency.

Similar approaches to mode selection can be applied to fibre laser oscillators. Through the use of inversion overlap tailoring, Kim et al also demonstrated the generation of ring shaped modes in an optical fibre [29]. In addition to these schemes, due to the waveguiding nature of fibre lasers, alternative approaches may also be employed. Ramachandran et al demonstrated the conversion from a Gaussian mode to a range of higher order ring shaped modes through the use of a long period grating to induce mode coupling, and was demonstrated with conversion efficiencies of ~99% [30,31].

5.4 Mode selection in a multimode thulium fibre laser

5.4.1 Bragg resonances of the active fibre

In order to write high reflectivity fibre Bragg gratings we must ensure that a photosensitive fibre is used. This is normally achieved with the addition of germanium as a dopant in passive optical fibre. Fibre Bragg gratings can then be written into these photosensitive fibres and spliced to active fibres to form a laser cavity. In our experiments we were hesitant to introduce any potential sources of mode coupling and decided against the use of fusion splicing. By doping our active fibre with germanium, we were able to create photosensitive active fibre negating the need for matched passive fibres and fusion splicing. This photosensitive thulium doped fibre was fabricated in-house via MCVD and solution doping techniques and allowed direct writing of FBG's into the core of the active fibre.

The drawn fibre had a 18μm diameter aluminosilicate core (0.22NA equivalent) with approximately 1 wt.% Tm and a D-shaped pure silica inner-cladding with an outer dimension of 300μm. The later was coated with a low refractive index UV-cured polymer yielding a numerical aperture of ~0.46 for the inner-cladding pump guide. Prior to any grating inscription (with the UV phase mask technique) hydrogen loading of the fibre was performed to further enhance photosensitivity of the active core [32].

The use of commercially available finite element method modelling software (Comsol) allowed us to make predictions of the of the Bragg resonance wavelength for the guided modes of this fibre. Input parameters were taken from the experimentally measured optical fibre refractive index profile (Photon Kinetics S14). The results of this modelling provided values for the effective indices of the guided modes as well as an estimation of the modal propagation loss. These values were then normalised to the fundamental mode resonance wavelength and were used to calculate the expected resonance wavelengths of higher order modes propagating in the multimode fibre.

Figure 5.5 shows the calculated reflectivity peak locations for a Bragg grating (λ_0=1925.5nm) written into the core of this fibre, with inserts showing the expected modal profiles. An important value for the successful selection of modes using this technique is the nearest neighbour wavelength spacing between modes. Here we see a wavelength spacing of ~4.3nm between the fundamental and LP_{11} mode peaks.

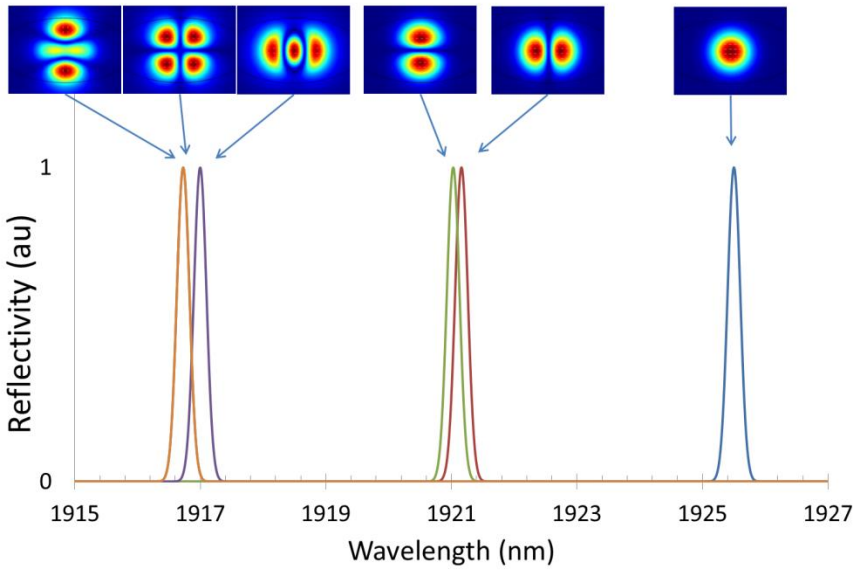

Figure 5.5 Calculated reflectivity spectrum for fibre Bragg grating written into multimode Tm-doped fibre.

The results of this modelling also show the slightly unexpected behaviour of multiple peaks at the nominally single peaked LP_{11} resonance. The LP_{11} mode within a step index fibre is actually an approximation of the four normally degenerate vector modes (TE_{01}, TM_{01}, HE_{21} and HE_{21}*). This behaviour suggests that a walk-off in propagation constants has occurred between these modes. Upon further investigation it was found that a fibre drawing induced core ellipticity (due to the shaped cladding) leads to a non-degeneracy of these vector modes [33]. This behaviour is demonstrated in Figure 5.6 where we plot the effective index of these four vector modes against an increasing fibre core ellipticity. Here we can see the same splitting of this mode group into two degenerate pairs. Additionally the intensity profile of these modes can be seen to transfer from a circularly symmetric profile into a two lobed shape.

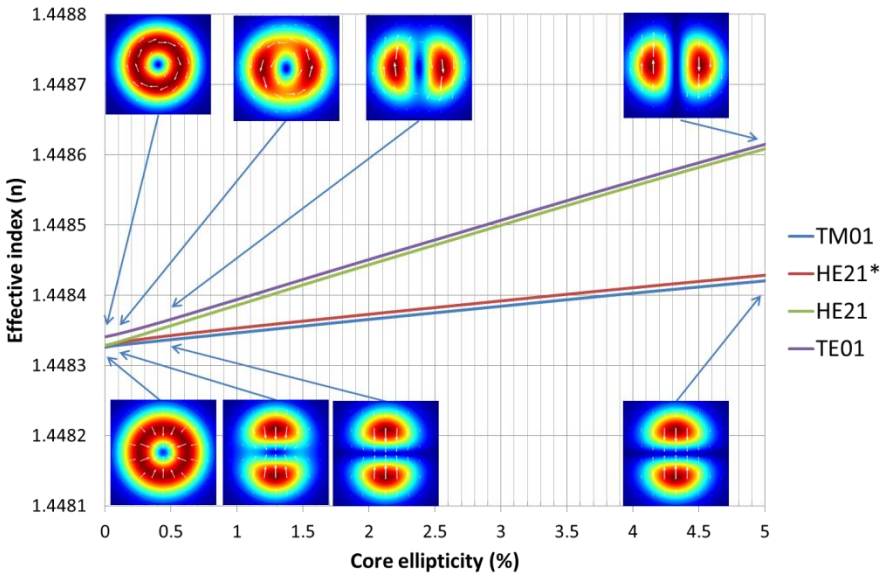

Figure 5.6 Mode profiles and effective index separations of the LP_{11} mode group in the presence of an elliptical fibre core.

5.4.2 Electronic mode control

To demonstrate the feasibility of this mode selection technique we constructed a simple laser resonator containing an in-fibre Bragg grating and an external cavity consisting of a wavelength selective AOTF feedback arrangement. By using an electronically-addressable wavelength-selective element within the external-cavity we are able to select the oscillating mode within the resonator without the need for any mechanical movement. This allows the switching of transverse modes within the oscillator without any realignment or physical movement. This electronic control also has the advantage of allowing mode switching to be performed at very fast rates, nearing that of the AOFT rise time. In this section we describe the mode selection results for a core-pumped multimode Tm-doped silica fibre, where we have successfully excited and switched between the fundamental mode (LP_{01}) and the next higher order mode (LP_{11}) of this active fibre at output power levels in excess of 5W. These were selected by simple adjustment of the RF drive frequency to the AOTF. Fast switching rates between these modes has also been realised with switching rates up to 20kHz demonstrated.

5.4.3 Experimental layout and results

We constructed the experimental arrangement shown in Figure 5.7, comprising of a 30cm length of thulium doped active fibre with a Bragg grating at one end of the active fibre and a 14° angle cleave to suppress broadband feedback. An external cavity consisting of a half wave plate, AOTF and broadband reflector (HR) was used to provide wavelength-dependent feedback as well as laser output coupling. The use of a half-wave plate in the external cavity allowed the polarization direction of the laser output to be aligned for optimum diffraction efficiency in the AOTF.

Pump light was provided by a commercially available 20W single-mode 1565nm Er,Yb fibre laser source (SPI lasers) and was coupled into the doped fibre with the aid of an all fibre wavelength division multiplexer (WDM). The FBG had an estimated reflectivity of >80% for the fundamental mode and bandwidth of 0.2nm (FWHM). Bragg resonance for the fundamental mode was at 1925.5nm under unpumped conditions. The AOTF used in our experiment was supplied by Gooch & Housego and could be operated across the entire 1700-2100nm Tm emission band. The single-pass bandwidth of the AOTF was 2nm (FWHM) at 2000nm and the single-pass diffraction efficiency could be varied from 0-70% for a linearly-polarized input.

The choice of using the FBG as high reflector within the cavity was made after initial experimentation using an FBG as a laser output coupler. When used as an output coupler, the FBG required near perfect external cavity feedback alignment, both in angle and in mode size to ensure mode scrambling does not occur at the free space to fibre boundary. Experimentally this was found to be very changeling and not achievable in any repeatable way. However by using the FBG as a HR reflector, any mode scrambling due to misalignment is simply passed through the FBG rather than back reflected. In this way the FBG works to clean up the back reflected mode. This is because the FBG will only reflect mode content from a single mode at a given wavelength transmitting all other modes.

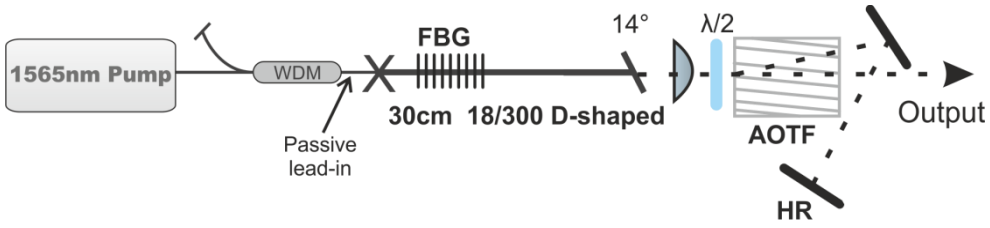

Figure 5.7 Experimental layout of core-pumped mode selective cavity containing an in-fibre Bragg grating written into the core of thulium doped active fibre and a free space external cavity containing wavelength-selective AOTF.

An expanded spectrum showing the predicted peaks for the first two sets of guided modes is shown in Figure 5.8. Resonance for the fundamental mode is seen at 1925.5nm. With dual peaks seen around 1921.1nm. The modal profile associated with each of these peaks is shown above the calculated reflection spectrum of the grating. As can be seen, at the 1921nm wavelength peak two-lobed mode profiles are generated with the mode orientation dependent on the excitation wavelength. Overlaid on this FBG spectrum is the expected single pass transmission bandwidth of the AOTF. When operating at resonance for the LP_{01} (R.F. drive frequency one (RF1)) clean single mode excitation is expected due to the large wavelength spacing between the fundamental and LP_{11} modes. However, when tuned to the LP_{11} peaks (R.F. drive frequency two (RF2)) the excitation of multiple modes is expected. In this case, with equal feedback for the LP_{11x} and LP_{11y} modes, an incoherent superposition of the two LP_{11} modes is formed. This incoherence is due to the separation in wavelength of these modes and is expected to result in a doughnut shaped intensity profile when exciting these peaks.

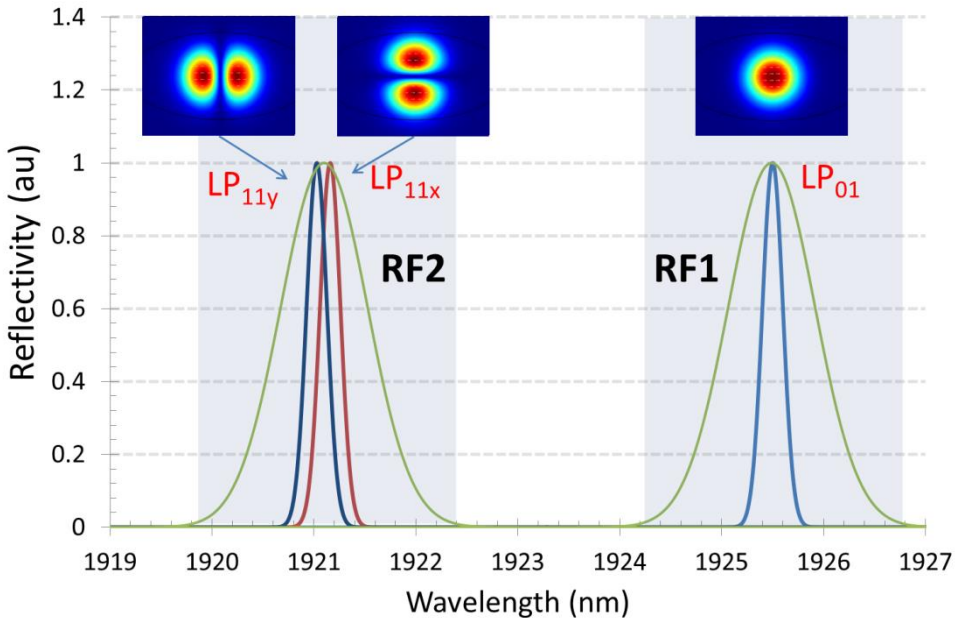

Figure 5.8 Close up of FBG reflection peaks of the fundamental and LP_{11} modes, overlaid on this is the single pass selection bandwidth of the AOTF (green shaded area) and calculated mode profiles for the corresponding peaks.

Using an arbitrary function generator the RF drive frequency of the AOTF was adjusted to allow the operating wavelength to be tuned across the Bragg resonance peaks of this multi-mode FBG. In CW mode of operation the fundamental or next higher order modes could be selected. Figure 5.9 shows the successful selection of the fundamental mode (Figure 5.9(a)) and doughnut-shaped (incoherent superposition) of LP_{11} modes (Figure 5.9(b)) within the multimode fibre. These results were achieved without any cavity realignment when selecting between the two modes. Due to the limited wavelength resolution of the AOTF and FBG, as well as a close effective index spacing (and hence wavelength spacing) of still higher order modes, it was not possible to excite modes of a higher order than the LP_{11} group individually. The resonance wavelength of the FBG was found to be pump power dependent with ~4pm/W shift to longer wavelengths. The latter was attributed to quantum defect heating in the fibre core. At a launched pump power of 17W the fundamental mode resonance was 1926.2nm, whilst the next guided modes corresponding to the LP11 group of modes were found to lase at 1922nm.

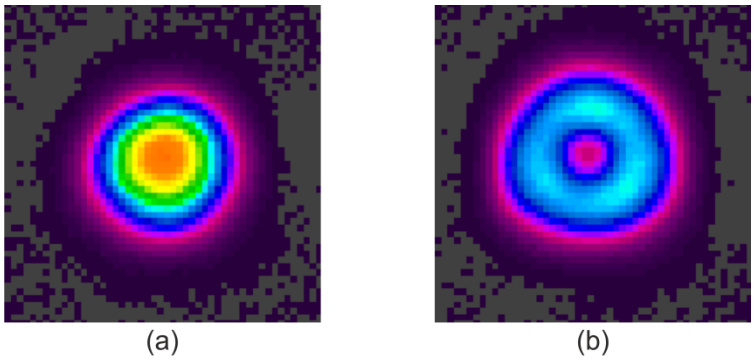

Figure 5.9 Laser output beam profiles successfully demonstrating the mode selection of individual modes within a multimode fibre oscillator. (a) AOTF tuned to the LP_{01} mode peak and (b) AOTF tuned to the LP_{11} mode superposition.

At the maximum pump power of 17W, the output powers for the LP_{01} mode and a doughnut-shaped LP_{11} superposition were 5.8W and 5.1W respectively (see Figure 5.10). Additionally, the emitted modes demonstrated a linear polarization perpendicular to the optical bench, with the LP_{11} superposition demonstrating a polarization extinction ratio (PER) of ~10dB, whilst the fundamental mode had a PER of >20dB. The beam propagation factors (M^2) for the fundamental mode and LP_{11} superposition were measured to be 1.07 and 2.23 respectively.

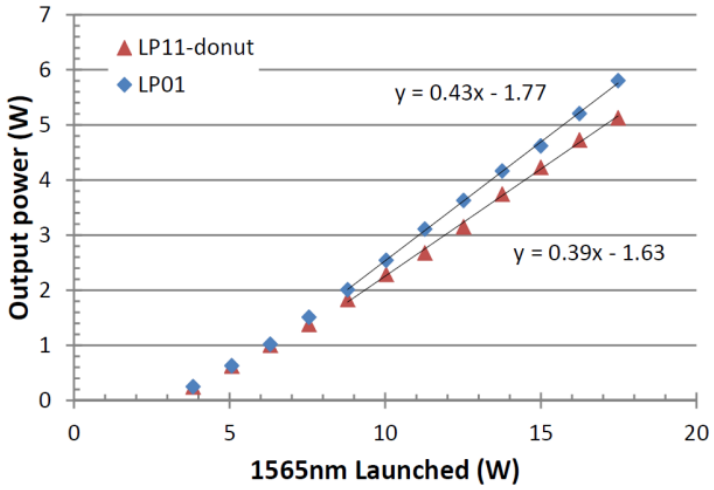

Figure 5.10 Laser output power for LP_{01} (blue) and $LP_{11\text{-doughnut}}$ (red) modes versus launched pump power.

When tuned to the LP_{11} doughnut, the laser emission spectrum was indeed found to comprise of two spectral peaks of roughly equal power separated by ~0.2nm. Any misalignment of the feedback mirror in the plane of incidence (or in the orthogonal

direction) resulted in a reduction in power for one of the emission wavelengths and a noticeable two-lobe intensity profile associated with preferential lasing on a particular LP_{11} mode orientation. To further investigate the spectral and modal properties of the LP_{11} peaks, a solid etalon of 0.5mm thickness (2.5nm free-spectral-range) and double-pass bandwidth of 0.05nm was inserted into the external cavity between the AOTF and HR mirror. This etalon was used to enhance wavelength discrimination within the feedback cavity to allow the individual peaks of the LP_{11} mode group to be resolved. With the AOTF tuned to the LP_{11} peak, the solid etalon was angle tuned to match either wavelength peak of the dual peak output. The results (illustrated in Figure 5.11) confirm that the two lobe output profile orientation was dependent on the resonance wavelength. The two lobe orientation changed by 90 degrees when etalon transmission peak, and hence lasing wavelength, was adjusted from the 1921.7nm peak to the 1921.9nm peak in agreement with our theoretical model.

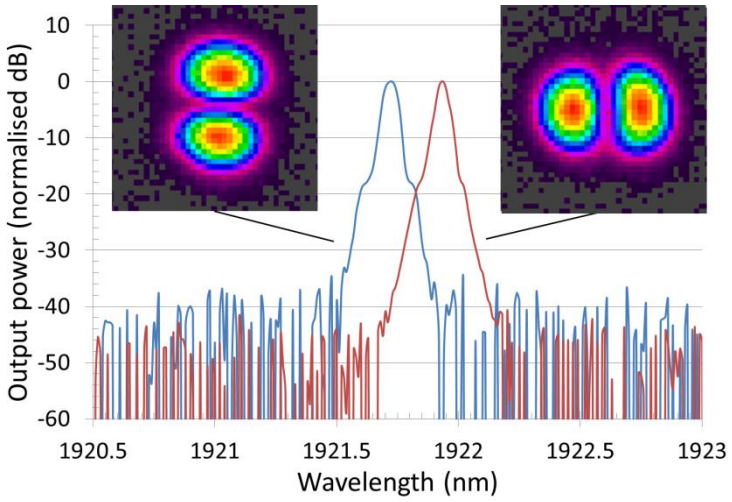

Figure 5.11 Output spectrum and corresponding beam profiles when tuned to the LP_{11} mode group with solid etalon used for fine wavelength selection.

By switching the resonance wavelength of the external cavity between resonance for the fundamental mode and resonance for the doughnut-shaped superposition of modes we could switch rapidly between the two mode shapes. This useful feature of laser behaviour is made possible by the ability to rapidly switch between resonance wavelengths in an AOTF. With the appropriate fibre, FBG and AOTF, this technique could also be extended to a wider range of transverse modes. To investigate the limits on the switching behaviour in our present laser, the feedback wavelength for the AOTF was switched between LP_{01}

and LP_{11} lasing wavelengths at repetition rates ranging from ~Hz to > 10kHz. The laser output profile was monitored using a combination of pyroelectric array camera and fast photodiode. For repetition rates up to 24Hz, the Pyrocam allowed direct observation of complete switching between the LP_{01} and LP_{11} modes. However at increased switching rates direct observation of laser switching behaviour was not possible due to the limited frame rate (48Hz) of the pyroelectric array. To investigate switching behaviour at higher frequencies, a volume Bragg grating with 0.5nm FWHM transmission bandwidth and >95% reflectivity was enlisted. This allowed the reflection of one wavelength whilst transmitting the other. Here the VBG was used to reflect either the 1922nm or 1926nm peak. This was then incident on fast photodiodes and power meter, and allowed the direct measurement of the relative mode power. The laser switching behaviour for repetition rates up to 40kHz was investigated using this technique. At low frequencies, the output profile of the laser was simply that of equal power of LP_{01} and LP_{11} doughnut. Whilst at higher switching frequencies, the LP_{01} mode tended to dominate the laser output. Adjustment of the relative RF drive powers on the AOTF, and hence the relative optical feedback efficiencies for the two modes, allowed this effect to be mitigated. This resulted in equal excitation of the fundamental and doughnut shaped modes at up to repetition rates of 20kHz. For switching frequencies above this, the limited build-up time for the AOTF wavelength selection resulted in too short a feedback duration for stable lasing to occur. Figure 5.12 shows the time profiles for 1kHz, 10kHz and 20kHz switching rates.

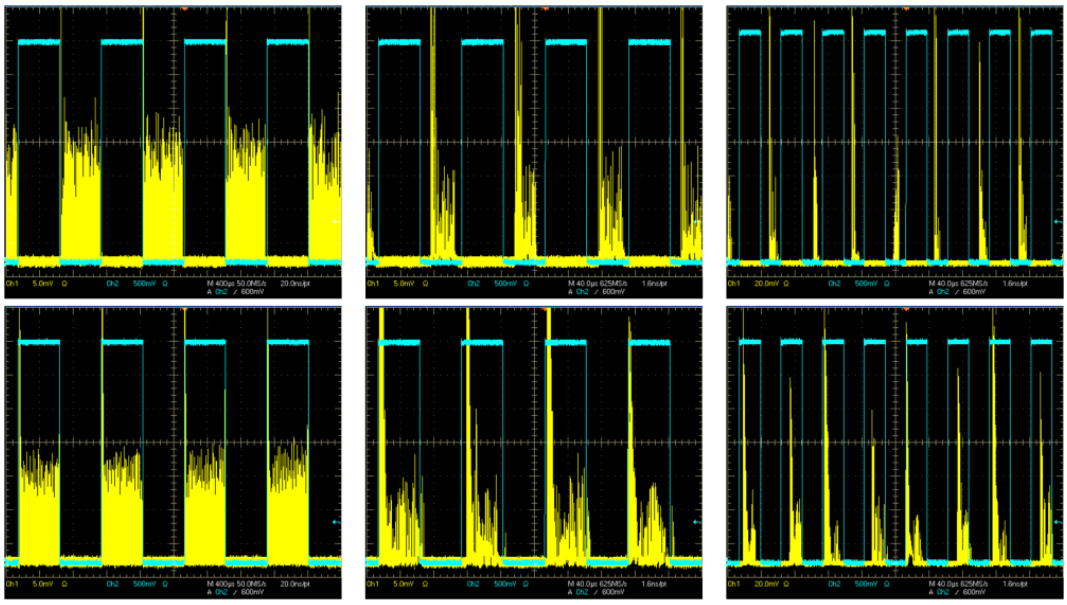

(a) 1kHz (400µs/dev) (b) 10kHz (40µs/dev) (c) 20kHz (40µs/dev)

Figure 5.12 Laser output time profiles for mode switching speeds of (a) 1kHz, (b) 10kHz and (c) 20kHz. A volume Bragg grating was used to spectrally separate the output of the two modes with top row showing the $LP_{11\text{-doughnut}}$ component of the laser output and bottom row showing LP_{01} component.

The wavelength selectivity of the AOTF used in these experiments was less than that required to cleanly excite the individual two lobed modes of the LP_{11} peak. However by inserting an appropriately spaced Fabry–Pérot filter into the external feedback cavity along with the AOTF, it was possible to switch between either one of the two orthogonally orientated LP_{11} mode groups and the fundamental LP_{01} mode whilst still maintaining the electronic control of the AOTF arrangement. As the Fabry–Pérot filter has a periodic transmission band, we match this period (free-spectral-range) to the wavelength spacing between the LP_{01} and one of the LP_{11} peaks. This was experimentally realised by the construction of a variable separation Fabry–Pérot wavelength filter, consisting of two 90% reflective plane mirrors. One mirror was placed on a mechanical translation stage allowing course adjustment of mirror separation, with fine adjustment achieved by piezoelectric positioner. For a mirror separation of ~430µm the resulting free spectral range and double-pass spectral selectivity of 4.3nm and 0.07nm was achieved. This allowed the long wavelength 1921.9nm LP_{11} peak and 1926.2nm LP_{01} peak to be selected and switched. By decreasing the mirror separation of the Fabry–Pérot filter to

410µm it was also possible to select between the short wavelength 1921.7nm LP_{11} peak and the fundamental mode.

5.5 Incoherent combination of multiple mode superpositions

In this section we use the combination of MM-FBG and AOTF to simultaneously excite multiple modes within the thulium fibre cavity, demonstrating the arbitrary combination of LP_{01} modes and a doughnut shaped LP_{11} superposition with output powers of the order of 5W. Resulting in in-situ laser profile control from doughnut shaped to flat-toped to Gaussian.

In the background section of this chapter, we introduced several different techniques for the generation of flat-topped mode profiles. Whilst some of these approaches are very effective, they generally require the user to have a prior knowledge of the optimum beam profile for the application. Furthermore if the system is to be used for multiple applications, these mode selection and transforming elements must be changed or removed for optimum performance to be achieved. We can address this lack of flexibility by using the previously presented mode selection technique for the selection of superpositions of modes in addition to the selection of individual modes. By driving the AOTF with multiple simultaneous frequencies we can cause the external cavity to provide resonance for multiple wavelengths simultaneously, and hence with the previously described experimental arrangement, excite multiple fibre modes simultaneously. As these modes are offset in wavelength, the resulting superposition is incoherent removing any issues associated with pointing instabilities etc. as would be the case for a coherent superposition (as discussed in Chapter 4). By doing so we present a technique capable of the in-situ tailoring of a laser beam profile to best match a desired application.

5.5.1 Principle of operation

In the previous section we demonstrated the selection and switching of laser modes within the multimode thulium oscillator. Here by driving the AOTF with simultaneous RF frequencies (rather than switching between them) we can cause the cavity to oscillate on multiple fibre modes in a very controlled way. By adjusting the RF drive power of each of the RF channels we can also adjust the relative intensities of each of the excited

modes. This allows for the selection and controlled superposition of multiple modes within a multimode fibre laser.

A range of power combinations of fundamental and first higher order mode are plotted in Figure 5.13. In Figure 5.13(d) we show that an approximately flat-toped intensity profile results when the modal superposition contains 70% fundamental Gaussian mode and 30% two lobed LP_{11} mode.

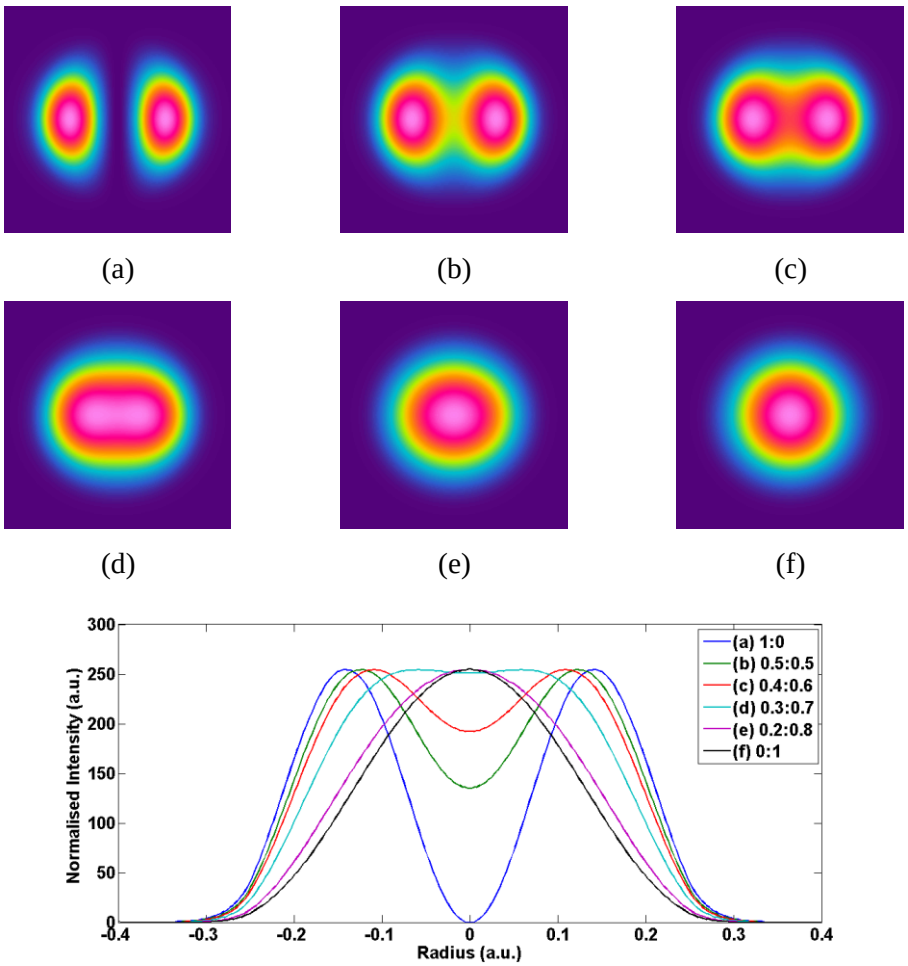

Figure 5.13 Theoretical beam profiles form the incoherent superposition of LP_{01} and LP_{11} fibre modes with modal intensity ratios of LP_{11} to LP_{01} of 1:0 (a), 0.5:0.5 (b), 0.4:0.6 (c), 0.3:0.7 (d), 0.2:0.8 (e), 0:1 (f) and a cross sectional view of these ratios in (g).

5.5.2 Experimental layout and results

Using the same experimental layout demonstrated in Section 5.4.3 (Figure 5.7) we take the core pumped cavity arrangement and drive this AOTF with a dual channel function generator (Tektronix AWG3102). This allows the AOTF to provide resonance for the fundamental LP_{01} (RF_{01}=30.0847MHz) and resonance for the LP_{11} group (RF_{11}=30.163MHz) simultaneously. By doing so, it is possible to excite an incoherent superposition of these modes within the multimode fibre laser cavity. By changing the relative drive power for each of the RF signals it is possible to control the relative intensities of these guided modes, allowing control of the 'flatness' or other parameters of the laser output beam. Figure 5.14 shows the effects of varying relative RF drive power whilst simultaneously providing resonance to both the LP_{01} and LP_{11} modes.

For a pump power of 17W an output power of above 5W was maintained across all modal power ratios. The relative power level of each mode group was directly measured using the same VBG spectral slicing technique mentioned in the previous section. With the relative modal power varied from complete $LP_{11\text{-doughnut}}$ to complete LP_{01}. The change in beam superposition was recorded as shown in Figure 5.14(a-f). Figure 5.14(d) shows the expected flat toped beam profile when 30% $LP_{11\text{-doughnut}}$ and 70% LP_{01} modes were excited.

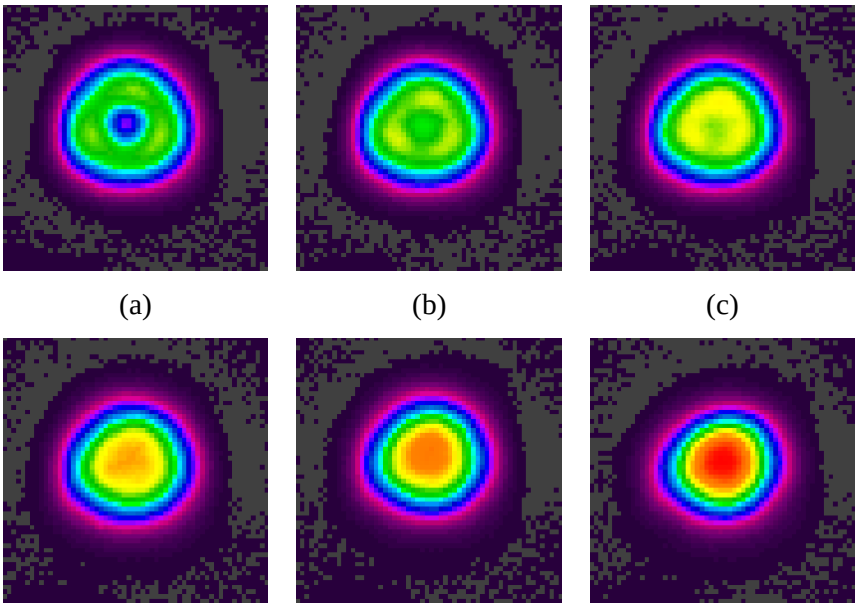

Figure 5.14 Laser output profile control using incoherent superpositions of LP_{01} and LP_{11} modes. Modal power ratios for $LP_{11\text{-doughnut}}$ to LP_{01} of 1:0 (a), 0.5:0.5 (b), 0.4:0.6 (c), 0.3:0.7 (d), 0.2:0.8 (e), 0:1 (f).

The broader spectral selectivity of the AOTF allowed the excitation of both LP_{11} mode peaks simultaneously with a single RF drive frequency. However if the individual two lobed mode profiles of the LP_{11} group are to be selected independently we must employ the use of additional wavelength selective elements. As detailed previously, we use appropriately spaced Fabry–Pérot filters to enhance the AOTF selectivity and allow the selection between the fundamental mode and long wavelength LP_{11} peak.

Again the relative power between excited modes could be completely controlled from 100% LP_{11} to 100% LP_{01} (See Figure 5.15). At an approximately 70/30 ratio between the LP_{01} and LP_{11} modes a flat toped elliptical superposition is formed (Figure 5.15(d)). For a pump power of 17W, 2.66W of output power was obtained at the LP_{11} mode. This reduction (of ~50%) in power in comparison to the $LP_{11\text{-doughnut}}$ case is due to an imperfect alignment of the FP filter arrangement resulting in a high insertion loss from the external feedback cavity. When a fused silica solid etalon of 0.5mm spacing and 90-90% reflectivity was used in combination with the AOTF to individually select the long wavelength LP_{11} peak up to 4.66 W was obtained at the same pump power. This is only a 12% reduction in comparison to the unfiltered case, demonstrating the ability to select this mode with high efficiency given a low loss spectral filter.

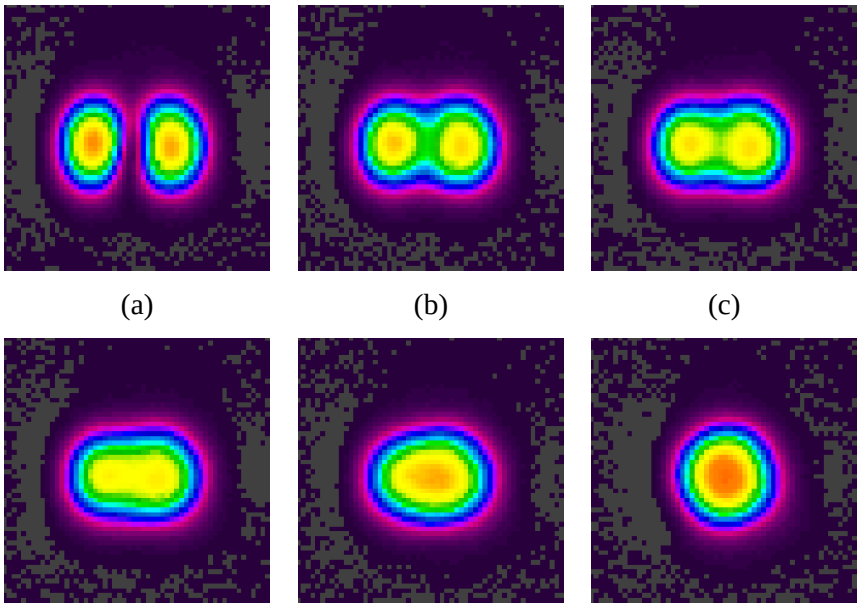

Figure 5.15 Laser output profile control using incoherent superpositions of LP_{01} and LP_{11} modes. Modal power ratios for LP_{11} to LP_{01} of 1:0 (a), 0.5:0.5 (b), 0.4:0.6 (c), 0.3:0.7 (d), 0.2:0.8 (e), 0:1 (f).

The normalised cross-sectional profiles of the modes obtained in Figure 5.15 are shown in Figure 5.16. Here we can see the variation in modal area when transitioning from LP_{01} to LP_{11}, as well as the approximately flat-toped profile of the 70/30 ratio of LP_{01} and LP_{11} modes.

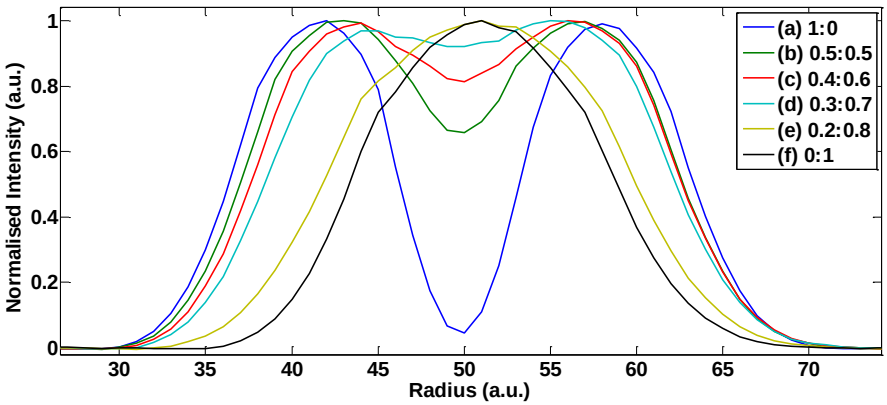

Figure 5.16 Measured cross-sectional profiles of the incoherent superpositions of the LP_{01} and LP_{11} modes.

5.5.3 Discussion

As is seen in Chapter 3, due to the close wavelength spacing of the LP_{01} and LP_{11} modes, to select these modes the resulting RF drive frequencies to the AOTF must be separated by sub MHz levels. This close frequency spacing brings the beat frequency of the two drive signals within the response time of the AOTF. Here the same modulation behaviour as shown in Chapter 3 is expected. This can been seen in time traces of the laser output, the beat frequency between RF_1 and RF_2 is shown in Figure 5.17.a with ~75kHz modulation. This same 75kHz modulation is seen on the laser output (Figure 5.17(b)). As discussed Chapter 3, suppression of this beating behaviour is possible through the use of a dual AOTF arrangement.

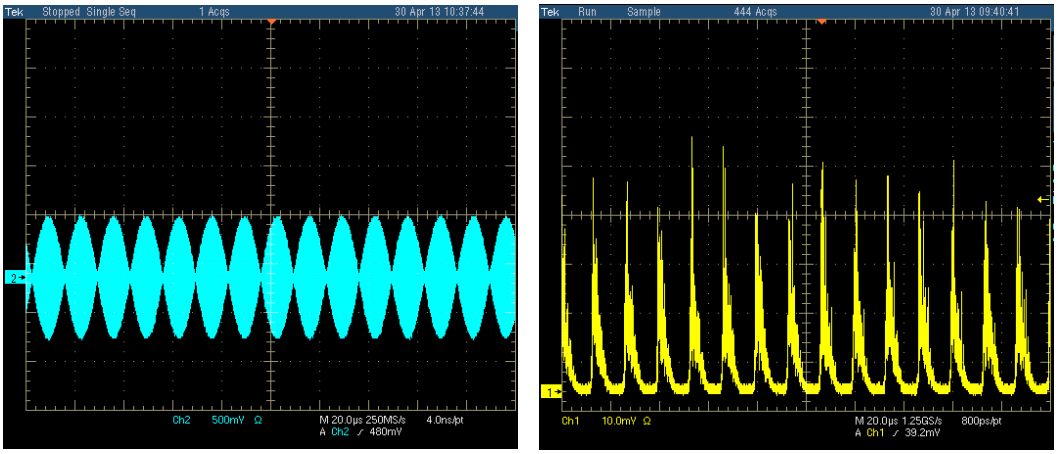

(a) (b)

Figure 5.17: (a) Oscilloscope trace of the combined 30.163MHz (LP_{11}) and 30.085MHz (LP_{01}) drive frequencies input into the AOTF, due to beating between these two frequencies an optical modulation of ~75kHz is seen.(b) The corresponding laser output profile for LP_{01} and LP_{11} selection of equal power.

Whilst the in-house built FP spectral filter allowed a significant increase in the spectral selectivity of the external cavity, its imperfect construction lead to an increased loss and reduced output power when selecting the LP_{01} & LP_{11} superpositions. Further improvements to output power can be achieved through the use of an appropriately spaced low-loss solid etalon.

5.6 Cladding pumped architecture for power scaling

For further power scaling of this technique it is desirable to move towards a directly diode pumped system where much higher pump powers can be achieved at a much lower cost per watt. Here we demonstrate a cladding pumped thulium fibre laser with a high power 793nm fibre-coupled diode pump. Initially we look at the modal behaviour in a cladding pumped system by analysing the emission spectra of a free running laser with a FBG for feedback. By monitoring the relative intensity of the individual FBG spectral peaks, information on the modal content of the free running laser can be obtained. We then extend this arrangement to a mode selective one through the use of an angle tuned VBG for wavelength selection. Whilst the use of a VBG in place of AOTF as the external cavity removes the dynamic control seen in the previous section it does still allow selection of modes through angle tuning of the VBG. For applications where only simple mode control rather than switching is desired this move to a passive cavity allows a reduction in parts count and has the potential for a very simple arrangement, consisting of only a lens and VBG for wavelength selection and output coupling.

5.6.1 Experimental layout

The multimode active fibre was cladding pumped with a 793nm fibre coupled diode source, and was launched into the TDF facet adjacent to the FBG with a launch efficiency of 90%, yielding a maximum available launched pump power of 33W. The cladding absorption coefficient for pump light at 793 nm was measured to be ~ 3dB/m resulting in an active fibre length of ~ 4m for efficient pump absorption. Feedback for lasing at the opposite end of the TDF was provided by a simple tunable external feedback cavity containing a VBG, high reflectivity plane mirror and an uncoated fused silica wedge. The 4% back reflection from the fused silica wedge provided laser feedback with the remaining light taken as the laser output. The VBG had a high reflectivity (>95%) at 1932nm at normal incidence to the grating and a reflection bandwidth of ~ 0.5nm (FWHM). This angle tuning arrangement (Figure **5.18**) allowed the resonance wavelength of the external cavity to be adjusted via rotation (of the VBG and plane mirror) to match the FBG resonance wavelength. The length of excess TDF between the FBG and pump launch was minimised to reduce wasted pump light with approximately ~ 5cm of active fibre between the FBG and angle cleave. The layout of this cavity is shown in Figure 5.18.

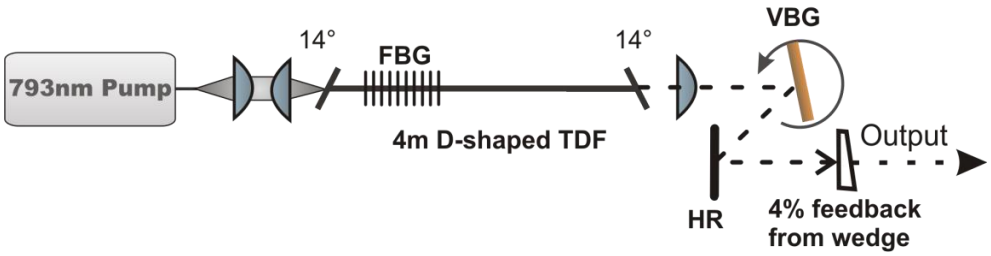

Figure 5.18 Experimental layout of cladding-pumped Tm-doped fibre laser.

5.6.2 Modal behaviour of free running cladding pumped TDF

Prior to operation as a mode selective cavity the VBG tuning arrangement was replaced by a flat cleave at the laser output and provided 4% broadband feedback via Fresnel reflection. Figure 5.19 shows the output spectra for this cladding pumped thulium laser at a range of signal output powers. The FBG was written at a fundamental mode resonance wavelength of 1923.3nm with an estimated reflectivity of 25%[4]. Due to the modal dependent behaviour of the FBG resonance wavelength we can use the relative intensities of the multi-peak laser spectrum to estimate the modal content of this free running fibre laser [34]. At low powers close to threshold (0.7W output) the fundamental mode appears to dominate, however as pump power is increased a larger number of modes are excited; with the LP_{11} peak (1919nm) and a mode conversion peak [8] (1921.2) demonstrating significantly higher powers than that of the fundamental. Note: for these spectral measurements a low resolution monochromator was used with a limited resolution of ~0.2-0.4nm and so the individual modal peaks for closely spaced modes were not resolved.

[4] This FBG was initially intended for use as laser output coupler (as discussed in Section 5.4.3), but due limited supply of high reflector fibre Bragg gratings this 25% reflector was repurposed as high reflector for these experiments.

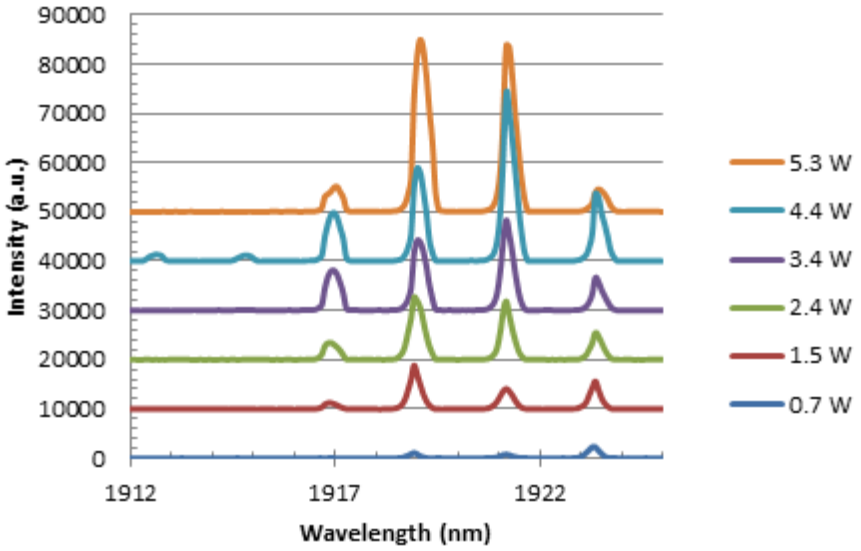

Figure 5.19 Spectral (modal) evolution of cladding pumped thulium fibre laser with MM Bragg grating and flat cleave for broadband feedback (offset for clarity).

In the previously presented core pumped experiments, the fundamental mode tended to dominate laser output power. This is due to an increased overlap between the single mode pump beam and the fundamental mode of the TDF. This lead to a lower threshold as well as better extraction efficiency near threshold for the fundamental mode. In this cladding pumped architecture, where a more uniform inversion distribution exists in the active fibre core, this preferential lasing on the fundamental mode is no longer the case. Here a more top-hat like inversion distribution is seen in the core that better favours the larger mode area of the LP_{11} close to threshold [35].

5.6.3 Mode selection in a cladding pumped Tm fibre laser

Under a free running configuration (with the VBG replaced by a high reflectivity plane mirror). The laser yielded a multimode output beam with a beam propagation factor (M^2) of ~ 3.3 (see Figure 5.20(a)). With the VBG present in the external cavity and aligned to provide feedback at 1923nm (i.e. to match Bragg wavelength for the LP_{01} for the FBG) lasing on only the fundamental (LP_{01}) mode was achieved. The beam propagation factor (M^2) was measured to be 1.05 confirming the diffraction-limited nature of the output beam (Figure 5.20(b)).

Angle tuning the VBG and realigning the HR plane mirror to match resonance for the next higher order mode allowed excitation of the LP_{11} mode as shown in Figure 5.20(c).

In this case the lasing wavelength was measured to be 1919nm, matching the peaks seen Figure 5.19 as expected.

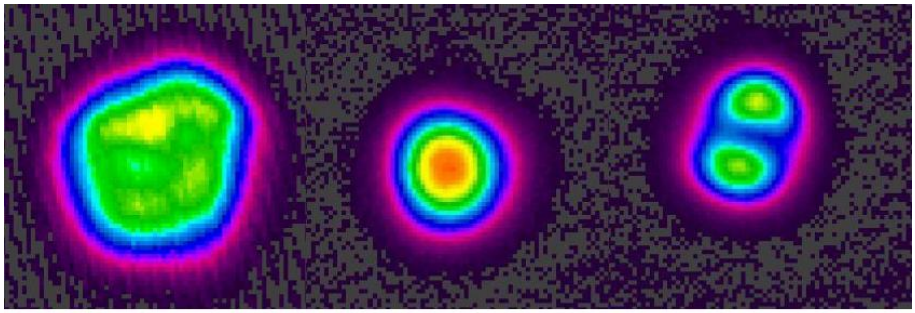

(a) (b) (c)

Figure 5.20 Output beam profile for: (a) Free running operation. (b) VBG tuned to 1923 nm to excite the LP01 mode. (c) VBG tuned to 1919 nm to excite the LP11 mode.

Figure 5.21 shows the output power for selection of either the LP_{01} or LP_{11} modes as a function of launched pump power. At the maximum launched pump power of ~ 34W the laser yielded output powers of 2.6W for LP_{01} mode operation and 3.6W for LP_{11} mode operation with corresponding slope efficiencies with the respect to launched pump power of 11% and 16% respectively. The higher output power and slope efficiency for LP_{11} mode selection was attributed to the better spatial overlap of the LP_{11} mode with the fibre inversion distribution [35]. Modelling conducted within the group [10] suggests that the difference seen in output power powers between the LP_{01} and LP_{11} modes reduces as pump power is increased to more times above threshold, eventually matching in output power for a sufficient number of times above threshold. Here as the intensity of the LP_{01} mode increases it is better able to extract inversion within the lower intensity wings of the Gaussian profile. However, due to a limited number of times above threshold this effect was not observable in these experiments.

The relatively low slope efficiencies for both LP_{01} and LP_{11} operation were attributed to the hydrogen loading process, which leads to a large increase in core propagation loss within the fibre at the lasing wavelength. The Tm fibre (with and without hydrogen loading) was tested in a simple free-running laser configurations and the slope efficiency for the TDF laser without hydrogen loading was found to be approximately 40%, roughly

a factor-of-two higher than for the TDF laser with hydrogen loading. The core propagation loss in the hydrogen-loaded TDF was estimated to be ~ 1dB/m.

It should also be noted that the TDF used in our experiments had a rather low Tm concentration and thus was not designed to enhance efficiency via promoting the 'two-for-one' cross-relaxation process (Chapter 2). Hence, further optimization of the core design with high Tm concentration should yield improvement in laser slope efficiency for a cladding pumped system.

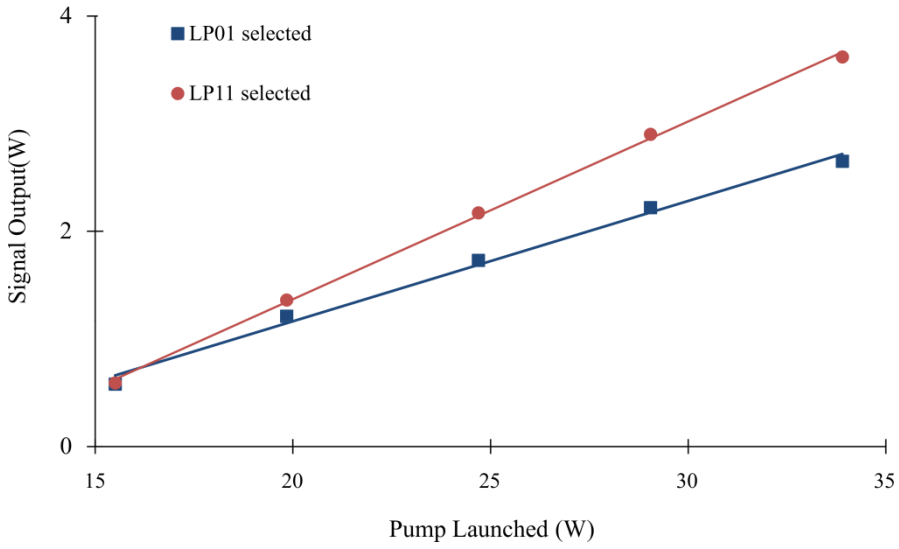

Figure 5.21 Laser output power versus launched pump power for LP_{01} and LP_{11} mode operation.

5.7 Future prospects

As the V-number of the multimode fibre is increased, the effective index spacing between neighbouring modes decreases. Reducing the effective index spacing between neighbouring modes has a number of important consequences that must be discussed if we are to get a good understanding of the core size scaling limits of this technique.

In the following sections we will investigate the scalability of this mode selection technique. Looking at the effects of increasing core size on wavelength separation between Bragg peaks as well as the increasing effects of mode coupling and bend distortion.

5.7.1 Mode separation with increasing core size

From eq.(34) we can see, for a fixed Bragg period, the wavelength separation between neighbouring modes is given by:

$$\Delta\lambda = 2\Delta n_{eff}\Lambda_{FBG} \tag{39}$$

where $\Delta n_{eff} = min(n_{eff}^{m} - \Delta n_{eff}^{m\pm1})$ i.e. the minimum index spacing between neighbouring modes. From this we can see a decreased effective index spacing will lead to a reduction in the wavelength spacing between reflection peaks of the FBG. To give an idea of the magnitude of this effect, the effective index separation between the LP_{11} and LP_{01} modes was calculated (Optifibre) for a fibre with fixed NA (0.20) and increasing core diameter. We then used these calculated values to plot the wavelength separation between the two guided modes for increasing core area (shown in Figure 5.22).

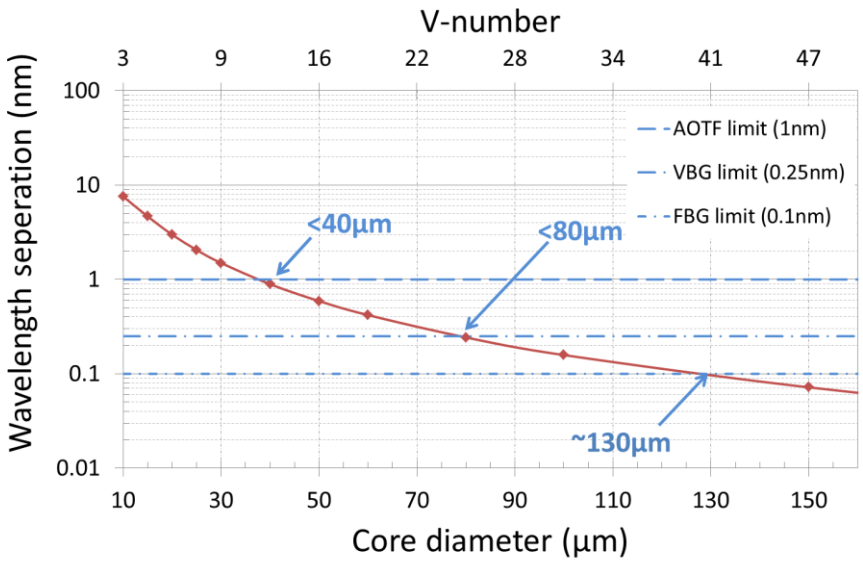

Figure 5.22 Wavelength separation of Bragg resonance between the LP_{01} & LP_{11} modes for a FBG written in to a 0.20NA step index fibre and central wavelength of 2µm.

On top of this plot we mark the various resolution limits of the individual wavelength selective elements used in our experiments, 1nm represents the resolution limits of the AOTF used (when in a double pass configuration), 0.25nm represents the resolution limit of the VBG (again in a double pass configuration). As both of these resolution limits can

be circumvented by the use of an etalon filter (as demonstrated in Section 5.4.3) we place a third limit, 0.1nm, based on a realistically achievable FBG reflection bandwidth. From this we find upper core diameters of 40µm (V-number ~ 12), 80µm (V-number ~ 25) and 130µm (V-number ~40) for the wavelength selectivity of AOTF, VBG and FBG respectively.

As we will see in the coming sections, effects such as mode coupling and bend induced mode distortion can place upper scaling limits before FBG limitations are reached. This analysis also assumes ideal, uniform FBG inscription across the width of the fibre core, in practice this might be a challenging prospect and effects such as grating non-uniformity will also have to be taken into account [8].

5.7.2 The effects of mode coupling

As has been demonstrated within this work, it is possible for a single transverse mode to propagate within a multimode fibre. However, there are certain constraints that must be met if modal purity is to be maintained. The effects of mode coupling, and ultimately our ability to maintain power within the selected mode, are dependent on wavelength, core and cladding size and fibre uniformity. For single mode excitation of a multimode fibre, the power contained within a single mode of a straight length of fibre after a distance of z(m) and due to mode coupling effects can be approximated by [36]:

$$\eta(z) = \left(1 + \frac{16 d_{core}^2 D z}{\lambda^2}\right)^{-1} \tag{40}$$

where $d_{core}(m)$ is the fibre core diameter and $D(rad/m^2)$ is the mode coupling coefficient. Generally *D* should be experimentally measured for reliable values. However, for the purposes of this analysis we will use some very rough approximations to gain insight to the scaling behaviour of *D*. Although the scaling behaviour for *D* as given by Fermann shows strong dependence on core diameter and wavelength [36], more recent studies suggest a slightly weaker dependence with *D* proportional to [37]:

$$D \propto \frac{d_{core}}{d_{clad}^2 \lambda^{1/2}} \tag{41}$$

From this dependence we can see increasing cladding diameter should have a strong effect on the limiting of mode coupling. Longer operating wavelengths as well as reduced

core diameter also have beneficial effects on reducing the effects of mode coupling. For the following section it is convenient to rearrange eq.(40) in terms of an upper propagation length limit for a given mode degradation:

$$z_{max} = \left(\frac{1}{x} - 1\right)\frac{\lambda^2}{16 d_{core}^2 D} \tag{42}$$

Where *x* is the maximum permissible power loss to other modes, i.e. for x=1-1/e^3, ~95% of the power will still be contained with the launched mode after propagating a length z_{max} along the fibre.

Taking an estimate of *D* from published literature [37] and scaling for wavelength, core and clad diameters from eq.(41) we can get a very rough estimate of the mode coupling behaviour across core size and wavelength. In Figure 5.23 we plot the estimated propagation length before 5% of the propagating mode is coupled to higher order modes, this is shown over a range of wavelengths.

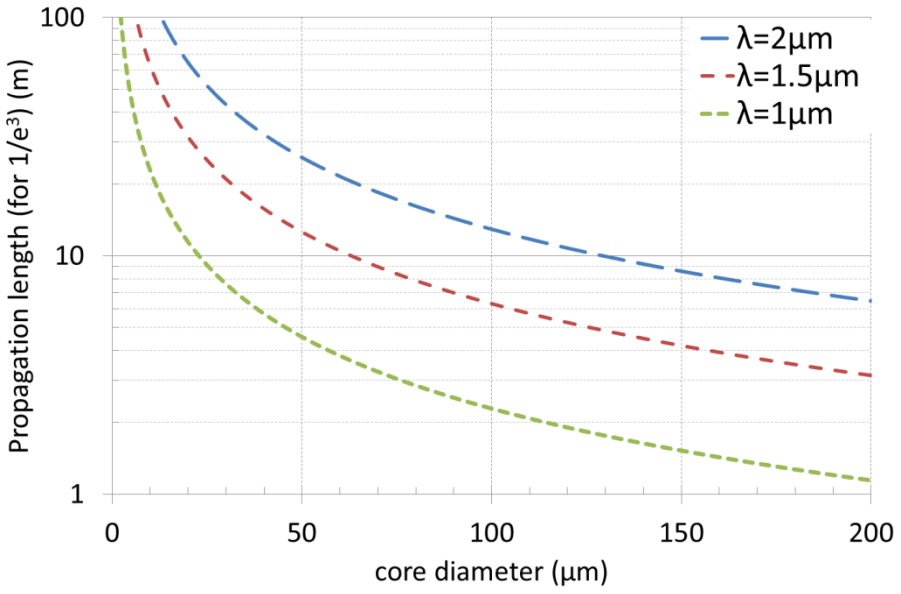

Figure 5.23 The achievable propagation length before power contained within the fundamental mode drops to ~95% of its initial value (for a step index fibre with a 0.20NA, and fixed core-to-clad ratio of 10, coupling coefficient *D* was scaled from eq.(41)

From this we can see it is possible to maintain mode quality in a multimode fibre providing the level of microbending is sufficiently low and fibre length is kept short.

However, even for an extremely uniform fibre, as the core size is scaled mode coupling will eventually become an issue, limiting the scalability of this technique.

The above treatment highlights the trends of increasing mode coupling for increasing V-number or decreasing wavelength, but can only be used as a very rough guide. For accurate predictions of propagation length, fibre parameters such as *D* have to be experimentally obtained. In practice the mode selection technique presented in this work may actually provide a simple way to quantify the real world effects of mode coupling.

5.7.3 Fibre Bragg gratings in large mode area fibre

There are some unanswered questions related to the axial uniformity achievable with Bragg gratings fabricated through side exposure with UV light. To maximise grating strength, in fibre Bragg gratings are generally written by a UV light source at an operating wavelength of 244nm. Due to the finite absorption depth of this wavelength within the fibre core, some degree of grating strength asymmetry is seen during grating manufacture. This asymmetry manifests itself as an increased loss within the grating through scattering and mode coupling and can also be seen in an increased polarisation dependence. Lu et al [8] modelled the behaviour of this effect within a two mode optical fibre and found increased grating asymmetry led to the generation of a third reflection peak. The location of this peak is equal to half the effective index spacing of the two guided modes. This peak is referred to as the cross coupling peak and can be thought of as a mode coupling effect due to a tilted Bragg grating. The gratings used within the experimental section of this chapter also showed this cross coupling peak (Figure 5.19). Within a passive fibre it is possible to use the relative strength of this peak to infer the asymmetry of the FBG. However within the active fibre used in our experiments this was not possible due to the possibility of spatially dependent absorption and gain within the active fibre. As core diameter is scaled, the sensitivity and severity of this effect is also increased. A upper limit on core size may be imposed by the achievable FBG uniformity across the core.

A possible solution to this can be found in the use femtosecond pulse FBG writing [38]. Here rather than relying on fibre photosensitivity, nonlinear interaction between high peak power incident pulses and the optical fibre lead to a refractive index modification and can be used for FBG inscription. Due to the non-linear absorption behaviour of this

process, FBG inscription can be achieved with high uniformity and is an interesting route to investigate should UV inscription become problematic.

5.7.4 Bend-induced mode distortion

As an optical fibre is bent, a distortion of the fibre mode profile can occur. This is due to an induced phase delay across a bent fibre's core when compared to the case of a straight fibre. For small core fibres this effect can be negligible, but as core size is increased this effect starts to have a significant impact on effective mode area of the guided modes with the potential to result in a poor overlap with gain within the active fibre as well as reducing the thresholds for detrimental nonlinear processes [39–41]. Examples of bend induced mode distortion can be seen in Figure 5.24 for a step index fibre with NA=0.2 and core diameter of 20μm, Profiles were calculated using commercially available software (Comsol).

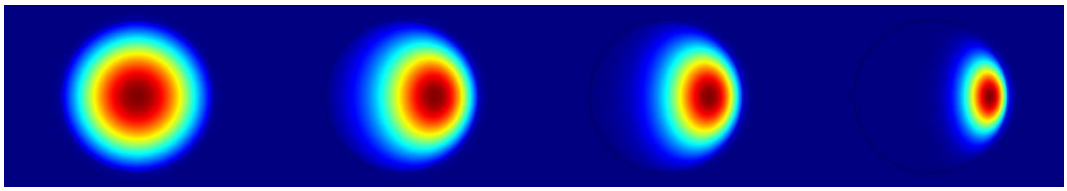

(a) (b) (c) (d)

Figure 5.24 The effects of fibre bend on fundamental mode profile, for unbent fibre (a) R_{bend}=50cm, (b) R_{bend}=10cm, (c) R_{bend}=5cm, (d) R_{bend}=1cm.

The bending of an optical waveguide can be analogous to introducing a refractive index slant across the core of the optical fibre [42]. With the resulting equivalent fibre refractive index profile given by:

$$n_{eq}(x,y) = n_0(x,y)\left(1 + \frac{x}{R_{bend}}\right) \tag{43}$$

where n_0 is the initial unbend index profile and R_{bend} is the effective fibre bend radius. Stress induced refractive index change within the glass can be accounted for by scaling R_{bend} as R_{bend}=1.27R [43] where R is the physical bend radius of the fibre. The resulting equivalent refractive index profile in comparison to an unbent fibre is shown conceptually in Figure 5.25. Following the treatment given in [42], we can gain a more intuitive understanding of bend induced mode distortion by first defining several parameters. The refractive index height of the core above the effective index of the guided mode as

$\Delta n_{eff}=n_{core}-n_{eff}$. The maximum increase in core refractive index due to bending as $\Delta n_{bend}=n_{core}r_{core}/R_{bend}$. These two parameters are marked in Figure 5.25, where the unbent fibre refractive index (black) is shown against the bent refractive index (red dashes). In this picture when $\Delta n_{bend} > \Delta n_{eff}$ a depressed region of refractive index that is less than the guided modes effective index is seen (grey shaded area). Within this area the mode cannot propagate and must reduce in area, moving towards the outside of the fibre bend. Whilst this is an oversimplification it does convey the behaviour of bend induced mode distortion.

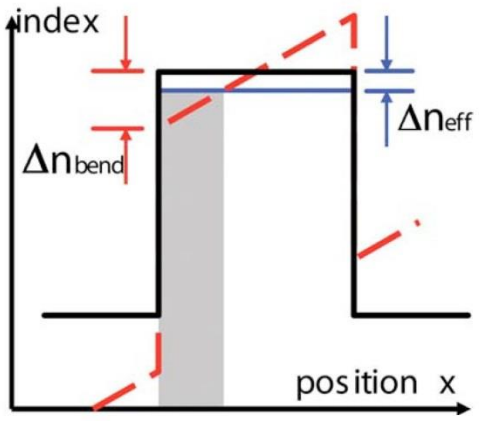

Figure 5.25 Equivalent bent refractive index profile (red dash) superimposed over the unbend index profile (black). The region shaded in grey represents a forbidden region for mode propagation [42].

From this we can define the value of R_{bend} when $\Delta n_{bend} = \Delta n_{eff}$ as the onset of mode distortion i.e.:

$$R_{bend-min} = \frac{n_{core}r_{core}}{\Delta n_{eff}} \tag{44}$$

When plotted against the normalised mode area (ratio of bent and unbend mode area) for several strongly guiding fibres it is found that this value $R_{bend\text{-}min}$ closely predicts the point at which the mode area drops to about 90% of its initial value. Further following the work in [42] we can approximate the value for Δn_{eff} within a strongly guided fibre as:

$$\Delta n_{eff} = \frac{\lambda^2}{8.8 n_{core} A_{eff}^{o}} \tag{45}$$

where A_{eff}^{o} is the effective area of the unbend fibre mode. From eq.(45) we can then gain an estimate of the minimum bend radius $R_{bend\text{-}min}$ as:

$$R_{bend-min} \approx \frac{8.8 n_{core}^{2} A_{eff}^{o} r_{core}}{\lambda^{2}} \tag{46}$$

From eq.(46) we can easily estimate the minimum bend radius of a strongly guided fibre (i.e. a fibre where bend loss can be neglected) for which mode distortion is expected to become a problem for a given core diameter and wavelength.

Figure 5.26 shows the result of these calculations for a 0.20NA fibre at a range of wavelengths and coil sizes. As reported previously for reasonable coil sizes (R=20-40cm) the fibre core diameter is limited to around 40-50µm when working at a wavelength of λ=1µm. We note that for the same coil size, moving to longer wavelengths, i.e. λ=2µm there is a ~60% increase in core diameter to 60-80µm before the same level of mode distortion will occur. It is important to mention that the above treatment is for step index fibre operating on the fundamental mode. There exist several techniques to further increase core size whilst maintaining a tolerance to mode distortion. Strategies include the use of tailored index profiles such as parabolic [42] or W-type fibre.

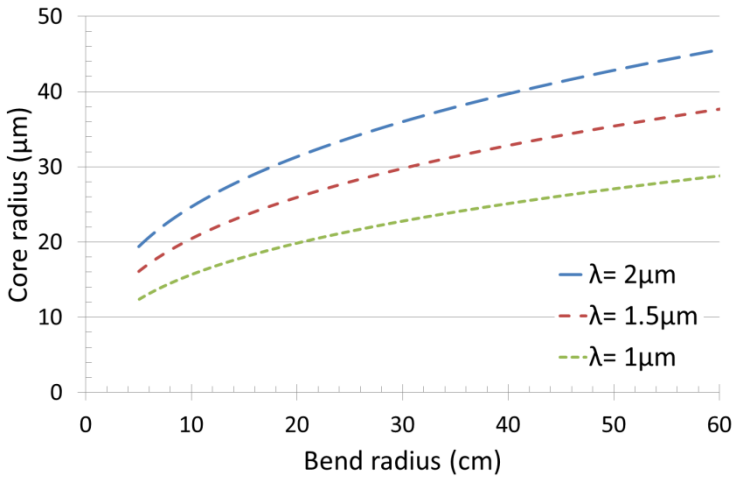

Figure 5.26 Expected core size limits for undistorted mode propagation ($A_{eff}>0.9*A_{eff}^{0}$) at a given bend radius. Core sizes above this limit will experience noticeable mode distortion and reduced effective area.

5.7.5 Higher order mode selection

The multimode fibre used in these experiments demonstrated close effective index spacing between higher order modes and resulted in close wavelength spacing on the reflection spectrum of the FBG. Due to a reflection bandwidth of approximately 0.2nm this resulted in a mode spacing (in wavelength) that was less than the FBG bandwidth for modes higher than the LP_{11} and excluded the clean excitation of these higher order modes. Through the use of smaller bandwidth FBG's it should be possible to excite higher order modes with this cavity arrangement. This will allow the selection and combination of other novel superpositions as well as higher order modes that possess larger effective areas and can show grater resistance to mode skew [4].

Although in the above experimental demonstrations operation on radially or azimuthally polarised modes was not possible, through the use of circularly symmetric fibre it is possible to guide and excite fibre mores with radial or azimuthal polarisation [44,45].

5.8 Conclusion

In this chapter we have introduced and successfully demonstrated a novel mode selection technique based on the differing spectral responses of in-fibre Bragg gratings and free space wavelength selective elements. Demonstrating for the first time, to the best of our knowledge, the rapid selection and switching between transverse modes in a multimode fibre laser oscillator.

We first introduced the concept of the mode selection technique, highlighting the difference in threshold between the selected mode and other propagating modes. We then successfully demonstrated the validity of this technique in a core pumped multimode thulium fibre laser. Using a FBG as a high reflector and an electronically controllable AOTF we demonstrated the selection of the fundamental mode and next higher order mode in a multimode oscillator with output powers of greater than 5W and laser slope efficiencies of approximately 40%. The measured beam quality for the fundamental and doughnut shaped LP_{11} superposition were M^2=1.07 and M^2=2.2 respectively. By switching the RF drive frequency to the AOTF it was possible to switch between the guided modes at switching frequencies of up to 20kHz. We enhanced the wavelength selectivity of the external cavity by introducing an additional wavelength selective

element in the form of an etalon of variable air gap spacing. By matching the air gap to that of the wavelength separation of the fundamental and either of the two LP_{11} modes, it was possible to individually select and switch between these modes. Thus circumventing the resolution limitations of the AOTF whilst still allowing active selection and switching between modes.

Detailing the flexibility of mode of operation with this technique, we use the incoherent superposition of the fundamental and doughnut shaped LP_{11} mode to generate beam profiles with variable shape and electronically selectable parameters such as beam flatness. This was achieved by driving the AOTF with two simultaneous RF drive signals, matched in frequency to that of the fundamental and LP_{11} modes. By changing the RF drive power of each of the signals, we can effectively control the relative power of each of these modes. The ability to control mode profile and shape as well as switch between modes at very rapid rates represents a new degree of flexibility of operation within a multimode fibre laser. Such switching of profile can be likened to the changing of a tool-head within a mechanical processing system and may allow higher performance and more efficient laser marking and processing applications.

To demonstrate the power scalability of this technique we move away from a core pumped system, where pump and fundamental mode overlap are favourable, to a cladding pumped architecture. This allows the use of high power laser diodes for power scaling within a double clad arrangement. We constructed a laser cavity containing multimode FBG and VBG in an angle tuning configuration. By angle tuning the VBG we were able to select the resonance wavelength of the external cavity and thus select the oscillating mode. In a resonator without wavelength selection (i.e. broadband feedback) the laser oscillated on multiple simultaneous modes with an output beam quality of M^2=3.3. However by introducing the wavelength selective VBG, fundamental-mode operation was achieved with output beam quality of M^2=1.05.

In the final section of this chapter we looked further ahead, analysing the various parameters associated with core area scaling. We show that for an increasing core area the wavelength separation between FBG resonances decreases. This effect was quantified in Figure 5.22 where we plot the wavelength spacing of the LP_{01} and LP_{11} modes. For our current fibre, we find a wavelength resolution of 0.25nm allows mode selection for a core size of up to ~70μm. By putting an upper limit associated with practical FBG bandwidth

we find a maximum core diameter of 130µm before overlap between the resonance wavelength for the fundamental and next higher order mode occurs.

We roughly estimate the effects of mode coupling within this arrangement and highlight the importance of large cladding diameters and short device lengths. Looking at the effects of mode distortion within such large core fibres we find an upper limit of ~ 70µm core diameter (at a wavelength of 2 µm) before mode skew effects become significant due to fibre bend.

Using a simple ratio of feedbacks between the selected mode and feedback from the angle cleaved end-facet, we were able estimate the difference in threshold between the selected mode and non-selected modes within a multimode oscillator. From our simple calculations, we found this difference in thresholds of approximately 6 times that of the selected mode. Discussing the selection of Gaussian modes, we highlighted previous work suggesting that this level of threshold suppression (of higher order modes) should allow strong saturation of inversion before the onset multimode operation. Experimentally, we saw no evidence of the onset of higher order modes or parasitic lasing within the fibre diameter used.

Many of the investigated parameters are not hard limits, but rather variables that can be traded off. For core diameters of up to ~70um it is expected fundamental mode operation is possible with a manageable fibre bend radius. For increasing fibre core diameter rod type fibre designs seem attractive. The short device lengths and large cladding diameters are beneficial from a mode coupling perspective and when kept straight the effects of mode skew can be neglected. Such oscillator designs would pave the way for a simple Q-switched Tm fibre laser oscillator with pulse energies in the multi-millijoule regime and beyond. Moreover, the ability to selectively excite higher order modes with larger transverse dimensions than the fundamental mode should help to improve extraction efficiency and raise energy damage thresholds opening up the prospect of even higher pulse energies.

References

1. V. Niziev and A. Nesterov, "Influence of beam polarization on laser cutting efficiency," J. Phys. D. Appl. Phys. **32**, 1455 (1999).

2. M. Meier, V. Romano, and T. Feurer, "Material processing with pulsed radially and azimuthally polarized laser radiation," Appl. Phys. A **86**, 329–334 (2006).

3. S. Ramachandran, J. M. Fini, M. Mermelstein, J. W. Nicholson, S. Ghalmi, and M. F. Yan, "Ultra-large effective-area, higher-order mode fibers: a new strategy for high-power lasers," Laser Photonics Rev. **2**, 429–448 (2008).

4. J. M. Fini and S. Ramachandran, "Natural bend-distortion immunity of higher-order-mode large-mode-area fibers," Opt. Lett. **32**, 748 (2007).

5. F. Havermeyer, "Volume holographic grating-based continuously tunable optical filter," Opt. Eng. **43**, 2017 (2004).

6. T. Mizunami, T. V. Djambova, T. Niiho, and S. Gupta, "Bragg gratings in multimode and few-mode optical fibers," J. Light. Technol. **18**, 230–235 (2000).

7. B. J. Eggleton, C. Kerbage, P. Westbrook, R. Windeler, and A. Hale, "Microstructured optical fiber devices," Opt. Express **9**, 698–713 (2001).

8. C. Lu and Y. Cui, "Fiber Bragg grating spectra in multimode optical fibers," J. Light. Technol. **24**, 598–604 (2006).

9. W. A. Clarkson, "SC270 High Power Fiber Lasers and Amplifiers," in *CLEO Short Course Series* (CLEO, 2009).

10. J. S. P. Chan, "Power scaling concepts in fiber lasers and amplifiers," Doctoral Thesis, University of Southampton (2011).

11. J. Bovatsek and R. S. Patel, "High-power, nanosecond-pulse Q-switch laser technology with flattop beam-shaping technique for efficient industrial laser processing," www.newport.com/images/webdocuments-en/images/29436.pdf (2007).

12. M. Duocastella and C. B. Arnold, "Bessel and annular beams for materials processing," Laser Photonics Rev. **6**, 607–621 (2012).

13. N. Sanner, N. Huot, E. Audouard, C. Larat, and J.-P. Huignard, "Direct ultrafast laser micro-structuring of materials using programmable beam shaping," Opt. Lasers Eng. **45**, 737–741 (2007).

14. C. Zhang, N. R. Quick, and a Kar, "Pitchfork beam shaping for laser micorvia drilling," J. Phys. D. Appl. Phys. **41**, 125105 (2008).

15. D. Zeng, "Annular beam shaping and optical trepanning," Doctoral Thesis, University of Central Florida (2006).

16. Q. Zhan, "Cylindrical vector beams: from mathematical concepts to applications," Adv. Opt. Photonics **1**, 1 (2009).

17. M. R. Taghizadeh, P. Blair, B. Layet, I. M. Barton, a. J. Waddie, and N. Ross, "Design and fabrication of diffractive optical elements," Microelectron. Eng. **34**, 219–242 (1997).

18. R. Voelkel and K. Weible, "Laser beam homogenizing: limitations and constraints," Opt. Syst. Des. (2008).

19. D. Lin, S. U. Alam, a. Malinowski, K. K. Chen, J. R. Hayes, J. C. Flannagan, V. Geddes, J. Nilsson, S. Ingram, S. Norman, and D. J. Richardson, "Temporally and spatially shaped fully-fiberized ytterbium-doped pulsed MOPA," Laser Phys. Lett. **8**, 747–753 (2011).

20. O. Homburg, D. Hauschild, F. Kubacki, and V. Lissotschenko, "Efficient beam shaping for highpower laser applications," Laser Tech. J. **4**, 44–47 (2007).

21. F. K. Fatemi and M. Bashkansky, "Generation of hollow beams by using a binary spatial light modulator," Opt. Lett. **31**, 864–6 (2006).

22. T. Cižmár and K. Dholakia, "Exploiting multimode waveguides for pure fibre-based imaging," Nat. Commun. **3**, 1027 (2012).

23. D. Flamm, C. Schulze, D. Naidoo, S. Schroter, A. Forbes, and M. Duparre, "All-Digital Holographic Tool for Mode Excitation and Analysis in Optical Fibers," J. Light. Technol. **31**, 1023–1032 (2013).

24. K. Yonezawa, Y. Kozawa, and S. Sato, "Generation of a radially polarized laser beam by use of the birefringence of a c-cut Nd:YVO4 crystal," Opt. Lett. **31**, 2151 (2006).

25. S. Ngcobo, I. Litvin, L. Burger, and A. Forbes, "A digital laser for on-demand laser modes," Nat. Commun. **4**, 2289 (2013).

26. J. Bisson, Y. Senatsky, and K. Ueda, "Generation of Laguerre-Gaussian modes in Nd: YAG laser using diffractive optical pumping," Laser Phys. Lett. **333**, 327–333 (2005).

27. J. W. Kim, J. I. Mackenzie, J. R. Hayes, and W. A. Clarkson, "High power Er:YAG laser with radially-polarized Laguerre-Gaussian (LG_01) mode output," Opt. Express **19**, 14526 (2011).

28. J. M. Daniel and A. Clarkson, "Generation of pseudo-radially-polarized beams in a diode-pumped solid-state laser," in *Conference on Lasers and Electro-Optics* (2012), p. CM1D.4.

29. J. Kim, C. A. Codemard, J. Nilsson, and J. Sahu, "Erbium-ytterbium co-doped hollow optical fibre laser," Electron. Lett. **42**, 5–6 (2006).

30. S. Ramachandran, J. W. Nicholson, S. Ghalmi, M. Yan, P. Wisk, E. Monberg, and F. Dimarcello, "Light propagation with ultralarge modal areas in optical fibers," Opt. Lett. **31**, 1797–1799 (2006).

31. S. Ramachandran, P. Kristensen, and M. F. Yan, "Generation and propagation of radially polarized beams in optical fibers.," Opt. Lett. **34**, 2525–7 (2009).

32. R. Kashyap, *Fiber Bragg Gratings* (Academic Press, 1999), p. 458.

33. A. W. Snyder and W. R. Young, "Modes of optical waveguides," J. Opt. Soc. Am. **68**, 297 (1978).

34. F. Stutzki, C. Jauregui, J. Limpert, and a. Tünnermann, "Real-time characterisation of modal content in monolithic few-mode fibre lasers," Electron. Lett. **47**, 274 (2011).

35. M. Gong, Y. Yuan, C. Li, P. Yan, H. Zhang, and S. Liao, "Numerical modeling of transverse mode competition in strongly pumped multimode fiber lasers and amplifiers," Opt. Express **15**, 3236–46 (2007).

36. M. E. Fermann, "Single-mode excitation of multimode fibers with ultrashort pulses," Opt. Lett. **23**, 52 (1998).

37. S. Hurand, L.-A. Chauny, H. El-Rabii, S. Joshi, and A. P. Yalin, "Mode coupling and output beam quality of 100-400 μm core silica fibers," Appl. Opt. **50**, 492–9 (2011).

38. J. Thomas, E. Wikszak, T. Clausnitzer, U. Fuchs, U. Zeitner, S. Nolte, and A. Tünnermann, "Inscription of fiber Bragg gratings with femtosecond pulses using a phase mask scanning technique," Appl. Phys. A **86**, 153–157 (2006).

39. J. W. Nicholson, J. M. Fini, A. D. Yablon, P. S. Westbrook, K. Feder, and C. Headley, "Demonstration of bend-induced nonlinearities in large-mode-area fibers," Opt. Lett. **32**, 2562–4 (2007).

40. J. M. Fini, "Design of large-mode-area amplifier fibers resistant to bend-induced distortion," J. Opt. Soc. Am. B **24**, 1669 (2007).

41. R. T. Schermer, "Mode scalability in bent optical fibers," Opt. Express **15**, 15674–15701 (2007).

42. J. M. Fini, "Intuitive modeling of bend distortion in large-mode-area fibers," Opt. Lett. **32**, 1632–4 (2007).

43. A. B. Sharma, A. H. Al-Ani, and S. J. Halme, "Constant-curvature loss in monomode fibers: an experimental investigation," Appl. Opt. **23**, 3297 (1984).

44. C. Jocher, C. Jauregui, C. Voigtländer, F. Stutzki, S. Nolte, J. Limpert, and A. Tünnermann, "Fiber based polarization filter for radially and azimuthally polarized light," Opt. Express **19**, 19582–19590 (2011).

45. C. Jocher, C. Jauregui, and M. Becker, "An all-fiber Raman laser for cylindrical vector beam generation," Laser Phys. Lett. **201101**, 201101 (2013).

Chapter 6.

Conclusion

Thulium fibre lasers offer a platform for high output power and broad wavelength flexibility within the two-micron wavelength band. Throughout this thesis we demonstrate a wide range of operating parameters using a thulium host, investigating wavelength and mode control in several different architectures. In this chapter we summarise the key results of this thesis providing a conclusion to the works undertaken.

In Chapter 3, investigating the broad emission band of the $^3F_4 - {}^3H_6$ transition within silica, we demonstrate wavelength tunability over a 450nm range. Over this wavelength span thulium emission transfers from quasi-three-level behaviour at short operating wavelengths through to more four-level behaviour at long wavelength emission. This behaviour is highlighted through the comparison of a low dopant concentration, core pumped sources and higher dopant concentration cladding pumped sources. Where, moving from the high excitation densities seen in core pumping to the lower excitation density from cladding pumping architectures resulted in a shift of the wavelength tuning range from ~1700-1900nm up to ~1900-2100nm.

Through use of an acousto-optic tunable filter (AOTF) in core and cladding pumped architectures, we have demonstrated a highly reconfigurable and tunable fibre source that shows the ability to operate on multiple simultaneous wavelengths. Through the spectral combination of the two gain stages into a single output we present a novel way forward for a broadly tunable two-micron laser source, with the potential to cover >400nm wavelength range at Watt level output powers and spectral linewidths of <0.1nm. Such a source would be a very attractive tool for work in this difficult to reach wavelength range as well a useful device for further power scaling and frequency conversion.

Exploring the short wavelength limits of the thulium emission band, we constructed a compression tuned fibre Bragg grating feedback arrangement and demonstrate the

remarkably short operation down to 1660nm. This tunable source highlights the feasibility of several short wavelength applications, such as the high brightness pumping of Dy:fluoride fibre for access into the mid infrared [1]. Finally, completing our investigation into wavelength coverage within a Tm:silica host, we demonstrated two fixed wavelength sources. These were based on high feedback efficiency fibre Bragg gratings with operating wavelengths of 1726nm and 1950nm. These sources were able to generate output powers of 12.6 and 14W respectively for 20.9W of launched pump light and showing laser slope efficiencies of 67% and 72% with respect to absorbed pump power. This first demonstration of high power and high efficiency 172xnm operation is of particular interest. With applications in laser materials processing of polymers [2] as well as in the potentially lucrative medical sector [3] and should attract interest from the commercial sector.

Continuing the theme of spectral control, in Chapter 4 we demonstrate the efficient generation of high peak power ASE light, through the fast feedback switching of a high gain fibre cavity. By introducing external cavity wavelength selective elements we demonstrate spectral bandwidth control, with output bandwidths from 24nm FWHM down to 0.7nm FWHM, without significant change in output power or pulse energy. Wavelength tunability of this source was from 1785nm to 1935nm. Output pulses showed a high degree of stability with pulse-to-pulse energy variance of only ~0.25%. Peak powers of 2.2kW were obtained within a 29ns pulse at pulse repetition rates of 125kHz. For increased pulse frequency, up to 10.3W of pulsed ASE output power was obtained at a slope efficiency of 63%. As this pulsed ASE source essentially behaves as a self-seeded multi-pass amplifier, by applying spectral filtering to the initial back-reflected wavelengths a broad degree of spectral control is possible and has initially been demonstrated. A promising route for future work on this source is through the addition of highly configurable wavelength control to the external cavity. By replacing the HR mirror and slit arrangement with a digital micromirror device (DMD), the operating wavelengths of the ASE source could each be addressed individually. This allows the emitted spectral envelope shape to be defined at up to the diffraction grating resolving power (~0.7nm in the current configuration) and should allow the generation of novel spectral envelope shapes, such as flat-toped or saw-toothed profiles.

In the second half of Chapter 4, we apply this pulsed ASE source to both the suppression of modal interference within a multimode amplifier and to the generation of broadband

supercontinuum light within a small core highly nonlinear fibre. By moving to larger active core areas pulse energy storage within the fibre can be increased and the effects of detrimental nonlinear processes can be reduced. Achieving core area scaling within a single mode fibre can be challenging particularly as core area is significantly increased. Relaxing the need for single mode guidance and moving to slightly multimode output can allow large gains in pulse energy, and greatly simplifies fibre design. However, when propagating on multiple modes within a multimode optical fibre, interference between these modes can lead to unstable beam profiles and intensity hotspots. By increasing the spectral bandwidth of the seed source we successfully suppressed these detrimental effects, generating a stable multimode beam profile that showed little sensitivity to fibre movement or heating. Although primarily intended as a demonstration of modal interference suppression, this source also operated with reasonable pulse energies, at up to 1.1mJ obtained with peak power of 20kW. As was discussed in the background section of Chapter 4, as well as demonstrated within passive fibre, this technique can be applied to much larger fibre core areas and should allow significant scaling of laser pulse energies.

By moving to smaller core areas with tight mode confinement we lower the threshold for nonlinear processes and successfully generate supercontinuum light spanning greater than an octave, from 1000nm to >2400nm. This ultra-broadband source was seeded by long pulse duration (ns) pulsed ASE light and showed very high spectral stability. Measurements of the spectrally resolved pulse-to-pulse stability were conducted using a fast photodiode and monochromator, and found to maintain a two sigma (95%) variance of less than 3% from 1900-2400nm. Within this wavelength range approximately 900mW of output power (>1.5mW/nm) was achieved, only limited by the power handling of the fibre isolator. The intended application of this source was for optical coherence tomography (OCT) measurements of subsurface features within historical works of art, initial demonstrations of long wavelength OCT showed high levels of contrast. When fully implemented this source has the potential to offer spatial resolutions of up to ~4μm within this difficult to reach wavelength range.

Within the final experimental chapter of this thesis, we look at individual mode selection and control within a multimode fibre oscillator. By exploiting an effective index dependence on the resonance wavelength of multimode fibre Bragg gratings we separate,

in wavelength, the different guided modes of the multimode optical fibre. By constructing a laser cavity containing a multimode FBG written into active fibre and a free space wavelength selective element, we successfully demonstrate the selection of the fundamental mode or next higher order mode within a multimode thulium fibre laser. By utilising an electrically controllable AOTF as the wavelength selective element, we can not only select the oscillating mode but also switch between these oscillating modes at very rapid rates. In this work we demonstrate switching between the fundamental mode and donut shaped LP_{11} mode at switching speeds of up to 20kHz and output powers of greater than 5W. By introducing a second passive wavelength selective element into the external cavity, we enhance the spectral selectivity of the wavelength control and demonstrate the selection of closely spaced higher order modes. By driving the AOTF at resonance for the fundamental and LP_{11} modes we were able to excite both modes simultaneously, and by changing the relative RF drive power to the AOTF, we are able to change the relative intensity of these modes. This was demonstrated with the incoherent superposition of the fundamental Gaussian shaped mode and donut shaped LP_{11} mode, allowing the generation of flat-topped beam profiles with flatness becoming an electronically controlled parameter. Finally with an aim to power scale, we demonstrate the successful application of this technique within a cladding pumped architecture and using static volume Bragg grating as free space wavelength selective element. In this configuration we were able to improve the beam quality of a multimode fibre oscillator, moving from an initial M^2 of 3.3 when mode selection was not applied to a near perfect beam quality of M^2=1.05 when fundamental mode was selected.

This technique of mode selection and switching in a multimode fibre laser can have several very interesting applications, by switching laser mode during laser cutting and marking applications, it should be possible to alter the laser processing behaviour and can be likened to a tool head change within a mechanical processing system. The generation of flat-topped laser beams allow more efficient material removal in some ablation applications and the novel feature of adjustable flatness opens up a parameter space that has not been previously explored. An attractive approach for power scaling of this technique was demonstrated with the use of cladding pumped fibre with static VBG. Although, due to high background propagation losses, demonstrated output powers were modest, the high power handling of the VBG makes this a simple approach for static mode selection and should allow significant CW power scaling. In the final section of this

chapter we discuss the core area scaling prospects of this technique. Showing the good potential to further scale core diameter to 70μm without significantly changing the experimental arrangement. With such large core areas it is expected that significant pulse energies should be obtainable through the use of this mode selection technique, and can be achieved with individual fundamental or higher order mode operation.

References

1. R. S. Quimby and M. Saad, "Dy:fluoroindate Fiber Laser at 4.5 μm with Cascade Lasing," in *Advanced Solid-State Lasers Congress* (2013), p. AM2A.7.

2. I. Mingareev, F. Weirauch, A. Olowinsky, L. Shah, P. Kadwani, and M. Richardson, "Welding of polymers using a 2μm thulium fiber laser," Opt. Laser Technol. **44**, 2095–2099 (2012).

3. V. V Alexander, K. Ke, Z. Xu, M. N. Islam, M. J. Freeman, B. Pitt, M. J. Welsh, and J. S. Orringer, "Photothermolysis of sebaceous glands in human skin ex vivo with a 1,708 nm Raman fiber laser and contact cooling.," Lasers Surg. Med. **43**, 470–80 (2011).

Appendix

List of Publications

In progress

1. **J. M. O. Daniel**, M. Tokurakawa, W. A. Clarkson "Wavelength agile thulium fibre laser operating at two-microns" Optics Communications (draft)

2. **J. M. O. Daniel**, N. Simakov, M. Tokurakawa, M. Ibsen, W. A. Clarkson "Ultrashort wavelength operation of a tunable two-microns thulium fibre laser" Photonics Technology Letters (draft)

3. C. S. Chenug, **J. M. O. Daniel,** M Tokurakawa, W. A. Clarkson and H. Liang "Optical coherence tomography in the two-micron wavelength regime for paint and other high opacity material" Optics Letters (draft)

4. **J. M. O. Daniel**, W. A. Clarkson "Bandwidth tunable pulsed ASE source" Optics Express (draft)

5. C. S. Chenug, **J. M. O. Daniel,** M Tokurakawa, W. A. Clarkson and H. Liang "High resolution Fourier domain optical coherence tomography in the 2µm wavelength range using a broadband supercontinuum source " (draft)

6. **J. M. O. Daniel**, N. Simakov, P. C. Shardlow, W. A. Clarkson "Effect of seed linewidth on few-moded fibre amplifiers" Optics Letters (draft)

7. **J. M. O. Daniel**, W. A. Clarkson "Electronic profile control of a multimode fibre laser" Optics Communications (draft)

8. **J. M. O. Daniel**, W.A. Clarkson "Generation of pseudo-radially-polarized beams in a diode-pumped solid-state laser" (draft)

Journal Papers

1. M Tokurakawa, **J. M. O. Daniel**, C. S. Chenug, H. Liang and W. A. Clarkson "Wavelength-swept Tm-doped fiber laser at the wavelength band of two-micron" Optics Express (preprint)

2. D. Lin, **J. M. O. Daniel**, M. Gecevičius; M. Beresna; P. G. Kazansky W. A. Clarkson "Cladding-pumped ytterbium-doped fiber laser with radially-polarized output" Optics Letters (preprint)

3. D. Lin, **J. M. O. Daniel**, W. A. Clarkson "Controlling the handedness of directly excited Laguerre-Gaussian modes in a solid-state laser" Optics Letters 39, 3903–6 (2014).

4. Y. Jung, P. C. Shardlow, M. Belal, Z. Li, A. M. Heidt, **J. M. O. Daniel**, D. Jain, J. K. Sahu, W. A. Clarkson, B. Corbett, J. O. Callaghan, S. U. Alam, D. J. Richardson "First demonstration of a 2µm few-mode TDFA for mode division multiplexing "Optics Express 22, 10544–10549 (2014)

5. **J. M. O. Daniel**, W. A. Clarkson "Rapid, electronically controllable transverse mode selection in a multimode fiber laser" Optics Express, 21 (24), pp.29442-29448. (2013)

6. Z. Li, A. M. Heidt, N. Simakov, Y. Jung, **J. M. O. Daniel**, S.-U. Alam, D. J. Richardson "Diode-pumped wideband thulium-doped fiber amplifiers for optical communications in the 1800-2050 nm window" Optics Express, Vol.21(22) pp.26450-26455 (2013)

7. Z. Li, A. M. Heidt, **J. M. O. Daniel**, Y. Jung, S. U. Alam, and D. J. Richardson "Thulium-doped fiber amplifier for optical communications at 2 µm" Optics Express, Vol. 21, Issue 8, pp. 9289-9297 (2013)

8. **J. M. O. Daniel**, J. S. P. Chan, J. W. Kim, M. Ibsen, J. K. Sahu, W. A. Clarkson "Novel technique for mode selection in a large-mode-area fiber laser" Optics Express Vol.19(13) pp.12434-12439 (2011)

Conference Papers

1. Z. Li, S.U. Alam, **J. M. O. Daniel**, N. Simakov, P. C. Shardlow, J. K. Sahu, A. M. Heidt, Y. Jung, W. A. Clarkson, D. J. Richardson "90 nm Gain Extension Towards 1.7 µm for Diode-Pumped, Silica-Based Thulium-Doped Fiber Amplifiers" 40th European Conference and Exhibition on Optical Communication (ECOC 2014) Tu.3.4.2

2. K. Boyd, N. Simakov, **J. M. O. Daniel**, R. Swain E. Mies A. Hemming W. A. Clarkson J. Haub "Novel Technique for the CO2 Laser Fabrication of Optical Devices with Sub-Micrometer Ablation Depth Precision" 40th European Conference and Exhibition on Optical Communication (ECOC 2014) P.1.4

3. Y. Jung, P. C. Shardlow, M. Belal, Z. Li, A. M. Heidt, **J. M. O. Daniel**, D. Jain, J. K. Sahu, B. Corbett, J. O. Callaghan, S. U. Alam, D. J. Richardson "few-mode TDFA for mode division multiplexing at 2µm" IEEE summer topicals: Space-division Multiplexing technologies for high capacity transmission (SDMT 2014)

4. M Tokurakawa, **J. M. O. Daniel**, S. Chenug, H. Liang and W. A. Clarkson "Ultra-broadband Wavelength Swept Tm-doped Fibre Laser" CLEO/QELS 2014 San Jose 6-11 May 2014 ST1L.2

5. D. Lin, **J. M. O. Daniel**, M. Gecevičius; M. Beresna; P. Kazansky W. A. Clarkson "Direct generation of radially-polarized output from an Yb-doped fiber laser" CLEO/QELS 2014 San Jose 8-13 June 2014 JW2A.22

6. **J. M. O. Daniel**, N. Simakov, M. Tokurakawa, M. Ibsen, W. A. Clarkson "Ultrashort wavelength operation of a tunable two-microns thulium fibre laser" CLEO/QELS 2014 San Jose 8-13 June 2014 SW1N.2

7. **J. M. O. Daniel**, N. Simakov, P. C. Shardlow, W. A. Clarkson "Effect of seed linewidth on few-moded fibre amplifiers" CLEO/QELS 2014 San Jose 8-13 June 2012 STu2N.7

8. H. Liang, C. S. Cheung, M. Tokurakawa, **J. M. O. Daniel**, W. A. Clarkson, M. Spring "Optical Coherence Tomography at 2 micron" LACONA X 2014

9. Y. Jung, Z. Li, N.H.-L. Wong, **J. M. O. Daniel**, J. K. Sahu, S.U. Alam, and D.J. Richardson "Spatial mode switchable, wavelength tunable erbium doped fiber laser incorporating a spatial light modulator" Optical Fiber Communication Conference, paper Tu3D.4. (2014)

10. E. Lim, S. Dasgupta, Q. Kang, **J. M. O. Daniel**, F. Poletti, S. Alam and D. J. Richardson "The Impact of Fiber Core Ellipticity on Few Moded Erbium Doped Fiber Amplifiers" 39th European Conference and Exhibition on Optical Communication (ECOC 2013) P.1.15

11. Z. Li, A. M. Heidt, S.U. Alam, N. Simakov, Y. Jung, **J. M. O. Daniel**, D. J. Richardson "Diode-pumped wideband Thulium-doped fiber amplifiers for optical communications in the 1800-2050 nm window" 39th European Conference and Exhibition on Optical Communication (ECOC 2013) Tu.1.A.2

12. H. Liang, C. S. Cheung, M. Tokurakawa, **J. M. O. Daniel**, W. A. Clarkson, M. Spring, D. Thickett "Next Generation Optical Coherence Tomography for Art" CHARISMA meeting - Torun 2013

13. S. U. Alam, Z. Li, **J. M. O. Daniel**, Y. Jung, A. M. Heidt, D. J. Richardson "Thulium Doped Fiber Amplifiers for 2μm Telecommunications" CLEO-PR & OECC/PS 2013 (Invited)

14. **J. M. O. Daniel**, W.A.Clarkson "Bandwidth-Controllable Tunable Q-Switched Thulium Fibre Laser" European Conference on Lasers and Electro-Optics 2013 CJ-10.2 THU

15. D. Lin, **J. M. O. Daniel**, W. A. Clarkson "Controlling the handenss of directly excited Laguerre Gaussian modes in a solid-state laser" European Conference on Lasers and Electro-Optics 2013 CA-10.2 WED

16. M Tokurakawa, **J. M. O. Daniel**, S. Chenug, H. Liang and W. A. Clarkson "Ultra-broadband Wavelength Swept Tm-doped Fibre Laser" European Conference on Lasers and Electro-Optics 2013 CJ-7.5 WED

17. C. S. Cheung, M. Tokurakawa, **J. M. O. Daniel**, W. A. Clarkson, H. Liang "Long wavelength optical coherence tomography for imaging of painted objects" SPIE Optical Metrology 2013 87900J-87900J-5

18. D. Lin, **J. M. O. Daniel**, W. A. Clarkson "Single-frequency Nd:YAG laser with LG01 donut mode output" Photonics West 2013

19. **J. M. O. Daniel**, W. Andrew Clarkson "Electronically controllable mode selection in a multimode fiber oscillator" Photonics West 2013 - 8601-22

20. Z. Li, A. M. Heidt, **J. M. O. Daniel**, Y. Jung, S. U. Alam, D. J. Richardson "Thulium-doped fiber amplifier for optical communications at 2 microns" OFC '13 Los Angeles 17-21 March 2013 OTh4C.1

21. **J. M. O. Daniel**, W. A. Clarkson "Simple scheme for active mode selection in a multimode fibre oscillator" 5th EPS-QEOD Europhoton Conference Stockholm Sweden 26-31 Aug 2012

22. **J. M. O. Daniel**, M. Tokurakawa, W. A. Clarkson "Power-scalable wavelength-agile fibre laser source at two-microns" 5th EPS-QEOD Europhoton Conference Stockholm Sweden 26-31 Aug 2012 ThB.3

23. **J. M. O. Daniel**, W. A. Clarkson "Generation of pseudo-radially-polarized beams in a diode pumped solid-state laser" CLEO/QELS 2012 San Jose 6-11 May 2012 CM1D.4

24. J. S. P. Chan, **J. M. O. Daniel**, J. W. Kim, M. Ibsen, J. K. Sahu, W. A. Clarkson. "Single Mode operation of a Large Mode Area Thulium fibre laser using a novel wavelength selective mode filter" 5th EPS-QEOD Europhoton Conference Hamburg Germany 29 Aug - 3 Sep 2010 TuD2

25. **J. M. O. Daniel**, J. S. P. Chan, J. W. Kim, M. Ibsen, J. K. Sahu, W. A. Clarkson. "Novel technique for mode selection in a large-mode-area fiber laser" CLEO/QELS 2010 San Jose 16-21 May 2010 CWC5